Fall 2013

Wireless Sensors for Condition Monitoring Applications Operating in Complete Metallic Environment

Lokesh Anilkumar Gupta
Purdue University

Graduate School ETD Form 9
(Revised 12/07)

PURDUE UNIVERSITY
GRADUATE SCHOOL
Thesis/Dissertation Acceptance

This is to certify that the thesis/dissertation prepared

By Lokesh Gupta

Entitled

Wireless Sensors for Condition Monitoring Applications Operating in Complete Metallic Environment

For the degree of Doctor of Philosophy

Is approved by the final examining committee:

DIMITRIOS PEROULIS
Chair

BABAK ZIAIE

FARSHID SADEGHI

JASON V. CLARK

To the best of my knowledge and as understood by the student in the *Research Integrity and Copyright Disclaimer (Graduate School Form 20)*, this thesis/dissertation adheres to the provisions of Purdue University's "Policy on Integrity in Research" and the use of copyrighted material.

Approved by Major Professor(s): DIMITRIOS PEROULIS

Approved by: M. R. Melloch 11-25-2013
Head of the Graduate Program Date

WIRELESS SENSORS FOR CONDITION MONITORING APPLICATIONS OPERATING IN COMPLETE METALLIC ENVIRONMENT

A Dissertation

Submitted to the Faculty

of

Purdue University

by

Lokesh A. Gupta

In Partial Fulfillment of the

Requirements for the Degree

of

Doctor of Philosophy

December 2013

Purdue University

West Lafayette, Indiana

I would like to dedicate this manuscript to my parents Mr. Anilkumar Gupta and Mrs. Maya Gupta.

ACKNOWLEDGMENTS

I would to like to present my sincere gratitude to my graduate advisor Prof. Dimitrios Peroulis for giving me this opportunity to work on this research and guide me throughout the project. I would also like to appreciate Prof. Farshid Sadeghi, Prof. Babak Ziaie and Prof. Jason Clark to serve on my committee and provide helpful suggestions. I would like to thank Mr. Amir Shahidi for providing me with critical inputs in development of various wireless temperature sensor for bearing applications. Additionally, I would like to thank Mr. Nithin Raghunathan for his support in implementing various measurement setups throughout this research study. Furthermore, I would like to thank Mr. Lionel Young and Mr. Berhanu Wondimu at Flowserve Corp., California for their financial as well as intellectual support to this research project. I would also like to express my gratitude to my colleagues from our ARES research group for their helpful insight throughout my research as well as providing a friendly and enjoyable surrounding. Finally, I would like to thank my parents, friends for providing me with continues encouragement and motivation to accomplish my research goals.

TABLE OF CONTENTS

Page

Page

LIST OF TABLES

LIST OF FIGURES

Figure Page

ABBREVIATIONS

AC	Alternating current
AlNiCo	Aluminum Nickel Cobalt
DAQ	Data acquisition card
DC	Direct current
MEMS	Microelectromechanical system
PCB	Printed circuit board
RF	Radio frequency
SmCo	Samarium Cobalt
SQUID	Superconducting quantum interference device

ABSTRACT

Gupta, Lokesh A. Ph.D., Purdue University, December 2013. Wireless sensors for condition monitoring applications operating in complete metallic environment. Major Professor: Dimitrios Peroulis.

Condition monitoring of machines is advantageous in predicting failure and estimating machine component lifetime. Continuous monitoring of parameters such as temperature, vibration, and strain using sensors and consequent data analysis can help in reducing machine downtime by taking corrective actions before failure. Various wireless and wired sensors may be attached to critical components such as bearings, gears, mechanical seals, shafts etc. for measurements. These sensors however are often inadequate solutions as wired sensors are difficult to mount on rotating components, especially in millimeter-size spaces that may exist in some of these components. Wireless sensors provide a viable solution for measurements in rotating components but their range and performance are often limited due to power-supply constraints. The majority of these components are enclosed in metal housings (ex. pumps and motors). In such scenarios, wireless communication is nearly impossible due to severe signal attenuation.

This research provides a unique solution to the above issues by implementing sensors based on temperature-induced magnetic field change of permanent neodymium magnets. Hall Effect sensors are employed to detect these changes. The static magnetic field can pass through non-magnetic, metals such as austinitic steels, copper, aluminum etc. thus allowing temperature sensing through complete metal enclosures. In this thesis, we present wireless sensors for bearing inner race and mechanical seal remote temperature measurement. A permanent neodymium ring-shaped magnet is attached to the inner race of bearing, while temperature is read remotely using a

Hall Effect sensor. The sensor is characterized on a hot plate for calibration equation and noise analysis. These calibration equations are later used for dynamic testing on bearing test rig. For mechanical seals, the sensor is implemented using a 2.2-mm diameter semi-cylindrical magnet with Hall Effect sensor mounted in a hole on steel flange. Temperature sensing is achieved through a metallic flange holding the seal in place. The temperature measurement concept is further extended to measure temperature and vibration simultaneously using permanent magnet and Hall Effect sensor. Furthermore, we also present various magnet lifetime tests and results with a detailed discussion about magnet lifetime. High temperature effects on magnet's magnetic field are also discussed.

1. INTRODUCTION

1.1 Condition monitoring overview

Condition monitoring systems are gaining prominence for failure identification and lifetime prediction of machine components. Continuous monitoring of rotating machinery helps to increase safety, reduce down-time and maintenance costs in high-performance commercial and defense applications [1]. Unlike timed-maintenance that leads to unnecessary repairs and high uncertainty for remaining lifetime, condition-based maintenance enables safe and cost-effective operation. Innovative wired and wireless sensors technologies that can monitor parameters at fault sources can enable predictive maintenance thus reducing plant downtime and resulting in increased efficiency. Some of these sensor technologies are shown in Figure 1.1. The data collected from these sensors can be utilized for designing efficient, long lasting, low maintenance systems and implementing predictive models that are useful in informing users about impending failures under specific operating conditions. Such technologies are particularly important in components such as bearings, mechanical seals, gears etc. These are used in a number of applications including wind generators, automobiles, aircrafts, pumps to name a few.

1.2 Motivation

The two important machine components that are subjected to harsh conditions in industrial systems are bearings and mechanical seals. Failure of these components often cause system and process shutdowns leading to significant financial losses and in some cases human injury and fatalities. Figure 1.2 shows a cross section view of a ball bearing. Various types of failures such as corrosion, indentation, flaking, cracks caused

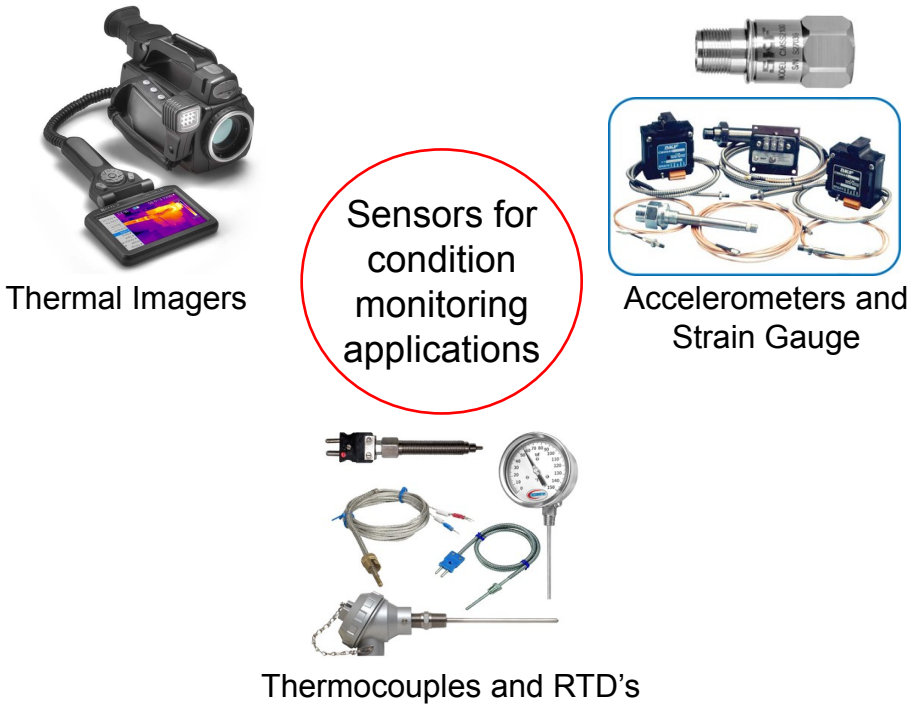

Fig. 1.1. Various sensor for condition monitoring applications.

by loss of lubricant, foreign particles, electrical discharge through lubricant films have been observed in bearings [3]. These failures often cause degradation of the bearing through enhanced friction leading to increased bearing temperature and vibration. Advanced wired and wireless sensors can be utilized to monitor these parameters and collect data. The data are analyzed and corrective action is taken before complete failure either by scheduling maintenance or by replacing the component. Wired sensors such as thermocouples and resistive temperature detectors (RTD's) are often suboptimal solutions due to the additional cost and inconvenience caused by the sensor's wires [4]. Furthermore, wired sensors may be completely impractical in applications with rotating or moving components such as bearing cages and spinning shafts. A variety of successful RF-based research approaches have been presented in monitoring sensitive equipment. Several recent studies have shown the high potential of these technologies for condition-based monitoring for bearings. Nickel et al. and Joshi et al.

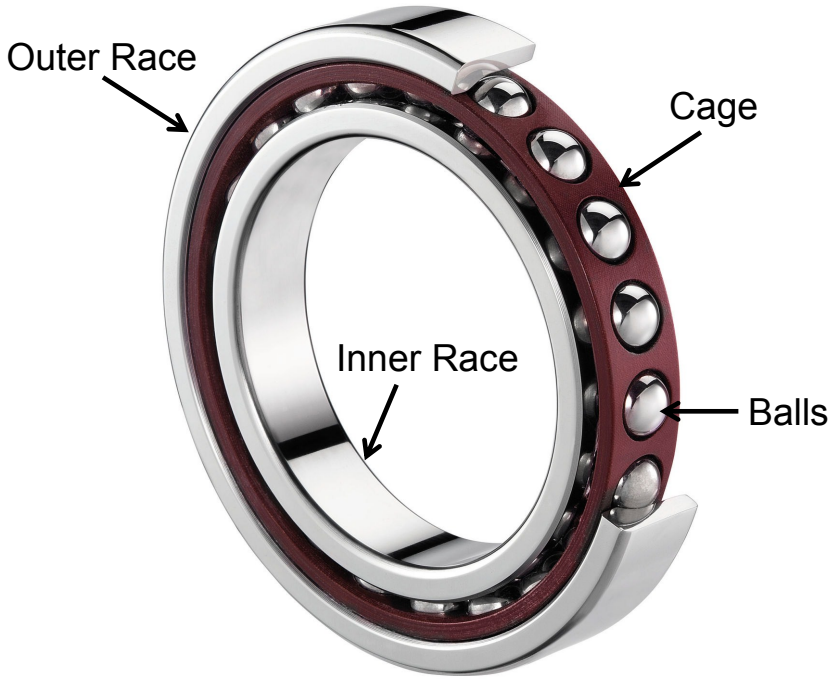

Fig. 1.2. A Ball bearing [2].

have demonstrated a battery and a inductively powered bearing cage telemeter based on temperature sensitive LC oscillator using active components [5], [6]. Components such as transistors and batteries are highly susceptible to degradation from high temperatures in the bearings resulting in inaccurate readings. As a solution, Kovacs et al. experimentally showed an inductively coupled passive bearing cage telemeter [1]. More recently, Scott et al. implemented wireless battery-free MEMS sensors for monitoring bearing temperature up to 300°C [7]. These sensors detect a temperature induced-shift in resonant frequency of an LC tank circuit interrogated using another inductor placed in close proximity. While these sensors successfully measured the true bearing temperature as opposed to the oil or housing temperatures that could be 15-30°C lower [7], the communication range is limited in the presence of metal obstacles since they rely on near-field electromagnetic coupling. Another method of wireless temperature measurement is using optics. Various optical devices such as

thermal guns and optical fibers are used to detect infrared radiation emanating from hot surfaces for remote temperature measurement [8].

Piezoelectric and capacitive type accelerometers are widely used on machines for vibration measurement. By analyzing the spectrum, fault frequencies are identified and appropriate corrective action is taken. These wired accelerometers have limitations similar to wired temperature sensors. Wireless sensors such as proximity and optical probes are also used in industry [9], [10], [11]. Although, these sensors are viable solutions, separate sensors for temperature and vibration measurement often increase installation complexity in machines. To mitigate these issues simultaneous measurement of vibration/strain and temperature using MEMS and optical methods have been successfully demonstrated by [12], [13]. Optical methods are promising for condition monitoring applications, but they are prone to fouling and oil in machines. Furthermore, many optical methods require long optical fibers, which have similar limitations as associated with other wired sensors.

Mechanical seals are critical subsystems of pumps. The purpose of a seal is to prevent or minimize leakage from a pump where the shaft exits the pump housing [14]. A typical mechanical seal consists of several parts, but for this discussion the two primary ones are stationary and rotating faces as shown in Figure1.3. The contacting surfaces are highly polished to a surface roughness of 2-6 μin Ra with flatness of 10-20 μin taper across face. These faces slide relative to each other on a thin fluid film. Any fluid film rupture and increased friction between the rotating and the stationary faces may result in heat generation that leads to deterioration of the contact surfaces, which may eventually lead to seal failure. Typical failure conditions due to high temperatures are listed below [14];

1. The seal tapering in radial direction due to heat generation from friction can lead to the whole system instability, leading to complete failure.

2. Due to high temperature, the seal can become wavy in structure and may lead to increased leakage.

3. For fluids like oil, coke deposits may form that can seriously impair the seal performance.

4. Constant high temperatures may also lead to the formation of crystals if system fluids contain dissolved salts. These crystals can bind to the contacting surfaces and lead to excessive wear in the seals.

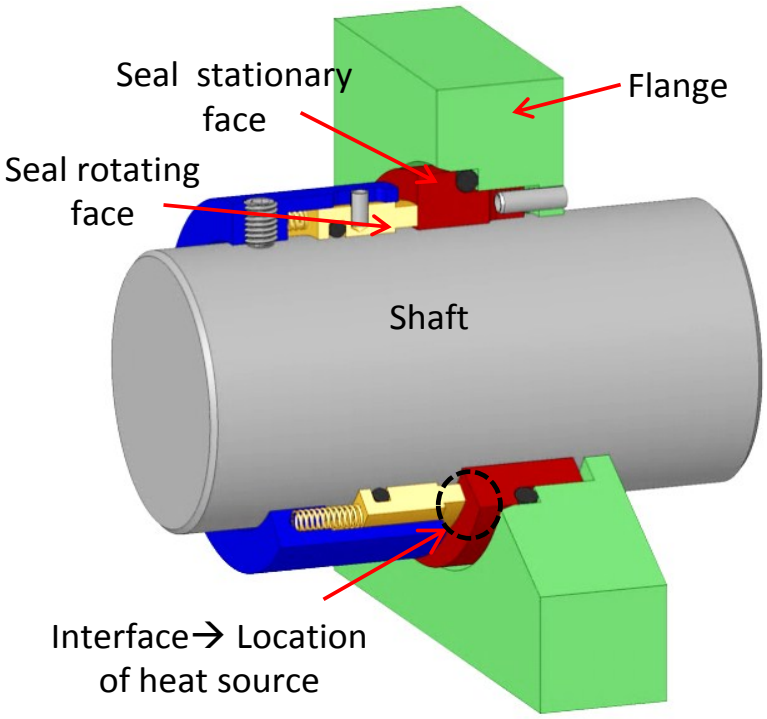

Fig. 1.3. Pump sub-system with mechanical seals, shaft and flange [15].

These conditions make it essential to monitor the temperature of seal interface. The measured data can be analyzed for component lifetime estimation and identifying failures. It can also assist in implementing efficient cooling techniques to maintain temperatures below satisfactory limits. Methods such as acoustic measurements of lubrication film thickness using ultrasonic sensors for seal condition monitoring [16], or wired thermocouple sensors to measure temperatures close to the seal interface have been implemented to give an indication of seal performance. Acoustic methods are sub-optimal due to external noise in industrial environments. Wired sensors

are difficult to implement in confined spaces (few millimeters depending on pump size) that exist in mechanical seal enclosures. In addition, mechanical seal are replaced after their useful life. As a result, in such cases, wired sensors attached to the stationary face of a seal are difficult to replace without disconnecting the signal processing circuitry. Another possible limitation of using thermocouples in monitoring seal temperature is related to user safety and compliance standards. Mechanical seals are widely used in oil and gas industrial pumps for material transport. The government-set, compliance standards have put restrictions on the use of sensors and systems in areas where they may come in contact with explosive hydro-carbons and cause explosion in case of failure events. A thermocouple attached to a seal inner surface is implemented by fusing two different metallic wires. Any failure in temperature signal processing circuitry can result in a voltage appearing across the thermocouple leading to a current flowing through the sensor tip. This can lead to an increase in thermocouple tip temperature that may ignite the hydrocarbons and cause an explosion. Recently, an inductive coupling based temperature sensor for mechanical seal condition monitoring has been proposed by Gupta et al. [17]. This sensor solves the problem of disconnecting wires when seals are replaced but fails to solve the issue posed by compliance. Fluid film-rupture detection using both electrical current and capacitance methods have been implemented for lubricants [18], [19]. These methods are also impractical for mechanical seals as contacts need to be attached to the seal stator and rotor.

1.3 Wireless temperature and vibration sensor based on permanent magnets

In response to the need of wireless sensors that can be read through metal without placing any electrical wires or component near the seal interface and implementable on rotating component such as bearings, this article proposes a unique solution based on permanent magnets. Specifically, a temperature sensor based on neodymium magnets

is experimentally demonstrated. Every permanent magnet has a temperature coefficient i.e. its magnetic field is reduced with increasing temperature. If this change in magnetic field is measured using magnetic field sensors at a constant distance, then temperature can be recorded remotely. A constant magnetic field generated by a permanent magnet is dispersed by materials with high permeability such as iron, nickel, and cobalt. Certain types of alloy steels, however, called austenitic stainless steels have relative permeability close to unity and are widely used in machine parts.Thus, this sensor concept can be used for remote temperature sensing for rotating parts such as bearings and mechanical seal that are enclosed in these non-magnetic metallic housings. A wireless temperature sensor for biological applications based on temperature-induced change in magnetic field in thin film materials has been proposed by H. Osada et al. [20]. This sensor's operating range is limited to a few millimeters and requires an electromagnet as the magnetic field source which makes it unfeasible for bearing applications.

The temperature measurement concept is further extended to simultaneously measure temperature and vibration. When the magnet is attached to a vibrating surface that is at elevated temperature the magnetic field sensor will pick up an AC signal superimposed on DC signal. The DC signal represents the temperature of the surface while AC signal represents vibration amplitude and frequency. By segregating these signals using appropriate hardware / software based filtering temperature and vibration can be measured independently and simultaneously.

This thesis is organized as follows: Chapter 2 discusses about basic sensor concept with a demonstration of sensor operation and temperature detection through metal. In Chapter 3, a wireless sensor for bearing inner race temperature monitoring is presented with dynamic test results on a bearing test rig. Noise analysis and quantifications that pose limits to the sensor's sensitivity are also discussed. In Chapter 4, another application of temperature monitoring of mechanical seal is discussed with experimental results. In this application, the results show dynamic tests on a mechanical seal tester where temperature is sensed remotely through thick metallic

flange. Chapter 5 talks about sensor implementation using cylindrical magnets and discusses about hysteresis observed in the various sensor outputs. Chapter 6 presents simultaneous temperature and vibration measurement techniques using permanent magnets. Chapter 7 addresses the permanent magnet lifetime, optimum dimensions required for the magnet and its reliability for long duration operation. Lastly, in chapter 8 future directions of this research are discussed.

2. SENSOR CONCEPT

In this chapter, the basic concept of sensor implementation is discussed. Section 2.1 describes various types of magnets and Hall Effect sensor [21]. Section 2.3 presents various test setup and results showing applicability of the sensor in an enclosed metallic environment. Lastly, Section 2.4 discusses magnet lifetime and vibration effects.

2.1 Magnet

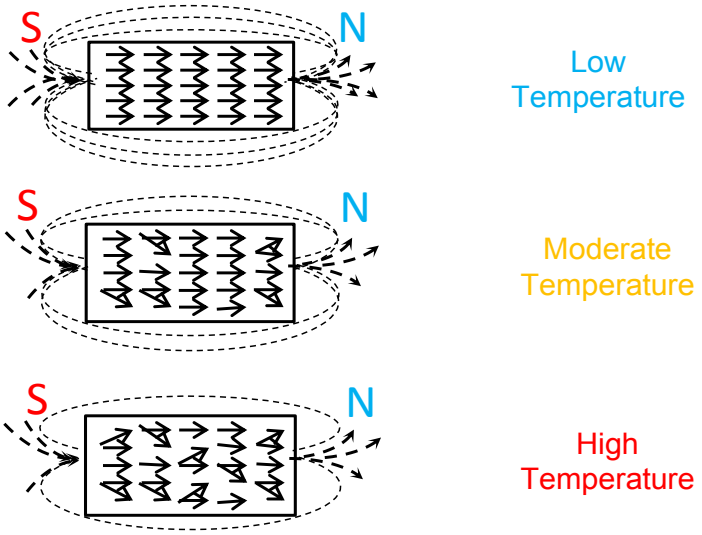

Fig. 2.1. Illustration of temperature-induced change in microscopic domains in magnetic materials ([21]).

The fundamental principle behind temperature-induced change in magnetic field is variation in spatial arrangement of microscopic magnetic domains at high temperatures. In every permanent magnet, each domain is made up of 10^{17} to 10^{21} atoms of ferrous materials. These domains are randomly oriented during magnet fabrica-

tion. When the magnet is subjected to an external magnetizing field, the domains align along the direction of the external magnetic field, thus resulting in a permanent magnet [21], [22]. At elevated temperatures the magnetic domain orientation tends to become random, resulting in loss of magnetic field strength. An inverse effect is observed at lower temperatures with magnetic domains aligning along the direction of the poles. These effects are schematically illustrated in Figure 2.1. As shown, the arrows representing domains are aligned at low temperatures with higher number of field lines traveling from N to S pole. At higher temperatures few domains are randomly oriented, thus reducing the number of field lines traveling from N to S poles. For certain temperature ranges, this change in magnetic domains is reversible. This temperature range depends on the magnet type, its geometry and material composition.

Table 2.1
Common properties of various magnetic materials

Magnet Type	Energy Product (MGOe)	Coercivity (kOe)	Maximum Temp. (°C)	Temp. Coeff. (%/°C)
Nd-Fe-B	42	30	200	-0.11
Sm-Co	30	25	350	-0.04
Al-Ni-Co	10	2	550	-0.02
Ceramic	4	2	300	-0.2

Various magnets such as Al-Ni-Co (Aluminum, Nickel, Cobalt), Ceramic, Nd-Fe-B (Neodymium, Iron, Boron), Sm-Co (Samarium, Cobalt) are commercially available in various size and shapes. These magnets are further classified in multiple grades depending upon their chemical composition and properties such as temperature coefficient, energy content (B-H product), maximum operating temperature etc. Table 2.1 gives a comparison of various magnet properties. Neodymium magnets have the

highest energy product with very high coercivity, i.e. these magnets cannot be easily demagnetized. They also have a high temperature coefficient thats makes them ideal for temperature sensing applications. These magnets have curie temperature of up to 300°C and an operating temperature range up to 200°C depending on the grade of magnet. For the application at hand, N45SH grade neodymium magnet is used with temperature coefficient of 0.11%/°C. The numerical '45' in the magnet grade notation represents the B-H product of a given magnet. For sensing higher temperatures, samarium cobalt rare earth magnets can be used as they have curie temperature of 550°C, operating temperature range of up to 300°C and temperature coefficient of 0.04%/°C [23].

2.2 Magnetic field sensors

Multiple sensor systems have been developed for sensing magnetic fields. Instruments such as magnetometers and SQUID are used for ultra low level magnetic field measurements. Semiconductor based devices such as Hall Effect and giant magnetoresistance based devices are widely used as position sensors in automobiles and industry. Hall Effect sensors are based on the Hall Effect observed in certain type of semiconductor materials when subjected to a constant current and a perpendicular magnetic field. Hall Effect sensor output is highly linear with change in magnetic field and responds differently depending on the polarity of the magnet. They have limited sensitivity compared to other types of magnetic field sensors [24]. Other advantages such as minimum external signal processing circuitry, very small footprint and operation in harsh environment make them ideal for this application compared to some of the high end methods presented in [24]. The Allegro A1395 Hall Effect sensor with sensitivity of 10-mV/G is selected for implementation of this concept. A1395 Hall Effect sensor has a small footprint of 6-mm^2 along with ratio-metric output depending on the magnet pole facing the sensor [25].

2.3 Sensor implementation

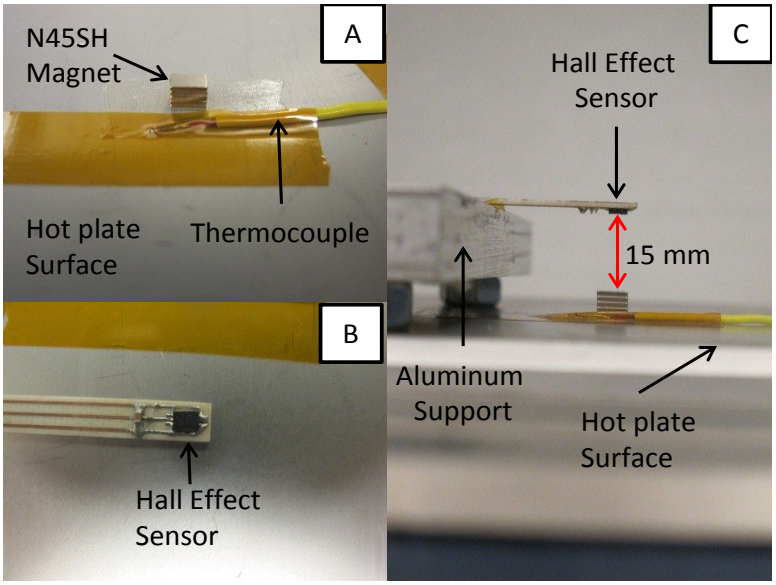

Fig. 2.2. Test setup for wireless temperature sensor measurements in air. The magnets are attached to a non-magnetic hot plate.

Fig. 2.2 shows the sensing element that comprises a stack of five 0.8-mm thick, 5-mm long, 3-mm wide N45SH grade neodymium magnets attached to a hot plate while the magnetic field is sensed by A1395 Hall Effect sensor. These measurements cannot be performed on commonly used, laboratory ceramic hot plates, as these hot plates use inductive coils for heating. These coils generate an alternating magnetic field which may affect the magnetic field sensed by the Hall Effect sensor. To mitigate this issue, sensor testing is performed on a hot-cold plate based on Peltier effect [26]. The magnet stack is attached to the hot plate using a thin double sided tape to record its temperature. A thermocouple is also attached to the hot plate close to the magnet for reference temperature measurement and temperature is cycled from 5°C to 80°C.The Hall Effect sensor is mounted on an aluminum support as shown in Fig. 2.2 at a distance of 15 mm from the magnet top surface. The distance between the magnet and the Hall Effect sensor is a trade-off between the minimum detectable signal (depends on the specific Hall Effect sensor) and the application (how

closely can the sensor be placed to the magnet). For this demonstration we chose a distance that would be relevant for many applications, but no attempt has been made to optimize it. A detailed study that would focus on studying these trade-offs in more detail is beyond the scope of this work. The Hall Effect sensor position is adjusted at 15 mm height to sense maximum magnetic field. This distance can be extended further to few centimeters with small modifications in magnet geometry and test setup. The data are recorded using multi-meter, LabVIEW data logging software and a PC [27]. The Hall Effect sensor output as presented in Fig. 2.3, shows

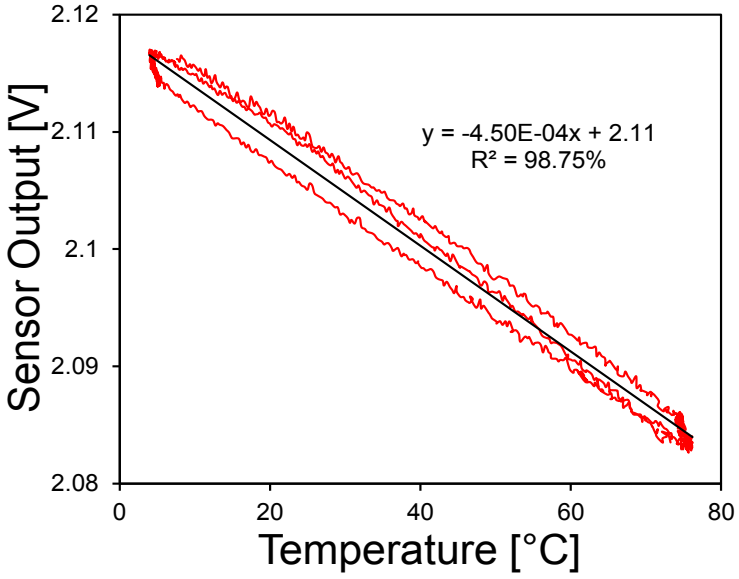

Fig. 2.3. Hall Effect sensor output vs. Temperature. Excellent curve fit value of 98% is observed for temperature variation of 5°C to 80°C.

excellent linear response from 5°C to 78°C range which is significantly lower than the magnet's Curie temperature. The curve fit value is greater than 98%. Although the magnets are rated up to 150°C, the test is limited to about 80°C due to hot plate limitations. This response may become non-linear as temperature approaches magnet's Curie temperature [22]. A minor hysteresis is observed in the sensor output which is similar to typical B-H curve for permanent magnets. The noise in the signal output is due to of inherent noise in the Hall Effect sensor output.

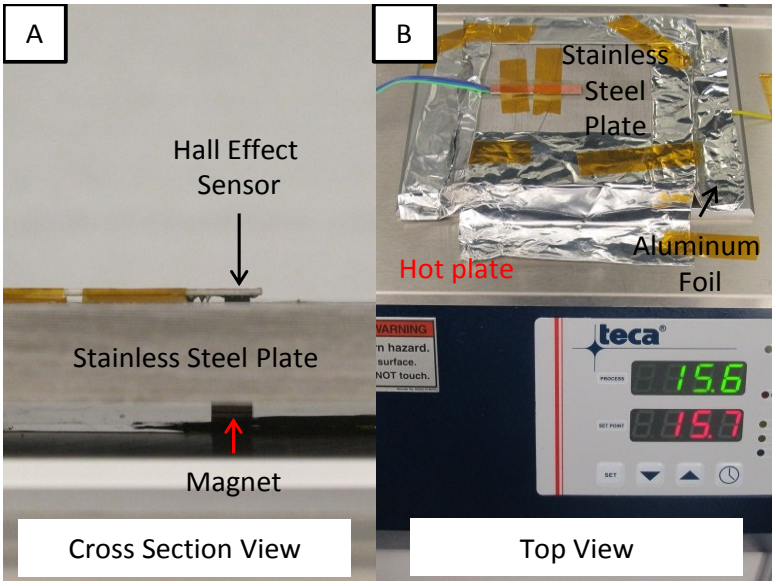

Fig. 2.4. Test setup for wireless temperature sensor measurements through 9.5-mm thick austenitic stainless steel plate placed on non-magnetic hot plate.

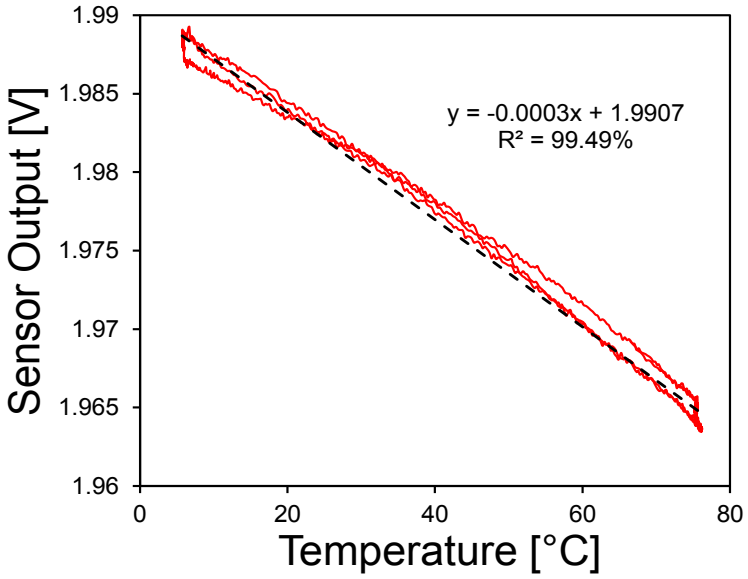

Fig. 2.5. Hall Effect sensor output vs. temperature for operation through stainless steel plate. The sensor response is highly linear with respect to temperature.

Stainless steels are probably the most widely used material for machines. Steels are broadly classified in to two types namely, Martensitic and Austenitic depending on their relative permeability. Martensitic stainless steels have high relative permeability resulting in ferromagnetic behavior similar to iron. Austenitic stainless steels have permeability close to unity [28]. To test the applicability of the sensor in an enclosed stainless steel environment, the setup shown in Fig. 2.4 is implemented. A 9.5-mm thick, 316-grade austenitic stainless steel plate is placed between the Hall Effect sensor and the magnet stack without any contact to the magnets as shown. The Hall Effect sensor is directly attached to steel plate. Furthermore, the open sides are covered using aluminum foil to leave no openings. Fig. 2.5 shows the sensors output with temperature for stainless steel plate between the magnet and the Hall Effect sensor. The sensor output response is linear with temperature which shows effectiveness of the sensor in completely metallic surrounding. The curve fit value is close to 99% indicating excellent sensor response.

2.4 Discussion

An important factor that may affect the sensor's performance is mechanical vibration. The effect of mechanical vibration is dependent on the application, magnitude of vibration, and the arrangement of the Hall Effect sensor and the magnet with respect to application. Passive wireless temperature sensors for bearing cage temperature monitoring have been successfully demonstrated by [1] and [7] in vibrating environment at thousands of rpm (Motor/bearing speed). These sensors are also susceptible to vibrations, but this issue has been mitigated with careful mechanical design that minimizes vibration effects. Similar designs can be readily implemented for the proposed magnetic temperature sensor. Furthermore, simultaneous temperature and vibration measurement using permanent magnet and Hall Effect sensor is discussed in Chapter 6.

2.5 Conclusion

In this chapter, the author has successfully demonstrated, the first wireless temperature sensor operating in an enclosed metallic environment. The sensor detected temperature of a hot-cold plate from 5°C to 80°C at a distance of 19 mm in air. The tests performed in metallic enclosure showed excellent response with temperature demonstrating the effectiveness of this sensor while operating through 9.5-mm thick austenitic stainless steel plate.

3. WIRELESS TEMPERATURE SENSOR FOR CONDITION MONITORING OF BEARINGS

This chapter present the first wireless temperature sensor for bearing condition monitoring operating through metals. The chapter is organized as follows; Section 3.1.1 addresses the basic sensor implementation and characterization of the sensor and the magnet with a stationary bearing at various Hall Effect sensor-magnet distances. Sections 3.1.2 and 3.1.3 address the test setup, results characterizing the effect of various metals and a new concept for detection of localized heating. Lastly, in Section 3.2 dynamic test results from bearing test rig are presented as demonstration of sensor in industrial environment.

3.1 Sensor implementation and characterization: Static

3.1.1 Effect of distance between magnet and Hall Effect sensor

A ring-shaped magnet with 69.5-mm outer diameter, 63.5-mm inner diameter and 6.35-mm thickness is selected for this application. The N45 grade magnet is polarized through its thickness. This polarization and uniform thickness ensures that magnet's south pole always faces the Hall Effect sensor during bearing rotation and the magnet-sensor distance remains constant resulting in an output reading that is proportional to the temperature-induced magnetic field change. The sensor is mounted on a commercially-available SKF 6012-2RSJEM bearing [29]. The inner race dimension of the bearing precisely matches the magnet dimensions. The bearing is made up of ferrous material allowing the magnet to be directly attached to the bearing without any adhesive. Figure 3.1a-b shows the ring-shaped magnet, bearing, and the test setup. The bearing is horizontally attached to a hot-cold plate using thin double-

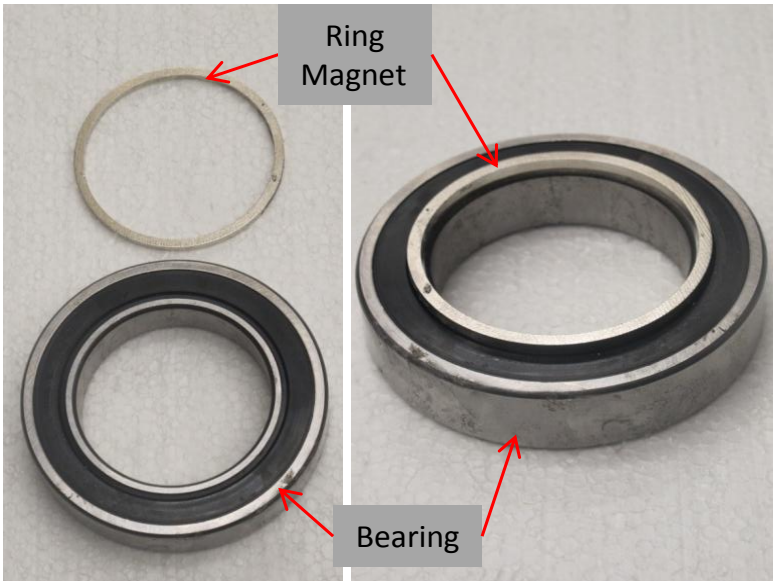

(a)

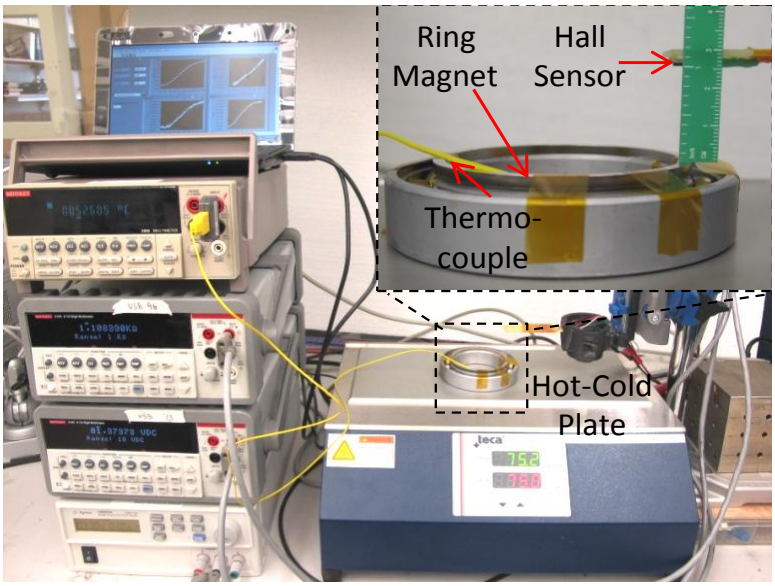

(b)

Fig. 3.1. (a) Ring magnet and SKF 6012-2RSJEM bearing. (b) Test setup for characterizing the effect of distance between the magnet and Hall Effect sensor. The Hall Effect sensor is mounted on a Z-axis apparatus to modify the distance between the magnet and Hall Effect sensor.

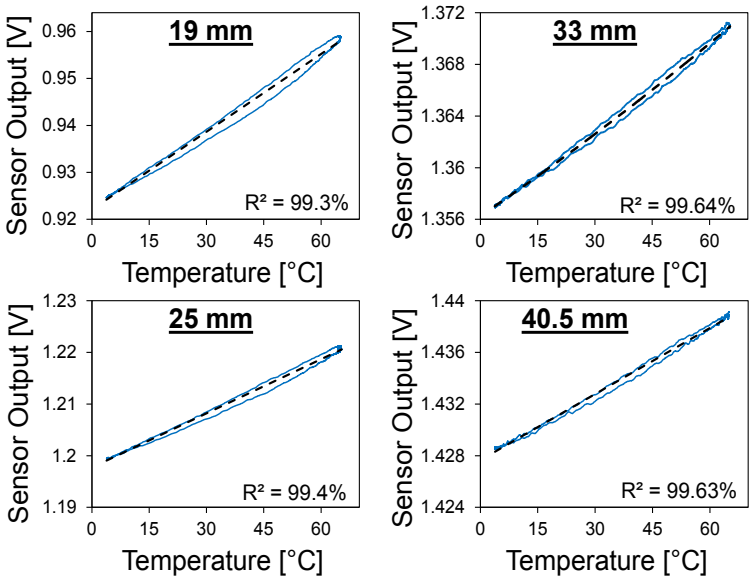

(a)

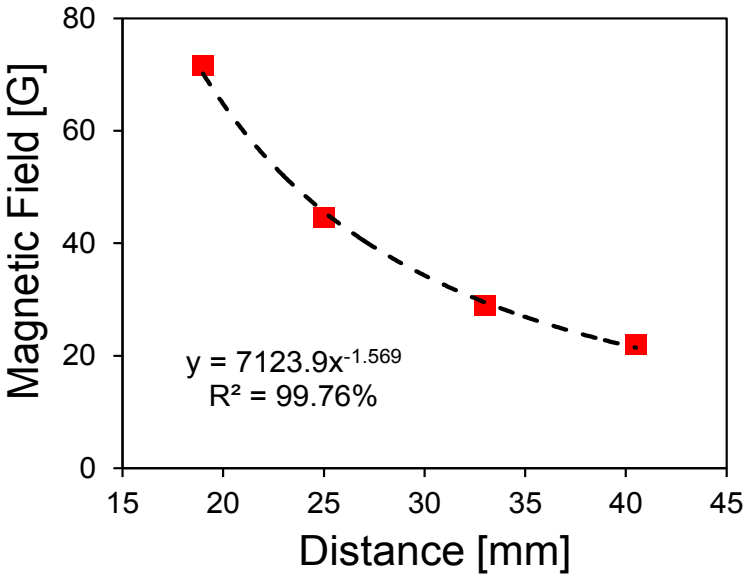

(b)

Fig. 3.2. (a) Measured sensor output vs. temperature at various distances (unprocessed data). Each data set demonstrates a curve fit value close to 99%. (b) Measured magnetic field vs. distance at 20°C. The distance and the magnetic field are related by power equation.

sided adhesive tape. A thermocouple is attached close to the magnet for reference

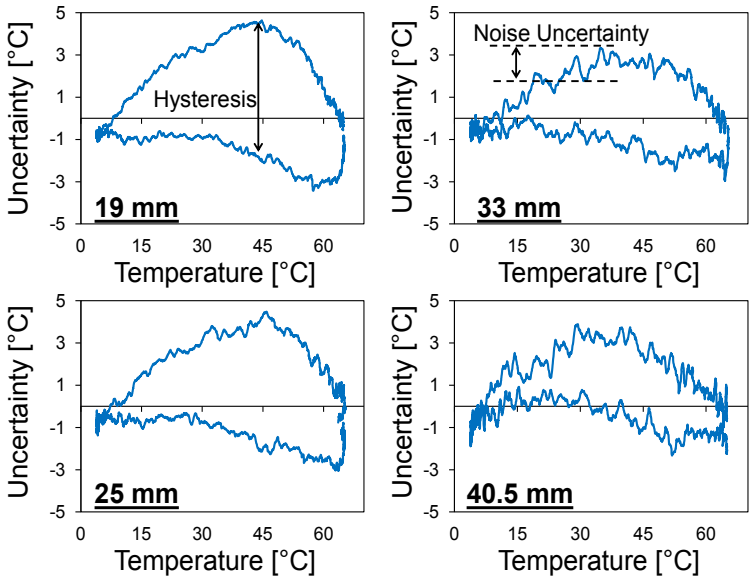

Fig. 3.3. Uncertainty vs. actual temperature. The uncertainty values are higher for smaller distances which is attributed to hysteresis in the sensor output. As the distance increases the hysteresis reduces with increase in noise in the sensor output.

temperature measurement. This test cannot be performed using conventional ceramic laboratory hot plates, as these hot plates use heating coils which are magnetic. Figure 3.1b shows a TECA, peltier effect based hot-cold plate [26]. For this application Allegro A1395 Hall effect sensor is used to measure change in magnetic field. This sensor is described in detail in Chapter 2. The Hall Effect sensor is soldered on a printed circuit board and mounted on a variable Z-axis setup above the hot-cold plate as shown. Further, the bearing is subjected to temperature cycling from 0°C to 80°C (hot plate surface temperature). The data from the thermocouple and the Hall Effect sensor are logged using a LabVIEW program and a PC [27]. This test is performed to characterize the effect of distance variation between the magnet and the Hall Effect sensor on temperature measurement.

Figure 3.2a shows the sensor output versus temperature for various distances with linear curve fit values. The sensor output follows a nearly linear trend with temperature from 4°C to 65°C (R^2 values are close to 99%). Although the ring

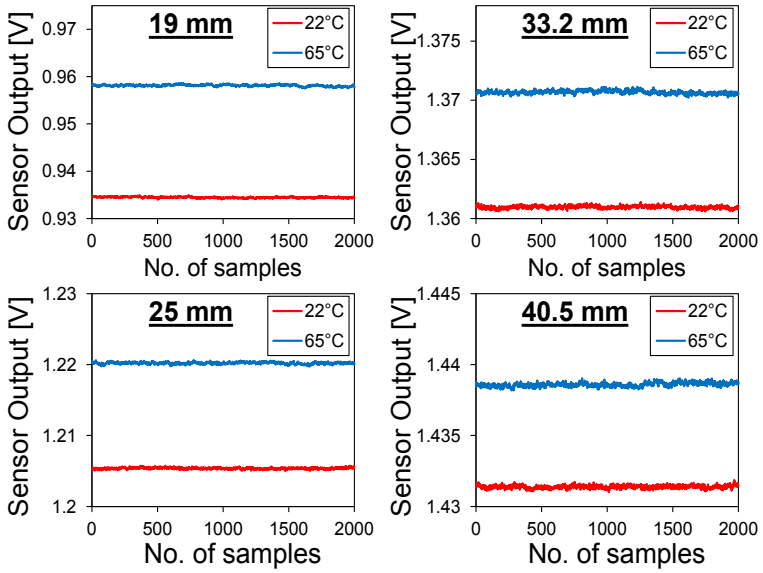

(a)

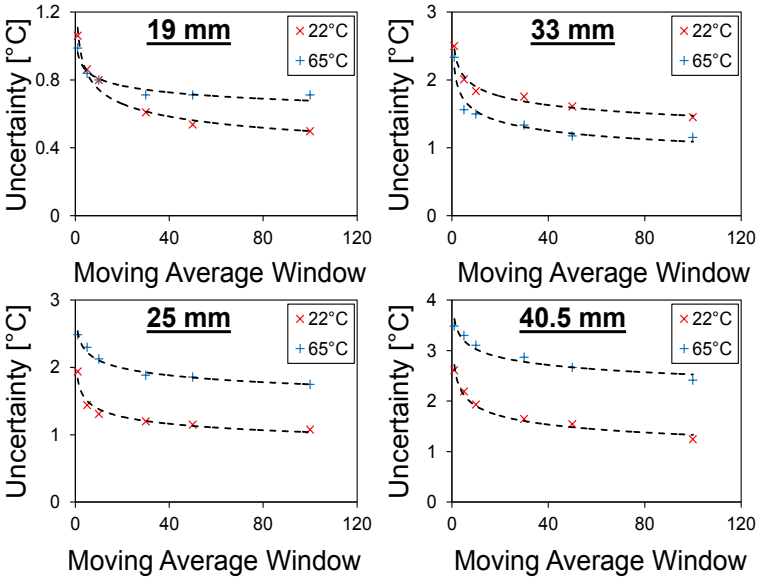

(b)

Fig. 3.4. (a) Measured sensor output vs. number of samples for various distances at constant temperature. (b) Uncertainty vs. moving average window. These results illustrate the number of samples required for averaging to reduce the noise uncertainty in the measurement.

magnet is rated up to 80°C, the measurement range is limited by the temperature range of the hot-cold plate and not by magnet specifications. Hysteresis is observed in the sensor outputs for all distances. This hysteric response is possibly due to difference between response time of the magnet sensor and thermocouple.

Figure 3.2b shows the measured magnetic field versus distance plotted at various temperatures. The magnetic field intensity at a distance from the magnet is a function magnet's geometry, surrounding material's permeability, and the point at which magnetic field is measured with respect to the magnet. In this case, the field is measured above a line passing through the circumference of the ring magnet. The measured field is proportional to $1/d^{1.569}$ as shown.

Figure 3.3 shows the hysteresis and noise-induced uncertainty in the measured temperature calculated using the linear curve fit equations. The uncertainty in the measured signal has two components, namely hysteresis and Hall Effect sensor noise as shown. The maximum hysteresis-induced discrepancy is 5.5°C for 19 mm distance, decreases to 3°C at 40.5 mm. These maximum values are observed around 45°C. Although, increasing the Hall Effect sensor-magnet distance results in reduced hysteresis, the inherent noise in the Hall Effect sensor output limits the maximum distance that can be achieved with sufficient signal integrity. The maximum distance experimentally tested is 40.5 mm. This is the highest reported sensor-reader distance for bearing applications for battery-free system [1], [5], [6]. It is worth mentioning that the combination of the ring magnet and the ferrous bearing forms a large magnet which increases the volume occupied by the magnetic field lines. This effect enhances the interaction of the field lines with the Hall Effect sensor allowing for interrogation of the magnetic field at larger distances in the order of few centimeters.

Figure 3.4a shows sensor output versus number of samples when temperature is held constant at 22°C and 65°C. These tests and data analysis quantify the Hall Effect sensor noise-induced uncertainty with respect to temperature. Figure 3.4b shows the uncertainty in the measured temperature versus moving average window size. The noise-induced uncertainty in the temperature is minimum for 19 mm in the range of

0.5°C to 1°C depending on the number of samples averaged. The uncertainty increases to 2.6°C to 3.4°C at 40.5 mm. The increase in the distance between magnet and the Hall Effect sensor reduces the temperature-induced change in magnetic field sensed by the Hall Effect sensor, resulting in increased noise-induced uncertainty. Table 3.1 summarizes the effects of hysteresis and noise in the temperature measurement. The noise uncertainty reduces with increase in the averaging sample size as shown in Figure 3.4b, but averaging large number of samples may affect the sensor response time. Nevertheless, the noise-induced uncertainty in the sensor output is almost constant beyond 30 sample average which is optimum for achieving noise-induced uncertainty of less than 0.5°C to 2.8°C depending on the Hall Effect sensor-magnet distance.

Table 3.1
Uncertainty analysis summary

Distance [mm]	Total change in voltage from 4°C to 65°C [mV]	Noise amplitude [mV]	Hysteresis at 45°C [°C]	Noise uncertainty[%]
19	32	0.941	5.5	2.9
25	20	0.923	5	4.6
33	13	0.915	4	7
40.5	10	0.870	3	8.7

3.1.2 Effect of metal plates between magnet and Hall Effect sensor

The majority of rotating machines are constructed using stainless steel. These stainless steels are broadly classified as martensite and austenitic, based on their relative permeability [28]. Martensite steels have high relative permeability making them ferromagnetic in nature. Austenitic stainless steels have relative permeability

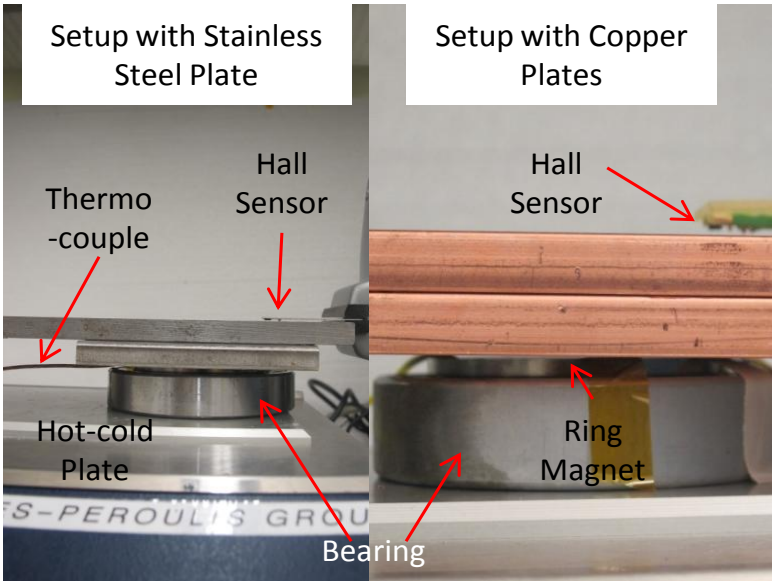

Fig. 3.5. Test setup shows two 9.5-mm thick metal plates placed between the bearing/magnet and the Hall Effect sensor.

close to unity resulting in non-magnetic steel. Figure 3.5 shows a test setup to study the temperature sensor operation through non-magnetic steel plates and commonly used non-ferrous metals. The test setup is similar to the setup shown in Figure 3.1. The distance between the magnet and the Hall Effect sensor is fixed at 26 mm. Two 9.5-mm thick aluminum, copper and 304-grade austenitic stainless steel metal plates are placed between the Hall Effect sensor and the magnet on the bearing.

Figure 3.6 shows the measurement results for three types of metal plates. The sensor response is linear with respect to temperature for all three metals. All plots demonstrate an excellent curve fit value of more that 96% from 7°C to 54°C. The plots show hysteretic response similar to plots shown in Figure 3.2a. The maximum field lines are able to penetrate the metal plates and reach the Hall Effect sensor without significant distortion or attenuation. In the case of stainless steel, the measured Hall Effect sensor output is slightly greater than copper and aluminum. This is possibly due to presence of active, scattered ferrous domains in the steel plate and slightly higher than unity permeability that results in small absorbtion and distortion of the

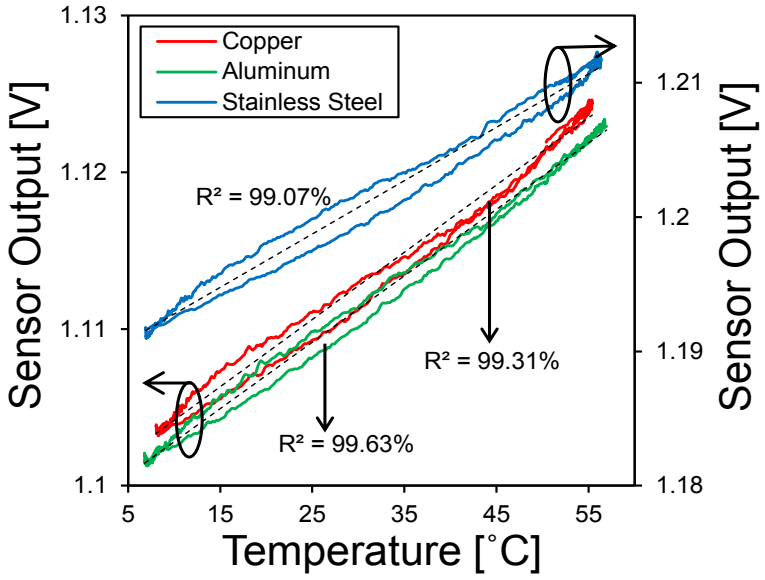

Fig. 3.6. Measured Hall Effect sensor output vs. temperature in the presence of different types of metal plates. The sensor output is higher with the stainless steel plate possibly due to presence of random ferrous domains in the steel.

magnetic field lines. These results indicate significant advantage of the presented sensor over traditional wireless and optical temperature sensors that are unable to function when obstructed by thick metals.

3.1.3 Localized heating detection

Multiple bearing failure modes are presented in [3]. Load variation and shaft misalignment on the bearing inner race leads to localized heating and in-turn localized degradation of the bearings. This localized failure is generally detected using visual inspection, as localized heating leads to spot burning and blackening of the bearing. The bearings which are visually inaccessible, multiple thermocouple sensors can be attached to the periphery for localized failure detection. Accuracy of this method is limited by the number of sensors that can be mounted on outer periphery of the bearing. Sensor presented in [5] , [7] are used for bearing cage temperature monitoring.

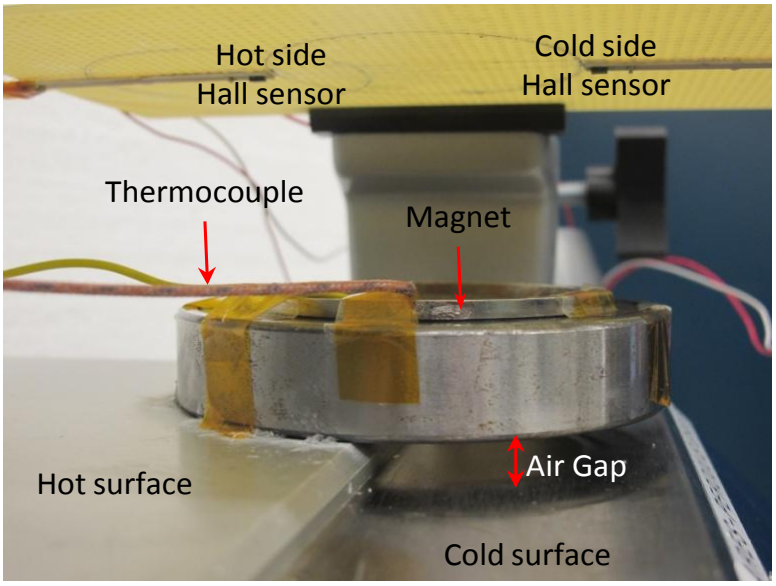

Fig. 3.7. Test setup with bearing partially placed on the hot-cold plate. Two thermocouple are attached to heated and unheated sides of the bearing for reference measurement.

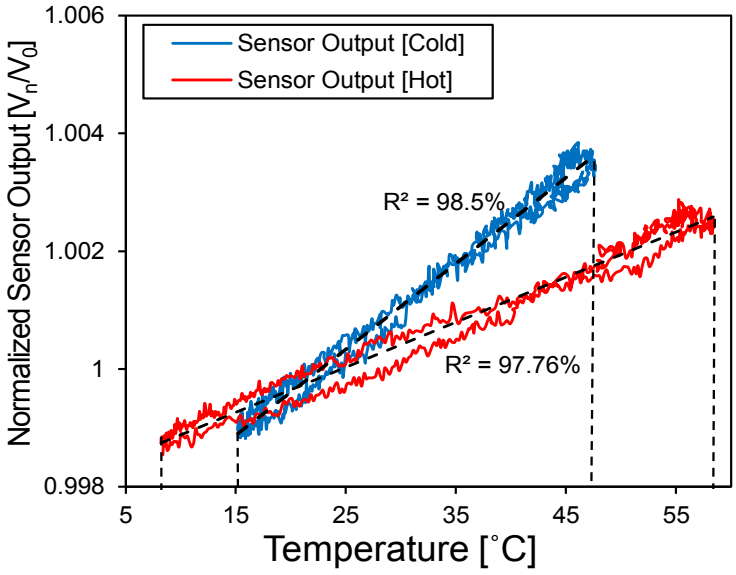

Fig. 3.8. Hall Effect sensor output vs. temperature for hot and cold side sensors. The noise on the measurement curve is due to inherent ultra low frequency 1/f %noise of the Hall Effect Sensor.

These capacitive sensors are attached to the bearing cage as the cage rotates at much lower rpm than the shaft. A temperature-induced capacitance change results in shift in resonant frequency of the inductive coil that is detected remotely. For localized heat detection, multiple capacitive elements are needed with different resonant frequencies. This results in a non-uniform structure throughout the circumference of the bearing in the complete sensor system. Although, this arrangement can be implemented for bearing cage temperature measurement, such multiple sensors are not suitable for inner race due to bearing balancing at high speeds. The magnetic sensor proposed in this article, provides a unique solution to this issue. The uniform shape of the magnet throughout its circumference ensures that bearing is balanced while operating at high speeds. Localized heat spots will result in different thermal regions on the surface of the magnet resulting in temperature-induced magnetic field variations along the circumference of the ring magnet. Figure 3.7 shows a test setup implemented to study the ability of the sensor system to detect localized hot spots. The bearing is placed horizontally on the hot plate such that only half of the bearing is in contact with the hot surface. Two Hall Effect sensors are used to emulate a rotating bearing with a single sensor detecting change in the magnetic field due to temperature at a fixed distance. The first sensor is facing the heated side and second sensor is facing the relatively unheated side of the bearing. Thermocouple sensors are placed on each side of the bearing for reference temperature measurement. The distance between the bearing and the magnet is set at 40.5 mm.

Figure 3.8 shows the measurement results for localized heating test setup. Both the sensor outputs follow a linear trend with temperature. These trends are similar to plots shown in Figure 3.2a. Ideally, the slope of both the curves should be same, but due to piece-to-piece variation in sensitivity of the Hall Effect sensors the slope of the curves is different. Of interest, is the region covered by the individual trends. The unheated side trend line only varies from 15°C to 45°C while the heated side trend line varies from 7°C to 56°C indicating temperature gradient-induced variation in magnetic field around the circumference of the magnet. These results are encouraging

as this sensor configuration is capable of distinguishing between cold and relatively hot side of the bearing using same monolithic ring magnet. Further research is needed for such system implementation as the individual points on the bearing periphery need to be known to detect of exact location of shaft imbalance. In case of practical implementation, the two Hall Effect sensors can be replaced by a single Hall Effect sensor placed at a fixed distance with bearing rotation synchronized with the sensor output.

3.2 Sensor implementation and characterization: Dynamic

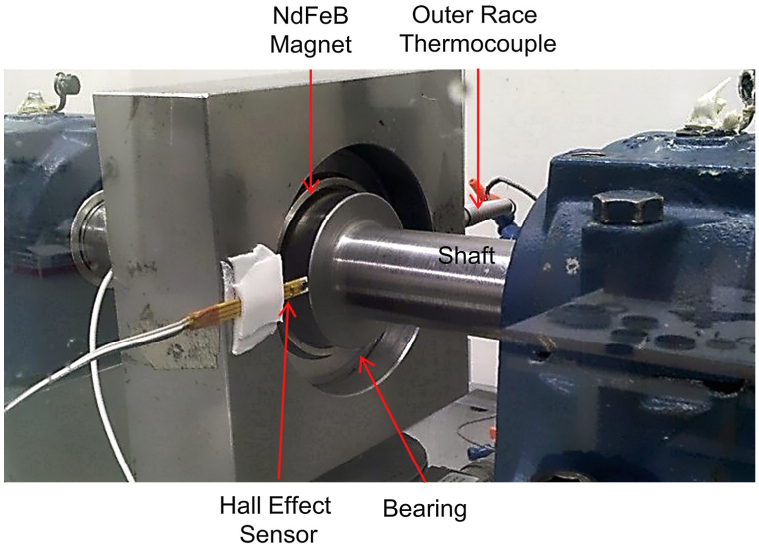

Fig. 3.9. Bearing test rig with magnet and Hall Effect sensor mounted on the bearing.

Figure 3.9 shows the presented magnet and Hall Effect sensor mounted on a bearing test rig. A thermocouple is also mounted in close proximity of the bearing outer race to measure its temperature. A high temperature N42SH grade ring magnet with identical dimensions is used for dynamic testing. N42SH grade magnets are rated up to 150°C with energy product same as the N42 grade. The distance between the magnet and Hall Effect sensor is approximately 14 mm, while the distance between the

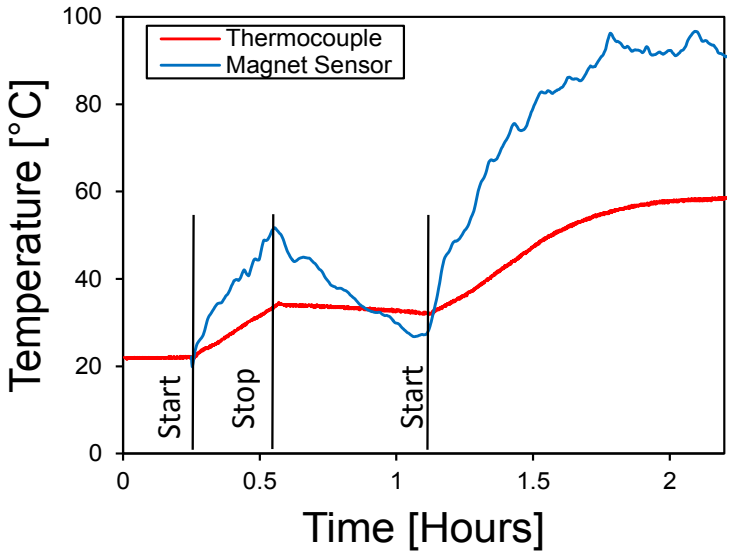

Fig. 3.10. Measured magnet sensor output and outer race thermocouple vs. time. The sensor response is sufficiently fast to detect transient condition such as starting and stopping of the rig.

martensite steel shaft and Hall Effect sensor is 3 mm. The rotating shaft is ferromagnetic which in-turn distorts the magnetic field lines reaching the Hall Effect sensor. It is experimentally found that this effect results in measured magnetic field values close to the values measured for distance of 25 mm without the shaft. A constant temperature offset is added to the calibration equation for 25 mm distance, to account for this field distortion. The offset value is equal to the difference between the temperature measured by the outer race thermocouple and magnet sensor at the start of the test (room temperature). This test is performed at 1,500 rpm and 100-150 lb load for 2.2 hours. Figure 3.10 shows the time based response of the outer race thermocouple and the magnetic sensor on the bearing for 2.2 hours of operation. The response clearly shows that outer race temperature is not a true indicator of bearing temperature. The magnet sensor response is much faster as compared to the thermocouple even for transient conditions such as starting and stopping of the test rig. These results are in accordance with result presented in [7] where bearing cage temperature is much higher than the temperature indicated by outer race thermocouple.

3.3 Conclusion

In this chapter, the author has presented an innovative concept of using a permanent magnet to implement a wireless temperature sensor for bearing condition monitoring in a completely metallic environment. The presented sensor, is capable of measuring temperature remotely from a distance of 40.5 mm which is the highest reported for a wireless battery free bearing condition monitoring system. The sensor is able to detect temperature-induced change in the magnetic field through a 19-mm thick stainless steel plate using a Hall Effect sensor. Furthermore, the dynamic tests on the test rig show the effectiveness of the sensor in detecting the temperature of the inner race without any active components mounted on the bearing while simultaneously proving the ineffectiveness of outer race thermocouple as true indicator of bearing temperature.

4. WIRELESS TEMPERATURE SENSOR FOR CONDITION MONITORING OF MECHANICAL SEALS

In this chapter, the first wireless temperature sensor operating through metal enclosure for mechanical seal application is presented [30]. The chapter is organized as follows: Section 4.2 discusses the sensor and magnet implementation in the mechanical seal-type interface, Sections 4.3 discusses the test setup and measurement results followed by conclusion in the last section.

4.1 Sensor components

The magnet grade selection for temperature sensing applications is a tradeoff between maximum temperature range and maximum possible strength. High strength magnets such as N52 are only specified up to 80°C. While magnet grades such as L30EHT have 43% less strength but can be used up to 250°C [31]. The high strength grade magnets enable larger distances between magnet and Hall Effect sensor but provide a limited operating temperature range. As a tradeoff we selected, a L38EHT grade neodymium magnet for this application. These magnets are rated up to 200°C with coercivity of 2388 KOe and magnet energy product of 38 MGOe. The Micronas HAL825 Hall Effect sensor is selected for temperature-induced magnetic field variation detection for this research. This sensor has a programmable sensitivity of 70 mV/G and 5 V supply [32]. The small size, minimum external signal processing circuitry and operating temperature range of 150°C makes this sensor ideal for mechanical seal temperature sensing applications.

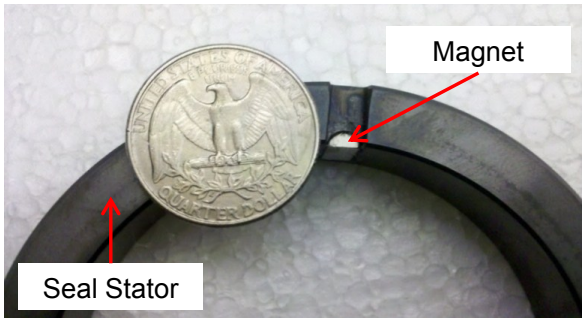

(a)

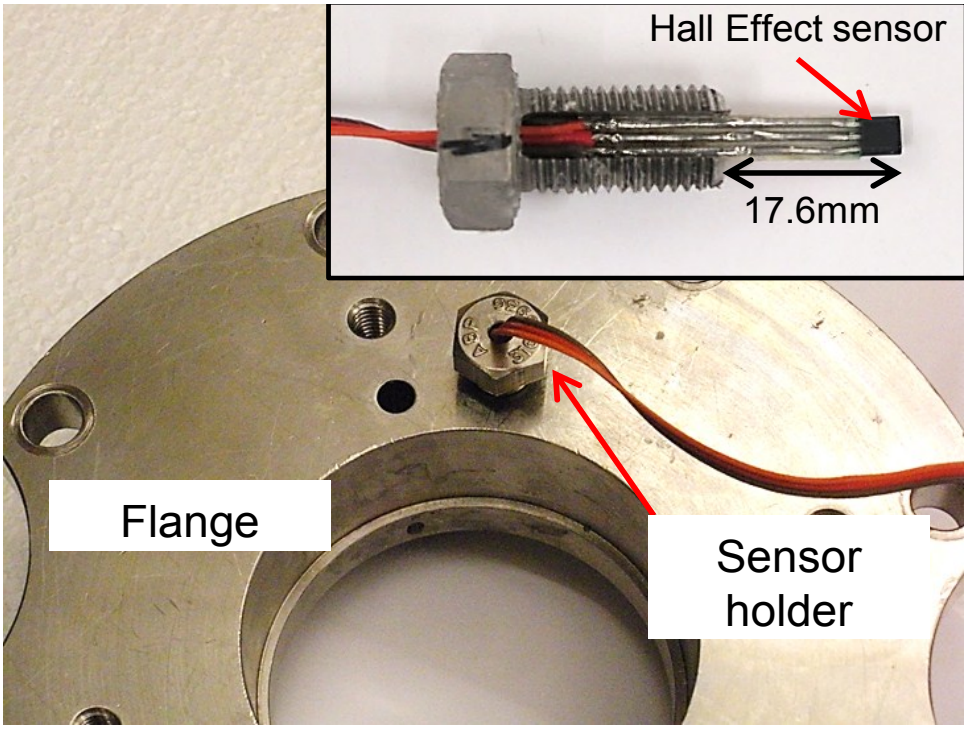

(b)

Fig. 4.1. (a) Seal stator with semi-cylindrical magnet. (b)Sensor holder mounted in the seal flange. Inset shows the Hall Effect sensor mounted in the holder.

4.2 Sensor implementation

A semi-cylindrical slot with 2.4-mm radius and 9.5-mm length is drilled in the silicon carbide seal stator as shown in Figure4.1(a). The L38EHT custom made semi-cylindrical magnet of 2.2-mm diameter and 9.5-mm length is attached to this

slot using temperature conductive adhesive. Magnet dimensions and geometry are selected based on available space in the seal and flange assembly while simultaneously keeping the magnet dimensions large enough with reasonable permeance coefficient. The completed assembly is shown in Figure 4.1(a). The magnet was annealed at 110°C for 1 hour to minimize potential effect of any unstable magnetic domains before assembly [33].

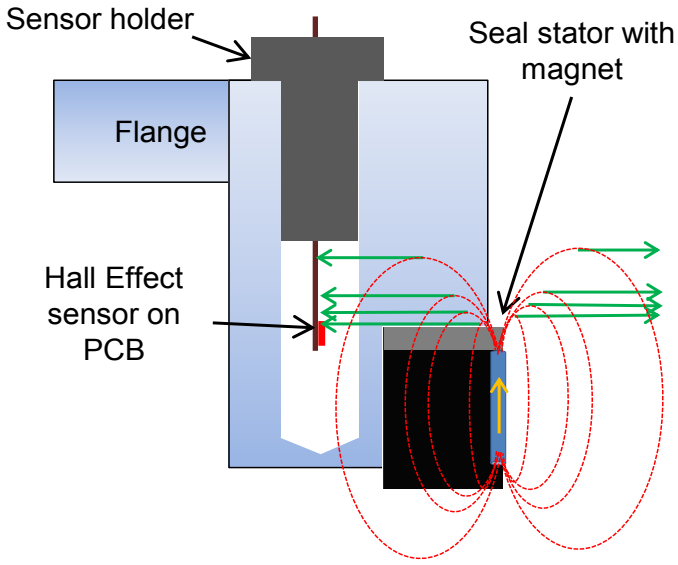

Fig. 4.2. Illustration of field lines sensed by Hall Effect sensor.

The Hall Effect sensor is mounted on a small 4.7-mm wide 0.8-mm thick printed circuit board. Three leads are attached to the PCB (Figure 4.1(b)) for power supply, ground and output. The sensor PCB is mounted on a threaded holder as shown in Figure 4.1(b). This holder is made by cutting a 5-mm wide slot in a 7/16-14, 25.4-mm long, 316-grade non-magnetic stainless steel screw. The sensor PCB is attached in the slot using an adhesive. This assembly is coated with an insulating transparent conformal coating for operation in the harsh environment. A 9.5-mm diameter hole is drilled in the flange as shown in Figure 4.1(b) to screw in the Hall Effect sensor and the sensor holder, thus fixing the position of the sensor with respect to the magnet. The orientation of the field lines is shown in Figure 4.2. The Hall Effect sensor is

subjected to lateral field lines close to the magnet south pole. This arrangement ensures that the magnet has its longest dimension along its length with minimum interference to the rotating shaft.

4.3 Test setup and results

4.3.1 Stationary test on a hot plate

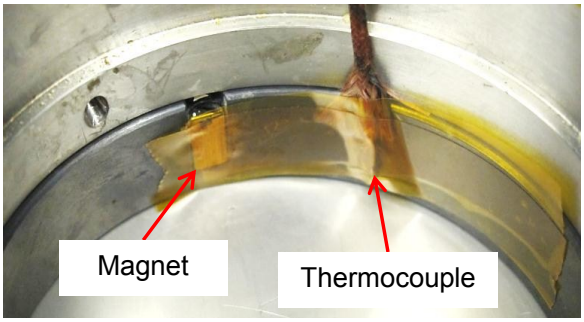

(a)

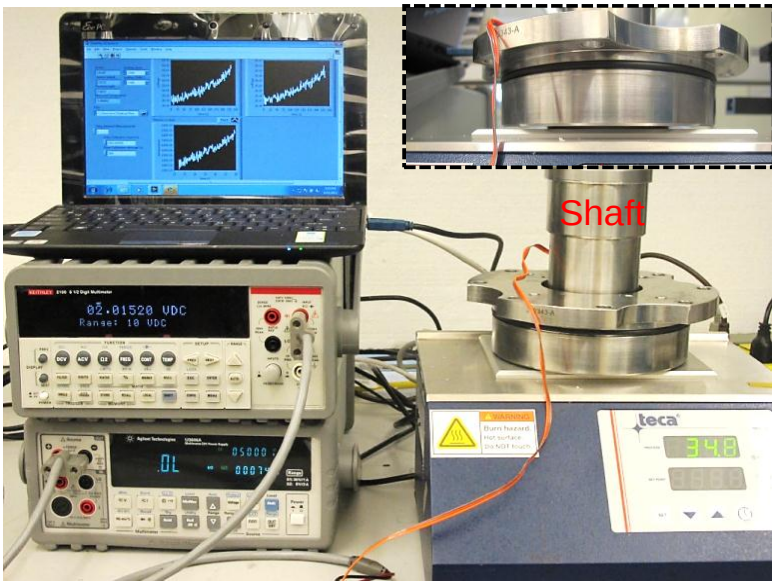

(b)

Fig. 4.3. (a) Seal with magnet placed on peltier hot plate.(b) Complete test setup. Inset shows seal with flange kept inverted to simulate the seal stator getting heated directly from the hot plate.

Tests were performed on a Teca hot/cold plate [26]. These tests cannot be performed on commonly used ceramic hot plates as they generate their own magnetic field. A thermocouple is attached to the seal stator as shown in Figure 4.3(a) for reference temperature measurement. The sensor holder position is fixed using hot glue to avoid accidental rotation of the screw. The seal with the flange, shaft and sleeve are kept inverted on the hot plate as shown in Figure 4.3(b) to simulate the seal stator in contact with the rotor in pump housing subjected to friction and heat. The hot plate is cycled from 0°C to 90°C with rise time, fall time and constant temperature time of 40 minutes each. The data are recorded using a multi-meter, PC and Labview system [34].

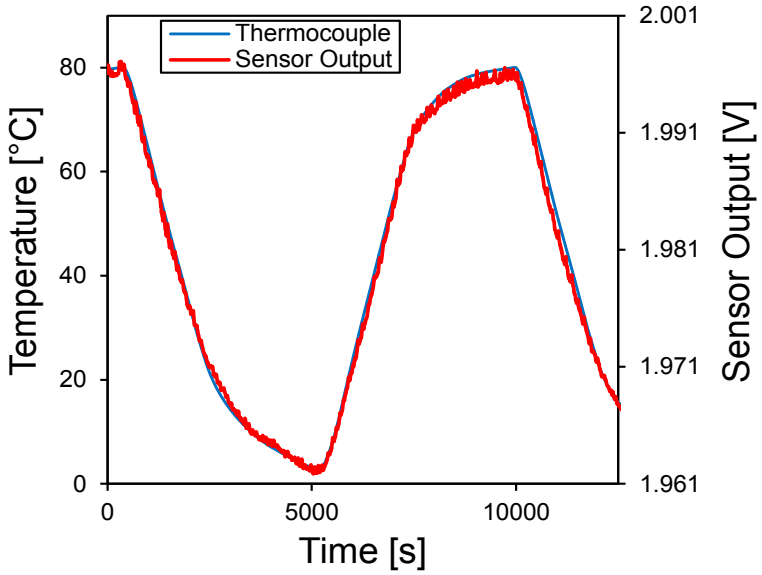

Fig. 4.4. Measured Hall Effect sensor output and seal temperature vs. time (static operation).

Figure 4.4 shows measured temperature cycling results from 8°C to 79°C. The Hall Effect sensor output closely follows the temperature curve. Figure 4.5 shows Hall Effect sensor output vs. seal temperature. The results show excellent congruity with the linear equation with curve fit value of 98%. A minor hysteresis is observed which is possibly due to the difference between the response times in magnet sensor's

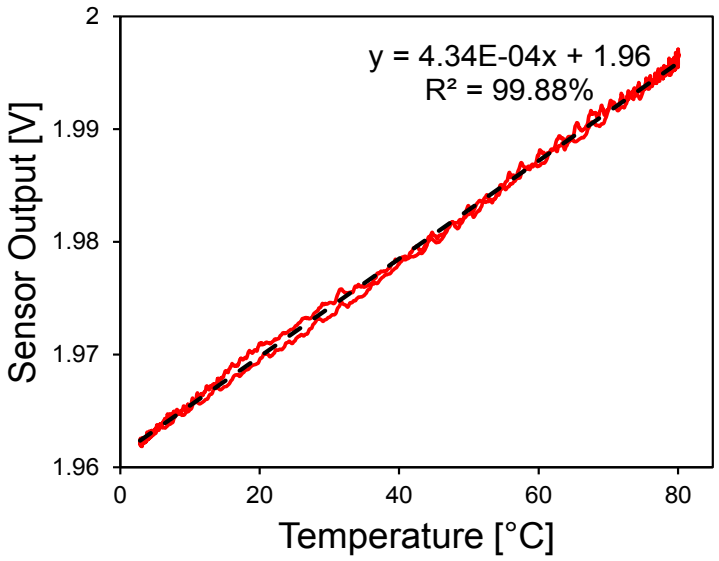

Fig. 4.5. Measured Hall Effect sensor output vs. seal temperature (static operation). The results indicate high degree of congruity with respect to linear curve fit.

output and thermocouple. The upper temperature limit for the sensor is limited by the hot plate and the test setup and not by the magnet temperature specifications.

4.3.2 Dynamic test in a mechanical seal test rig

The stationary face and flange assembly was installed on a seal test rig. The distance and position of the magnet and Hall Effect sensor is identical to the system configuration implemented for stationary testing. A thermocouple is attached to the seal stator to measure the seal reference temperature and compare the results obtained by the magnet sensor. The thermocouple data are acquired using NI-9310 thermocouple DAQ card [34]. On-site calibration was performed by rotating the sensor holder orientation and matching the Hall Effect sensor output to the voltage value at 22°C (room temperature) measured during stationary tests. The magnet sensor data is acquired using a NI-6343 USB DAQ [34] and applying the calibration equation shown in Figure 4.5. An offset of -6°C is added to the calibration equation to com-

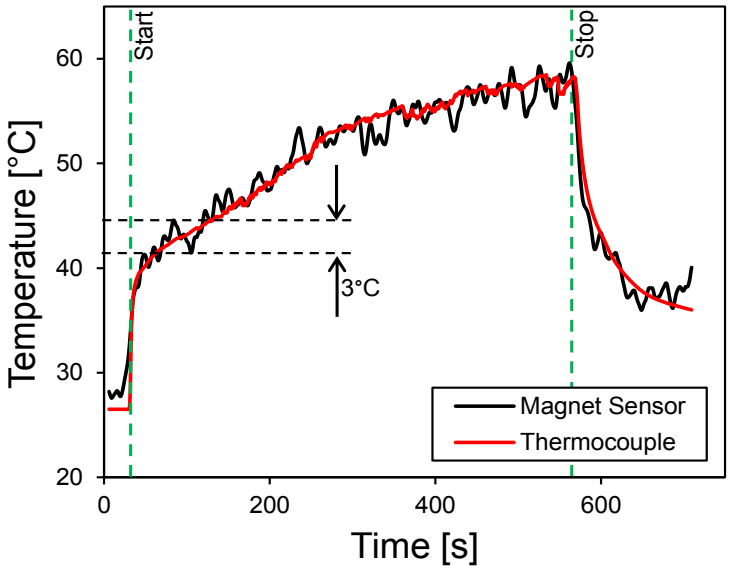

Fig. 4.6. Averaged magnet sensor measurement and thermocouple data vs. time (dynamic operation). The temperature displayed by the magnet sensor follows the thermocouple closely.

pensate for piece-to-piece variation in the seal housing/flange and minor variations in the magnet and Hall Effect sensor positioning. The tester was operated at 1800 rpm and 12 bar water pressure. Figure 4.6 shows the time based result for the magnet sensor and the thermocouple. These results show excellent congruity. The magnet sensor is able to respond to fast transients during starting and stopping of the test rig. The noise in the magnet sensor output is possibly due to the low resolution of the data acquisition card (16-bit ADC), inherent noise in Hall Effect sensor and system vibrations. This noise can be reduced with better data acquisition system that has high internal ADC resolution and amplification, software based averaging and filtering. The processed measurement data with averaging shows noise induced variation of 2-3°C in comparison to thermocouple as shown in Figure 4.6. In terms of seal health 2-3°C variation is negligible as pump operators look for fast transient changes that are in order of 15-35°C for fault conditions. Such fault conditions generally occur when either seal surface is damaged or fluid film between the sliding surface is ruptured [35].

4.4 Conclusion

In this chapter, the author has successfully demonstrated a wireless temperature sensor operating within a metallic enclosure to detect temperature of a mechanical face seal. Stationary tests show excellent results up to 80°C. The sensor concept was verified on a mechanical seal test rig. The magnet sensor response closely followed the thermocouple during dynamic testing proving the applicability of the sensor concept. As a possible extension for the future, the sensor will be tested with an improved data acquisition system to reduce the noise-induced uncertainty in the sensor output. Furthermore, long term tests may be performed on the seal test rig as well as on a hot plate to estimate sensor lifetime and reliability under various simulated conditions.

5. SENSOR IMPLEMENTATION USING CYLINDRICAL MAGNETS

This chapter discusses the implementation of wireless temperature sensor using a cylindrical magnet. Section 5.1 discusses the selection of cylindrical magnets and effect of the magnet dimensions on sensor performance. Furthermore, Section 5.2 compares results presented in previous chapters and discusses about the source of hysteresis in the measurements.

5.1 Sensor implementation

The semi-cylindrical magnet shown in Chapter 4 is subjected to heat when placed in a seal only from the convex surface. An improvement of this design is using cylindrical magnets inserted in a cavity drilled on the seal. This method ensures better response time as magnet is uniformly heated from all sides. Additionally, this design protects the magnet surface from the corrosive fluids that may exist in pumps. To find optimum dimensions of the cylindrical magnet such that they have reasonable permeance coefficient while keeping the magnet small enough for implementation in seals, we selected four L38EHT magnets with sizes shown in Table 5.1.

Figure 5.1 shows the test setup for sensor implementation with cylindrical magnets. An aluminum block with width and height similar to a mechanical seal is fabricated. Three holes with diameters 2 mm, 3 mm and 4 mm are drilled from top as shown with depths of 5 mm each. The cylindrical magnets are first annealed at 110°C for one hour and then placed in these holes (one magnet at a time) for sensor testing. Furthermore, the holes are filled with thermally conductive silicone paste (non-adhesive) for improved thermal contact. The magnets are positioned such that HAL 825 Hall Effect sensor responds to the horizontal component of the magnetic

Table 5.1
Cylindrical magnet dimensions

Number	Diameter (mm)	Length (mm)
1	2	4
2	3	4
3	3	5
4	4	5

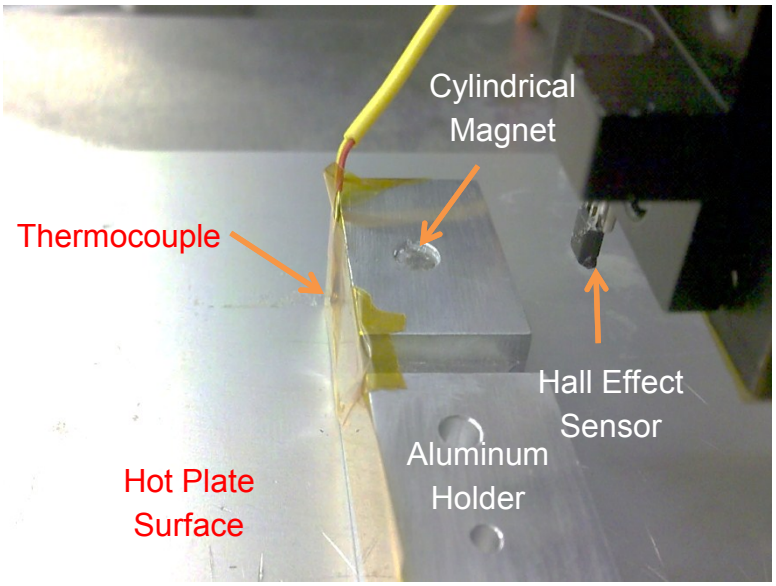

Fig. 5.1. Cylindrical magnet and Hall Effect sensor arrangement with respect to aluminum holder and hot plate.

field lines emanating from the magnet's South Pole which is similar to the sensor principle shown in chapter 4. HAL 825 Hall Effect sensor output is captured using high resolution Agilent multimeter [36]. A thermocouple is attached to the aluminum holder as shown for reference temperature measurement. The distance between the magnet and Hall Effect sensor is set at 11 mm for magnet 1 and 2. This arrangement mimics the sensor installation in a mechanical seal and flange. For magnets 3 and

4, the Hall Effect-magnet distance is fixed at 15 mm to avoid saturation of the Hall Effect sensor output due to the large magnetic field from these larger magnets. The hot plate is cycled from 10°C to 90°C with 40 minutes rise-time, fall-time and stable temperature. The data are recorded using PC and LabVIEW system [27].

5.1.1 Results and discussion

Figures 5.2, 5.3 show the measurement results for the 4 cylindrical magnets. Each of the magnets show linear trend with respect to temperature measured by thermocouple with excellent curve fit value. The response of magnet 1 is noisy compared the response of magnets 2, 3, 4. The variation in the magnetic field and corresponding variation in Hall Effect sensor output for the complete temperature range is also lowest for magnet 1. This variation increases with magnet dimensions. For a temperature sensor it is desirable to have the maximum possible variation in the sensor output for a given temperature range with minimum noise. But, in applications such as mechanical seals where magnet-Hall Effect sensor distance is fixed and space available for the magnet is extremely constrained, additional hardware and software signal processing may be required for satisfactory sensor resolution and sensitivity. Based on these results we can conclude that magnet 3 and 4 are more suitable for mechanical seal application as they provide better signal-to-noise ratio with reasonable dimensions.

5.2 Hysteresis

In results shown in Chapter 2 and 3, hysteresis was observed between thermocouple and hall effect sensor output. Figure 5.4 shows test setups and results for rectangular magnet stack implementation, bearing sensor implementation, mechanical seal sensor and the cylindrical magnet implementation. An interesting phenomenon is observed when all the graphs and setups are observed together. The hysteresis in the sensor outputs reduces from setup (a) to setup (d). In setup (a) the magnets are heated from one side of the stack and the heat travels from base of the lowest magnet

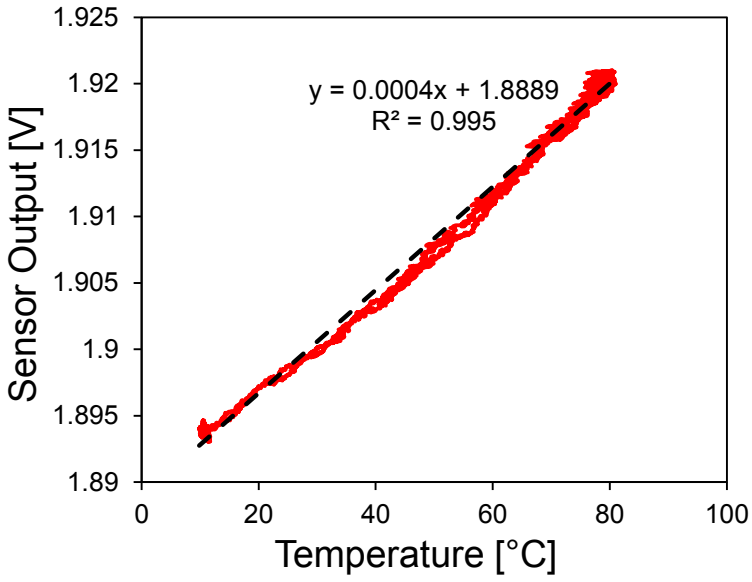

(a)

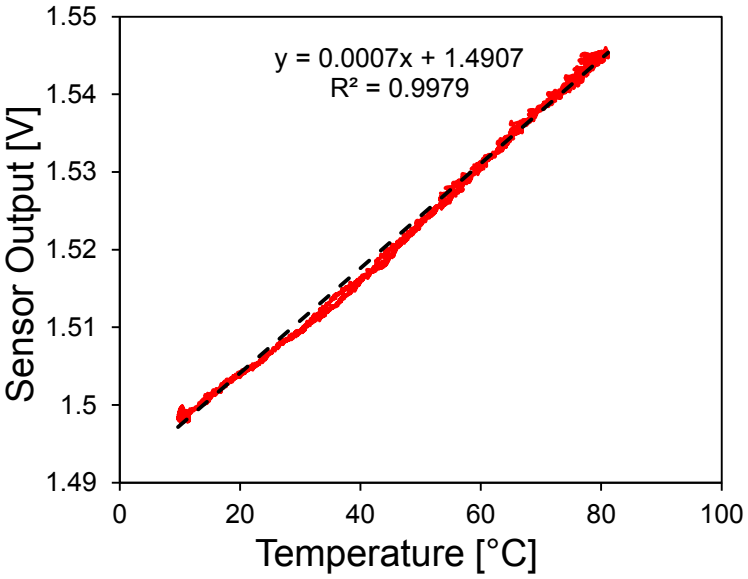

(b)

Fig. 5.2. (a) Measured sensor output vs. temperature for 2 mm diameter 4 mm length magnet. (b) Measured sensor output vs. temperature for 3 mm diameter 4 mm length magnet.

to top of the stack. In case of bearing sensor implementation, the ring magnet is heated from the bottom side that is in contact with the bearing's inner race. Mag-

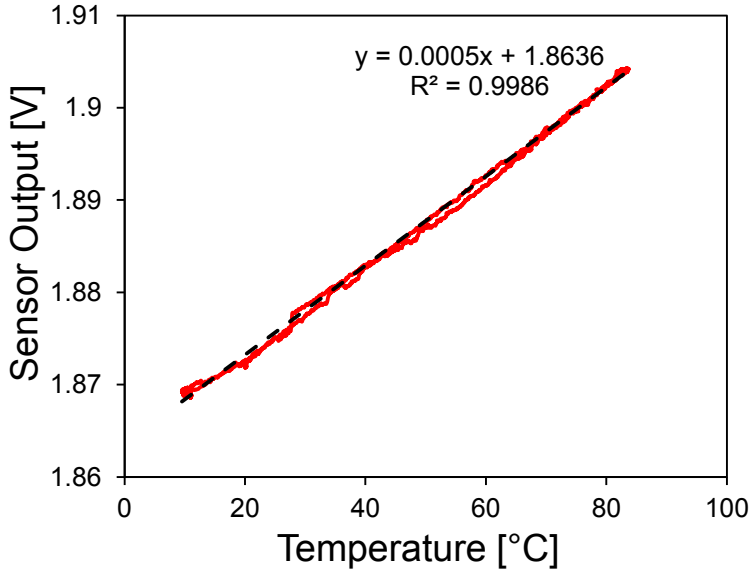

(a)

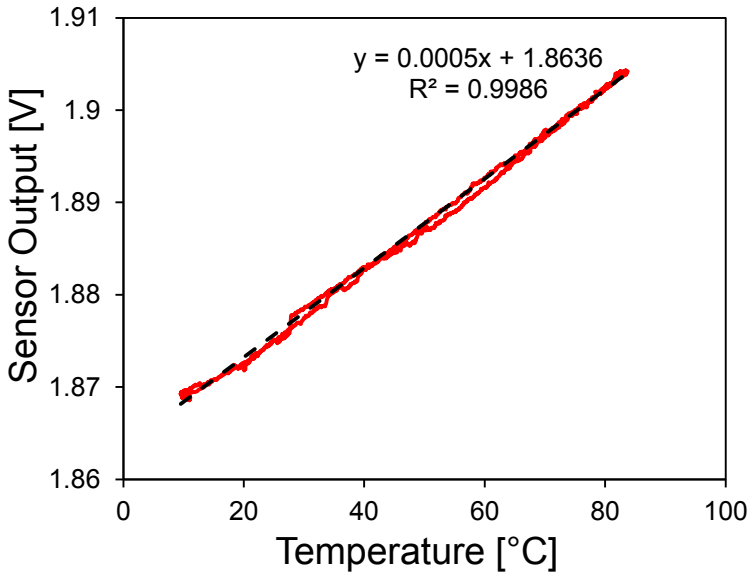

(b)

Fig. 5.3. (a) Measured sensor output vs. temperature for 3 mm diameter 5 mm length magnet. (b) Measured sensor output vs. temperature for 4 mm diameter 5 mm length magnet.

nets are generally poor thermal conductors hence they take longer to reach expected temperature. When magnets are heated only from single side, they take longer to re-

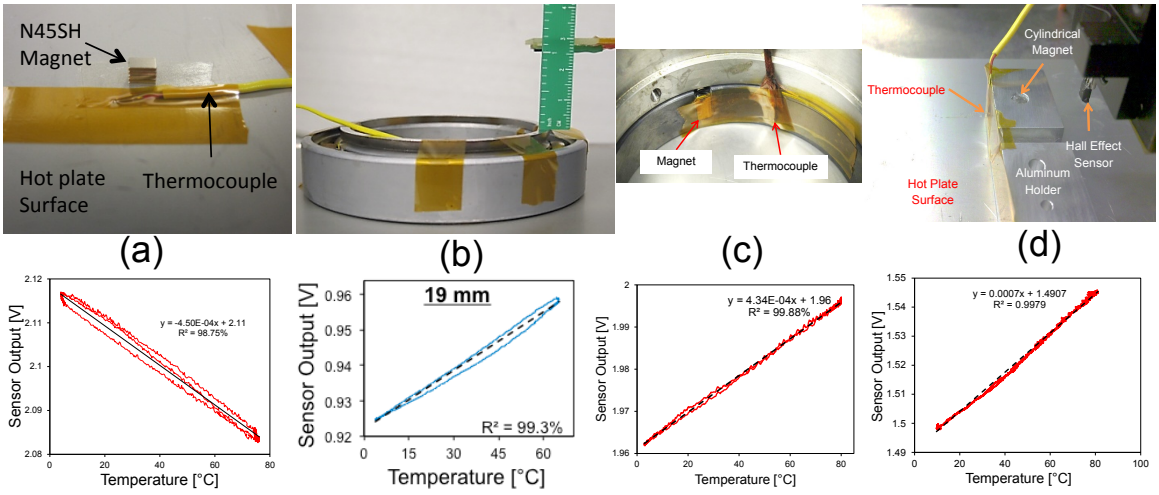

Fig. 5.4. Figure showing the four different test setups and their measurement results. An important point to be noticed in this image is reduction in hysteresis from setup (a) to setup (d).

spond to thermal changes. On the other hand, the reference thermocouple's metallic contact area is less than 0.5 sq. mm. Thus thermocouple can almost instantaneously respond to temperature variation. This difference in response time leads to magnet sensor readings lagging the thermocouple readings resulting in measurement hysteresis. In case of the mechanical seal sensor implementation, the magnet is heated from convex side and for the cylindrical magnet, the magnet is heated from all sides simultaneously. This enhances the thermal conduction rate of the magnet and thus magnet is able to respond to thermal changes at the same rate as thermocouple. Hence no hysteresis is observed for later mechanical seals and cylindrical magnets. As a recommendation for improvement in the bearing sensor application, the magnet needs to be concealed on the inner race for better thermal conduction. This is possible by machining a circular slot on the bearing inner race.

5.3 Conclusion

In this chapter, an improvement for mechanical seal sensor is presented using cylindrical magnets with relevant results. All the cylindrical magnets showed excellent linear results with no hysteresis. Furthermore, the cause of hysteresis in bearing sensor implementation is identified and a possible solution for bearing sensor is suggested.

6. SIMULTANEOUS MEASUREMENT OF TEMPERATURE AND VIBRATION

This chapter proposes a novel concept of simultaneous measurement of temperature and vibration using a combination of a permanent magnet and a Hall Effect sensor placed at a fixed distance relative to each other. A temperature sensor based on thermal-induced magnetic field change in permanent magnets has been presented by [21]. This sensor concept has been successfully implemented for bearing inner race temperature measurement in [37]. This chapter extends the wireless temperature measurement concept to simultaneously measure temperature and vibrations. The temperature-induced magnetic field change in permanent magnet results in a slow moving DC signal as Hall Effect sensor output. If the magnet is subjected to vibrations, the relative distance between magnet and Hall Effect sensor changes resulting in periodic AC signal superimposed on DC signal in the Hall Effect sensor output. The AC and DC signals can be separated by suitable electrical signal processing and temperature as well as vibration of a hot vibrating surface can be deduced remotely. This concept is illustrated in Fig. 6.1 This chapter is divided as follows: Section 6.1 discuss the sensor implementation using a semi-cylindrical magnet and a Hall Effect sensor, Section 6.2 present test result for temperature and vibration measurements.

6.1 Sensor implementation

To implement simultaneous temperature and vibration measurement, we have selected the Micronas HAL 825 Hall Effect sensor. The Hall Effect sensor is programmed to a sensitivity of 70 mV/Gauss. A semi-cylindrical shaped 4.4-mm diameter, 9.5-mm length L38EHT magnet is selected for sensor implementation. This magnet is

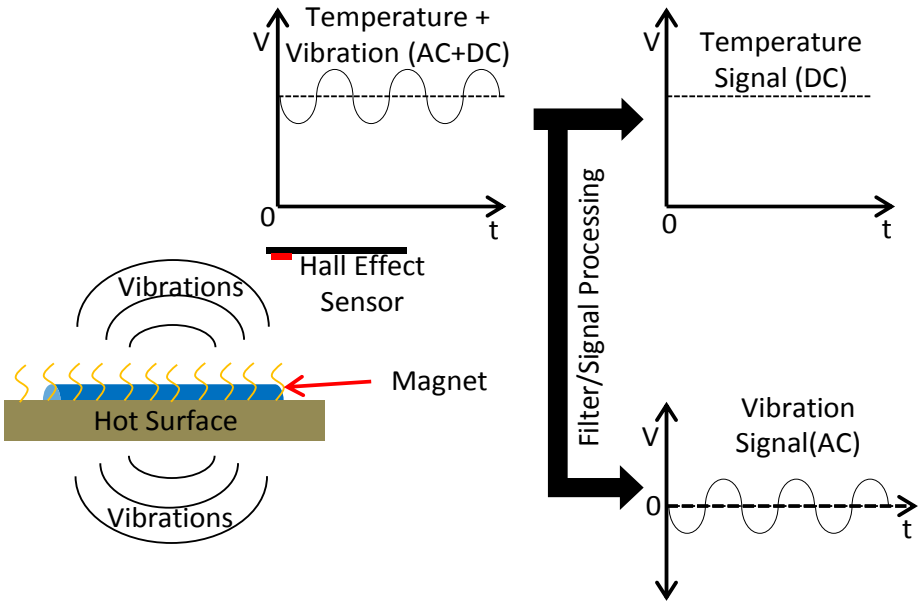

Fig. 6.1. Illustration of the sensor concept

polarized along its length with temperature rating of 200°C, coercivity of 2388 KOe and B-H product of 38 MGOe.

Figure 6.2(a) shows a semi-cylindrical magnet attached to a custom fabricated aluminum holder. The aluminum holder maintains uniform temperature across the magnet volume. The holder is attached to the hot plate using double-sided tape. A thermocouple is attached to the holder as shown for reference temperature measurement. The Hall Effect sensor is mounted on a small PCB. In a typical measurement system the magnet will be attached to a vibrating hot surface; however, in this case it is difficult to introduce vibrations on the magnet directly due to the size and weight limitations of the hot plate. Therefore, to demonstrate simultaneous measurement of temperature and vibration, the Hall Effect sensor PCB is attached to a piezoelectric actuator. This unique assembly is mounted on a Z-axis setup at a distance of 13-mm from the the magnet's south pole. The Hall Effect sensor measures vertical component

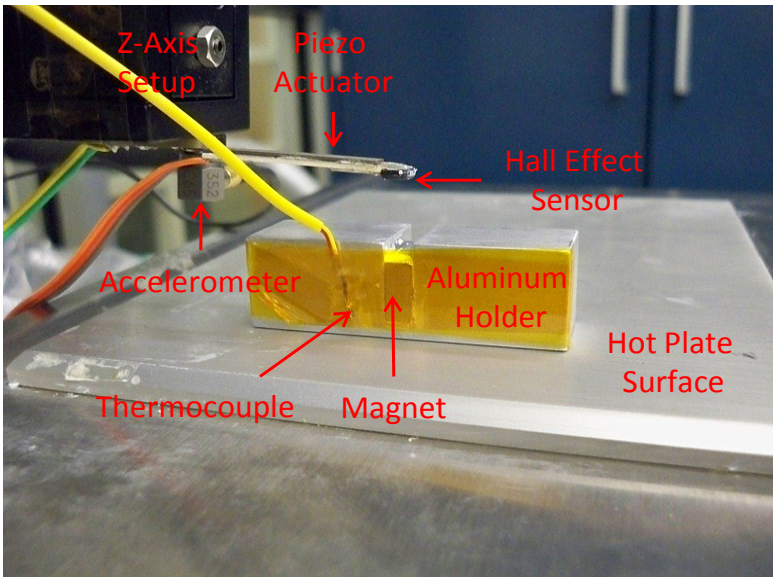

(a)

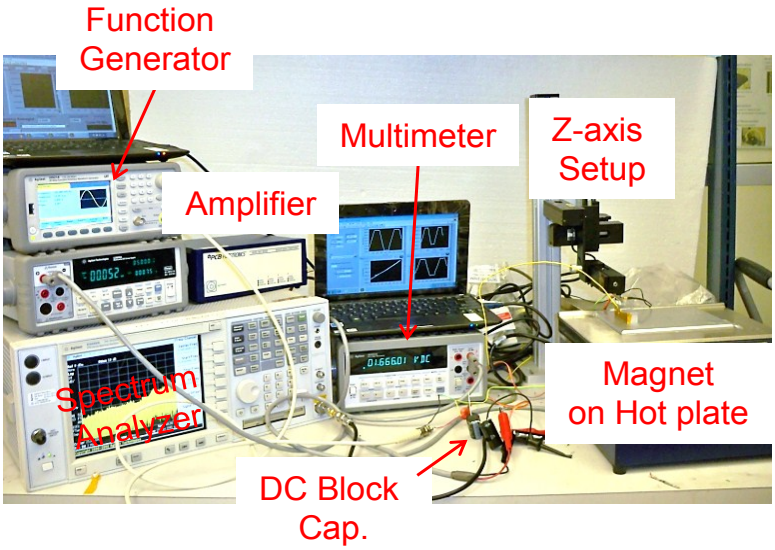

(b)

Fig. 6.2. (a) Magnet attached to the aluminum sensor holder and holder kept on the hot plate. (b)Complete measurement setup.

of the magnetic field lines originating at the magnet's south pole. The piezoelectric actuator is connected to a signal generator to induce vibrations. When the piezoelectric actuator is excited at certain frequency, the Hall Effect sensor's position changes

periodically with respect to the magnet. These vibrations are detected by capturing the AC component in the Hall Effect sensor output using a spectrum analyzer. The Hall Effect sensor output is connected to a spectrum analyzer through a large DC blocking capacitor for vibration signal measurement. This output is also connected to a multi-meter without DC block for temperature measurement. A standard accelerometer with sensitivity of 100 mV/g is attached to the Z-axis setup as shown in Figure 6.2(b) for reference. The data are recorded on a PC using LabVIEW [34]. The hot plate temperature is cycled from 10°C to 90°C with rise time, fall time and

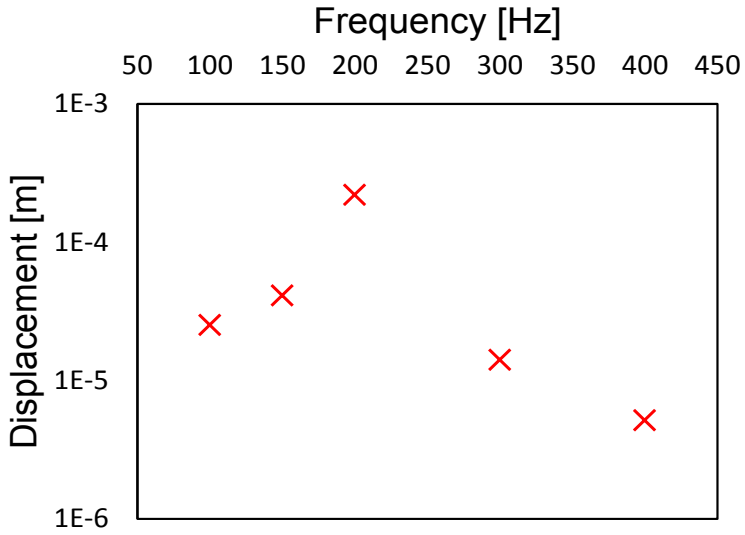

Fig. 6.3. Measured piezoelectric actuator displacement vs. frequency.

constant temperature time of 40 minutes each. The piezoelectric actuator has rated displacement of 315 μm at $\pm$90 Vp-p excitation. In this setup, the piezoelectric actuator is excited using a function generator at $\pm$10 Vp-p resulting in measured tip displacement of 218 μm at resonance. Figure 6.3 shows measured displacement of the piezoelectric actuator with Hall Effect sensor at various excitation frequencies. These measurements are performed using a Polytec Laser doppler vibrometer [38]. Although the specified resonant frequency of the stand-alone piezoelectric actuator is 272 Hz, this resonant frequency is reduced to 200 Hz as the beam is loaded with the Hall

Effect sensor PCB. The piezoelectric actuator is subjected to multiple frequencies to capture a wide response spectrum.

6.2 Results

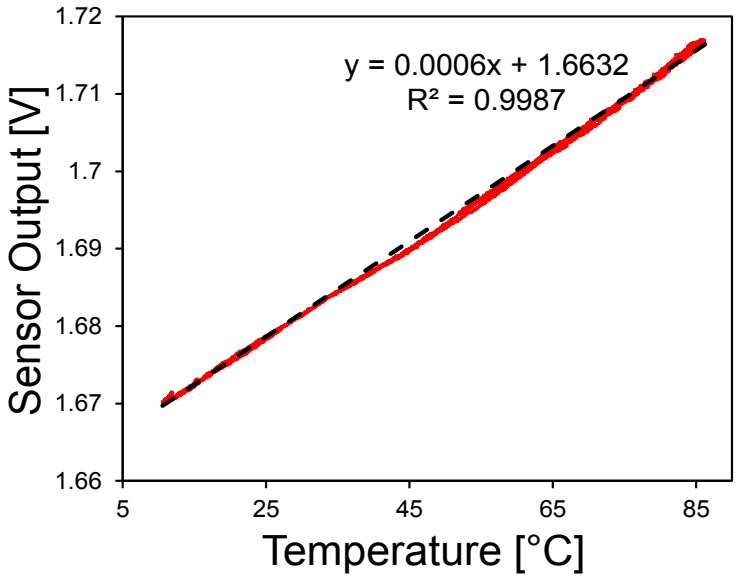

Fig. 6.4. Measured Hall Effect sensor output vs. temperature.

Figure 6.4 shows the measured Hall Effect sensor output vs. temperature from 10°C to 85°C. The measurements show linear trend with curve fit value of greater than 98%. These results are in accordance with results presented by [21].

Figure 6.5(a) and 6.5(b) show the vibration measurement spectra for the magnet sensor and accelerometer. The magnet sensor is able to detect all frequencies applied to the piezoelectric actuator with high accuracy. An important point to be noticed in the graphs is the amplitude of the signals at various frequencies. The magnet sensor acts as displacement sensor, resulting in the measured amplitude being proportional to the actual displacement of the Hall effect sensor with respect to the magnet. Hence, a large amplitude signal is observed at the resonant frequency of 200 Hz.

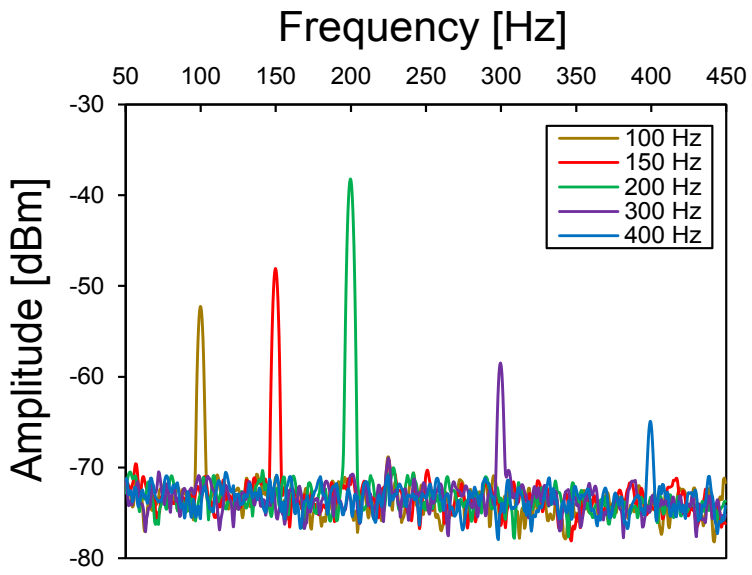

(a)

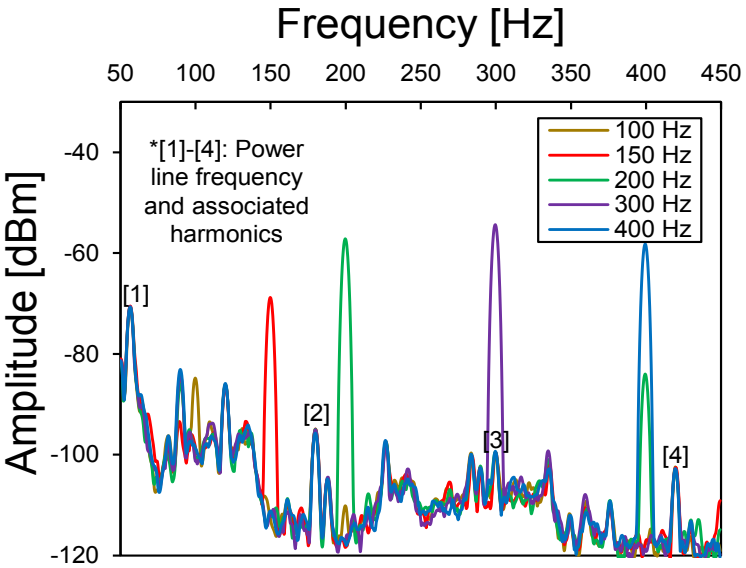

(b)

Fig. 6.5. (a) Measured vibration spectrum for magnet sensor. (b) Measured vibration spectrum for accelerometer. The magnet sensor acts as displacement sensor similar to a proximity probe while accelerometer measures vibrations as equivalent acceleration.

Although, the accelerometer measures the same frequency components as shown in Figure 6.5(a) & 6.5(b), the measured amplitude is proportional to the accelera-

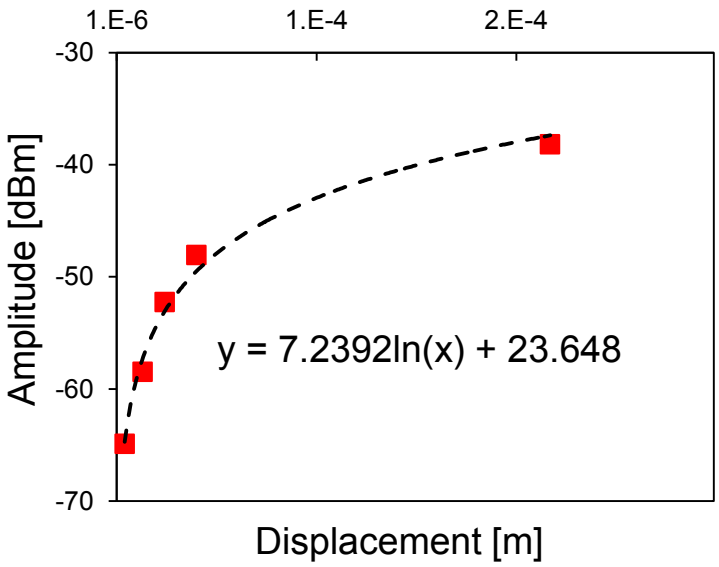

Fig. 6.6. Measured Hall Effect sensor output vs. measured displacement. The inherent noise of the Hall Effect sensor limits the the vibration measurement range at 1.5 μm.

tion at the fixed end of the piezoelectric actuator on the Z-axis setup. Additionally, the accelerometer spectrum shows various power line frequencies and associated harmonics with the frequency dependent noise floor which varies from -80 dBm to -120 dBm. These line frequencies and noise floor variations are likely introduced by the accelerometer signal processor (Figure 6.2(b)) and are absent in the magnet sensor output.

Figure 6.6 shows the measured amplitude from Hall Effect sensor vs. piezoelectric actuator displacement. The Hall Effect sensor has inherent noise of -72dBm. This noise limits the dynamic measurement range of the Hall Effect sensor- magnet configuration. By using the curve fit equation shown in Figure 6.6 the lower limit for the displacement measurement range is calculated to be 1.5 μm for the magnet-Hall Effect sensor distance of 13 mm.

6.3 Conclusion

In this chapter, the author has successfully demonstrated a wireless sensor capable of measuring vibrations and temperature simultaneously using a permanent magnet and a Hall Effect sensor. The temperature measurements showed a linear trend up to 85°C for a magnet-Hall Effect sensor distance of 13 mm. Furthermore, the magnet sensor detected all vibration frequencies, as also identified by an accelerometer with a high degree of congruity. The magnet sensor's vibration spectrum showed better signal-to-noise ratio than the accelerometer's one.

7. SENSOR RELIABILITY

This chapter discusses sensor reliability and its dependance on magnet properties. Section 7.1 summarizes the effects of permeance coefficient and physical dimensions on magnet lifetime. Section 7.2 discusses various test setups and results for subjecting magnets at various temperatures and thermal cycling. Additionally, Section 7.2.5 gives a detailed analysis of thermal effects on magnet lifetime.

7.1 Permeance coefficient

An essential property of permanent magnets is their time-dependent loss in magnetic field strength. This degradation depends upon the magnet type, material, coercivity, permeance coefficient and operating temperature [33], [39]. Permanent magnets can be used for long durations at high temperatures without any significant time-based loss if they have high permeance coefficient, high coercivity and operating temperatures are significantly below the Curie temperature [22]. Coercivity of the magnet is defined as ability of the magnet to oppose demagnetization. It is a material property which is hard to control considering the fact that these magnets are procured commercially. Permeance coefficient (P_c), also called the load-line, B/H or operating slope of a magnet, is the line on the demagnetization curve where a given magnet operates. Its value depends on both the shape of the magnet, and it's surrounding environment. In practical terms, it is a number that define how hard it is for the field lines to go from the north pole to the south pole of a magnet. A tall cylindrical magnet will have a high P_c, while a short, thin disc will have a low P_c [40]. Permeance coefficient of a given magnet is calculated using Equation 7.1

$$P_c = -\frac{K_1}{K_2} \times \frac{A_g \times L_m}{L_g \times A_m} \tag{7.1}$$

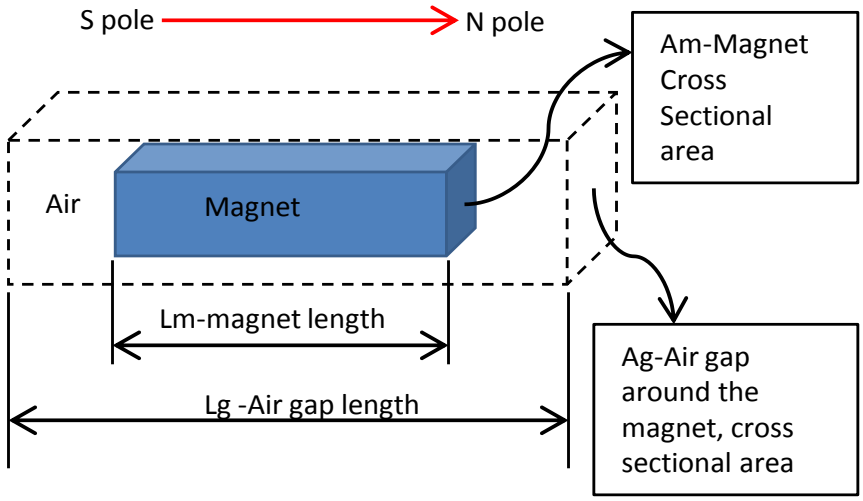

Fig. 7.1. Illustration showing various dimensions of magnet used to calculate the permeance coefficient.

Figure 7.1 defines the various variables used in Equation 7.1. K_1 and K_2 are dependent on the external magnet circuit that may form in the presence of magnetic materials and are equal to unity for stand alone magnets. Thus, the P_c value only depends on the physical dimensions for a magnet held in air [41].

The permeance coefficient values for a rectangular, ring-shaped and cylindrical magnets are calculated by Equations 7.2, 7.3 and 7.4 respectively [41]

$$P_c = \frac{1.77 \times L_b}{W \times T} \sqrt{2 \times (W + T) + W \times T} \tag{7.2}$$

$$P_c = \frac{4 \times L_r}{D_o^2 - D_i^2} \sqrt{\frac{L_r \times (D_o + D_i)}{2} + \frac{D_i^2 + D_i^2}{4}} \tag{7.3}$$

$$P_c = \frac{L_c}{R^2} \sqrt{R \times (R + L_c)} \tag{7.4}$$

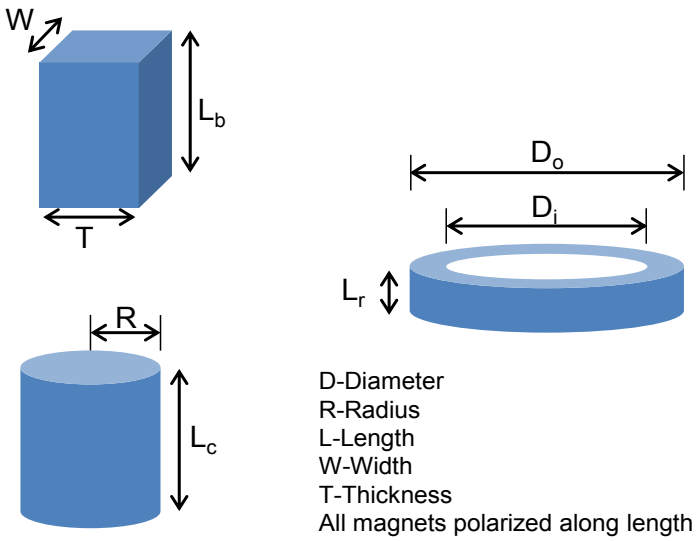

Fig. 7.2. Illustration showing description of various magnet dimensions

Figure 7.2 defines various dimensions used for calculating the permeance coefficients of different magnet shapes. The calculated permeance coefficient of the rectangular magnet shown in chapter 2 is 3.2, while the permeance coefficient of the ring magnet in chapter 3 is 1.65. As the ring magnet is mounted on a ferrous bearing, the length of the magnet is approximated to be twice the physical length resulting in the overall permeance coefficient value of 3.5 for the complete assembly [42]. Similarly, the estimated permeance coefficient of the semi-cylindrical magnet shown in chapter 4 is 16.36. This estimation is performed by calculating the permeance coefficient of a cylindrical magnet with the same cross-sectional area.

7.2 Magnet lifetime

Magnet lifetime is critical for long-term operation of the sensor in mechanical seal applications. A typical mechanical seal is replaced after about 5 years in operation [35]. For reliable sensor operation, it is desirable that magnet the embedded exceeds the seal's lifetime. This typically requires a minimum reduction in the magnetic field

strength. Implementing a long term setup for lifetime characterization is challenging for long durations (months-years). Alternatively useful estimations may be obtained by subjecting magnets to temperatures that are higher than the specified application limits for relatively short durations. The magnetic field strength is then continuously measured and lifetime is extrapolated for that given temperature. A similar method has been proposed by Haavisto et al. where they studied the effect of permeance coefficient on temperature-induced magnetic field strength losses for various grades of Nd-Fe-B magnets [33]. In their research, they observed only 1-3% loss in the magnetic field strength after 10,000 hours at 80°C and 150°C for P_c values of 3.3. They further estimated the magnet lifetime up to 30,000 hours by extrapolating the 10,000 hours measurement data. In this research we have performed a similar study for smaller cylindrical and rectangular (N45SH and L38EHT grade) magnets at various temperatures from 25°C to 130°C.

7.2.1 Short term tests on rectangular magnets

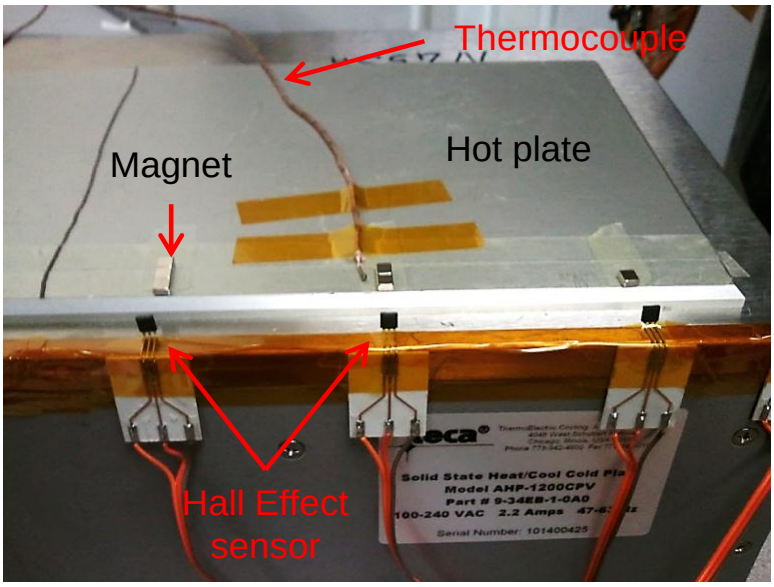

Fig. 7.3. Test setup for magnet lifetime measurement for rectangular magnets.

Table 7.1
Rectangular magnet dimensions and P_c values

Grade	Length (mm)	Width (mm)	Thickness (mm)	P_c
N45SH	4.7	5	2	6.26
N45SH	9.4	5	2	16.69
N45SH	14.1	5	2	30.02
L38EHT	4.7	5	2	6.26
L38EHT	9.4	5	2	16.69

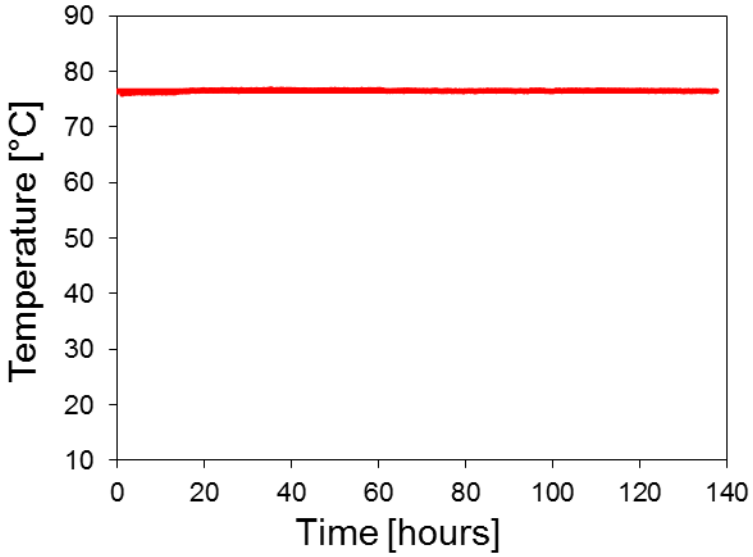

Fig. 7.4. Hot plate surface temperature vs. time

We performed short term tests on various permeance coefficient values of rectangular N45SH and L38EHT grade magnets. The magnets are tested at a constant temperature of 75°C for 140 hours. The test setup is shown in Figure 7.3. Three P_c values of N45SH and two permeance coefficient values of L38EHT grade magnets are attached to a hot-cold plate using thermally conductive epoxy. The magnet dimensions and P_c values are shown in Table 7.1. Various permeance coefficient values are achieved by attaching the magnets in series along their polarization direction. The

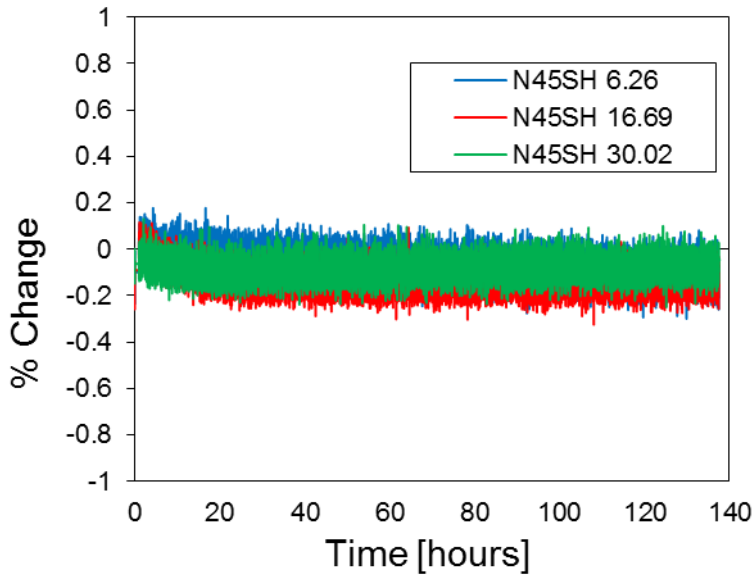

(a)

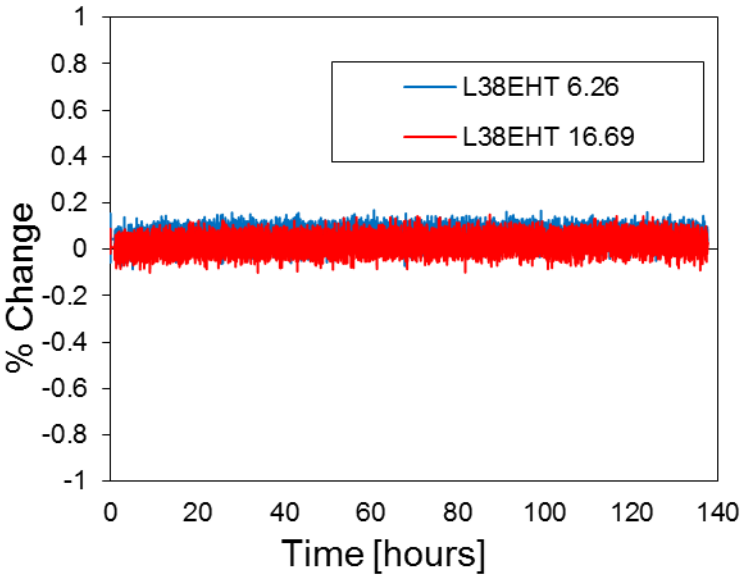

(b)

Fig. 7.5. (a) Magnetic field change vs. time for the N45SH magnet for various permeance coefficient values. (b) Magnetic field change vs. time for the L38EHT magnet for various permeance coefficient values.

individual block magnets are 5-mm wide, 2-mm thick and 4.7-mm long and are magnetized along length. The HAL825 sensors are mounted on the hot plate as shown

in Figure 7.3 for magnetic field strength measurements [32]. Two thermocouples are attached to monitor the hot plate temperature. The data is captured continuously using LabVIEW data acquisition card and a PC [27].

Figure 7.4 shows the hot plate temperature vs. time graph. Figures 7.5(a) and 7.5(b) show time-based loss in the magnetic field strength at 75°C. The slope of the measurements remains nearly flat for a constant temperature of 75°C indicating minimum time based loss at high temperature. This is true for both magnet grades and all tested permeance coefficient values. The noise in the sensor output is due to inherent noise from Hall Effect sensor and possibly due to limited resolution of the data acquisition card.

7.2.2 Short term tests on cylindrical magnets

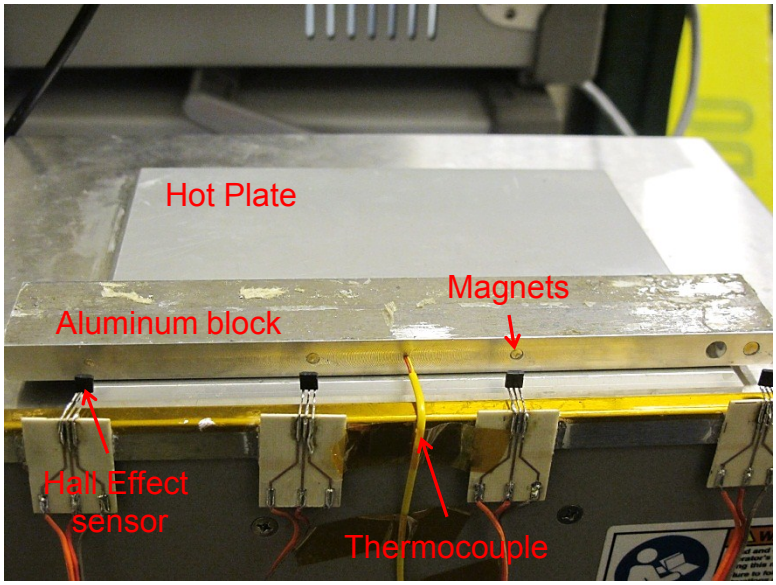

Fig. 7.6. Test setup for magnet lifetime measurement for cylindrical magnets.

Figure 7.6 shows the test setup for studying magnetic field strength losses at temperatures ranging from room temperature to 90°C. The cylindrical L38EHT magnets presented in the previous chapter are placed in cylindrical holes drilled in an alu-

minum block as shown in Figure 7.6. The physical dimensions and P_c values for cylindrical magnets are shown in Table 7.2. The aluminum block is attached to a TECA hot-cold plate using double-sided adhesive tape. The magnets are preheated at 120°C for an hour to stabilize potentially unstable magnetic domains. The Hall Effect sensors are placed at a fixed distance (8 mm to 11 mm depending on the magnet size) from the magnets. A thermocouple is attached to the aluminum block for reference temperature measurement. The hot plate temperature is varied from 25°C to 75°C in five steps. At each step, the temperature is kept constant for 48 hours to study the loss in magnetic field strength. Similar, to previous test setups the data are captured using a PC, a NI data acquisition card and LabVIEW [27].

Table 7.2
Cylindrical magnet dimensions and P_c values

Sr. Number	Diameter (mm)	Length (mm)	P_c
1	2	4	8.94
2	3	4	5.11
3	3	5	6.94
4	4	5	4.68

Observations

1. Figure 7.7 shows the hot plate temperature vs. time graph.

2. Figures 7.8 to 7.11 show the measured magnetic field strength vs. time graphs. The field strength changes almost instantaneously when temperature transitions from one stable regime to another for all magnets. This is an expected behavior as the field strength should change with temperature and ideally should remain constant when temperature is stable.

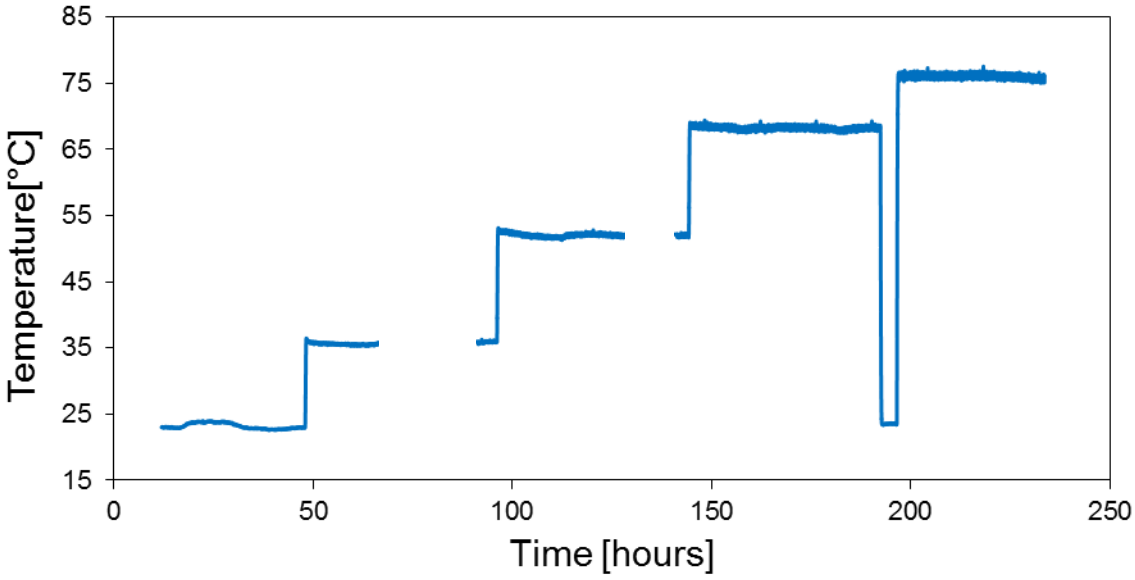

Fig. 7.7. Measured hot plate temperature vs. time for short term measurement setup.

3. Figure 7.8 shows temperature and magnetic field strength vs. time for the 2 mm diameter 4 mm long magnet. The magnetic field strength decreases continuously with time during stable temperatures regimes. This loss is observed as a negative slope in the field strength graph during the stable temperature regimes.

4. Figures 7.9 to 7.11 show magnetic field strength vs. time for magnets of D=3 mm L=4 mm, D=3 mm L=5 mm, D=4 mm L=5 mm respectively. The slope of the magnetic field strength graph for each of these magnets remains relatively flat when temperature is stable. This indicates minimum losses in magnetic field strength with time during stable temperature regimes. Few minor variations are observed in the Hall Effect sensor output. These variations are caused by fluctuations in the hot plate temperature arising due to minor changes in room conditions.

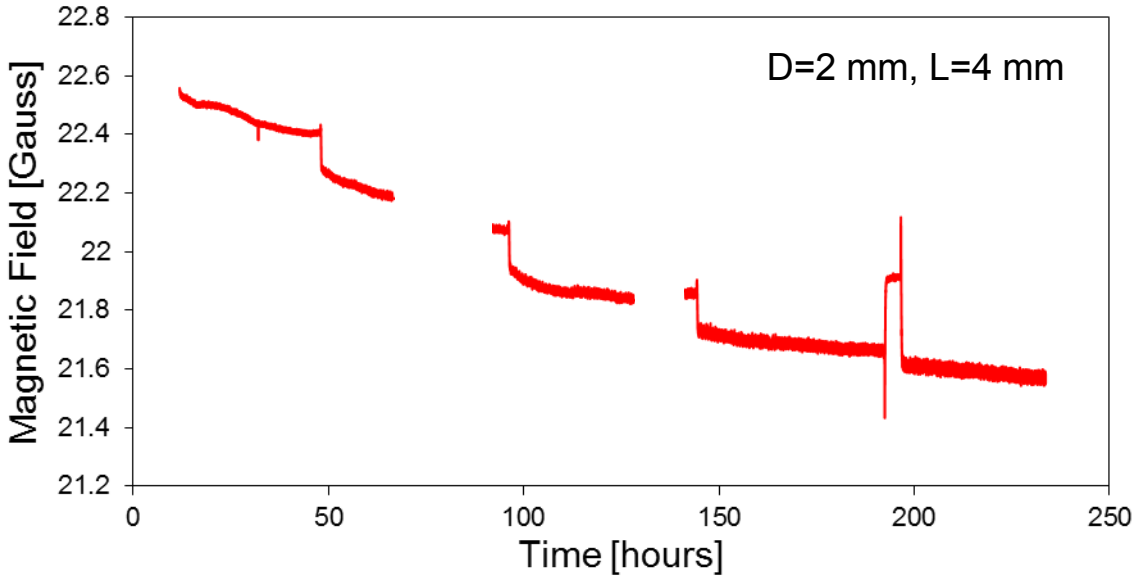

(a)

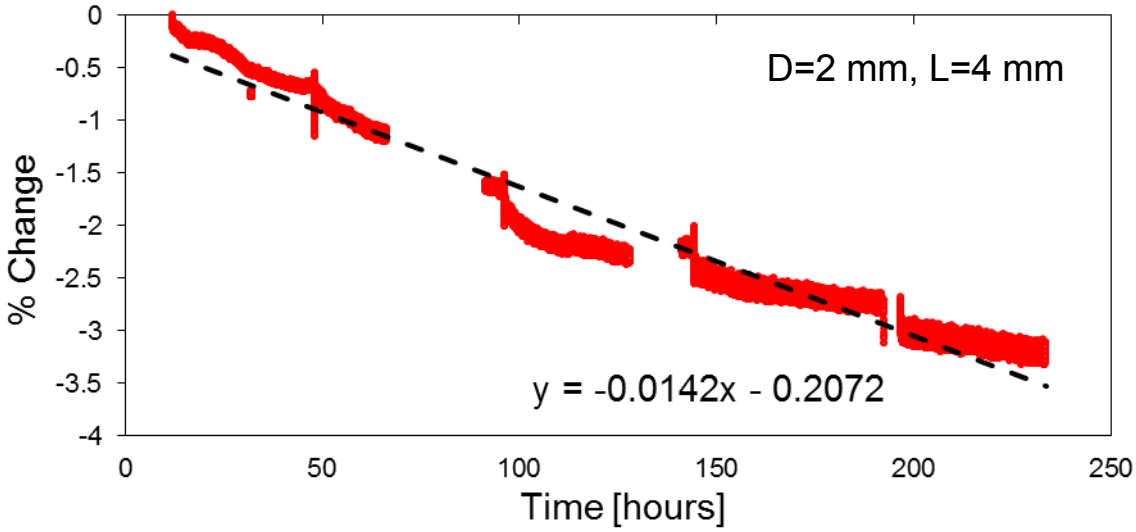

(b)

Fig. 7.8. (a) Measured magnetic field strength vs. time for 2 mm diameter, 4 mm length magnet. (b) Measured magnetic field strength change vs. time.

5. In Figures 7.8 to 7.11, there are two zones where the measurements discontinuities exist. These discontinuities were caused by a malfunction in the computer

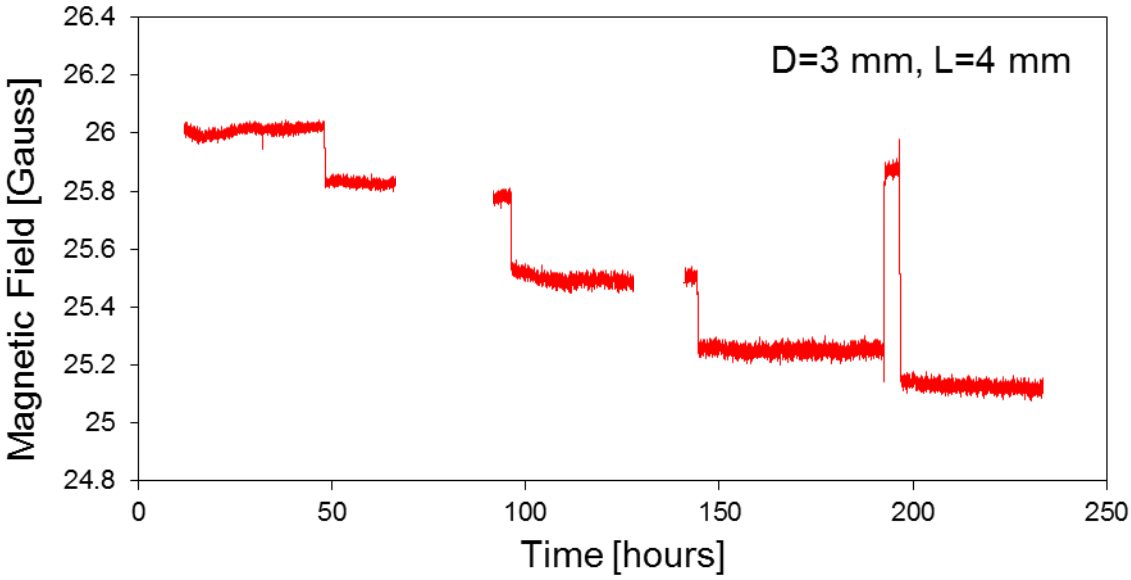

Fig. 7.9. Measured magnetic field strength vs. time for 3 mm diameter, 4 mm length magnet.

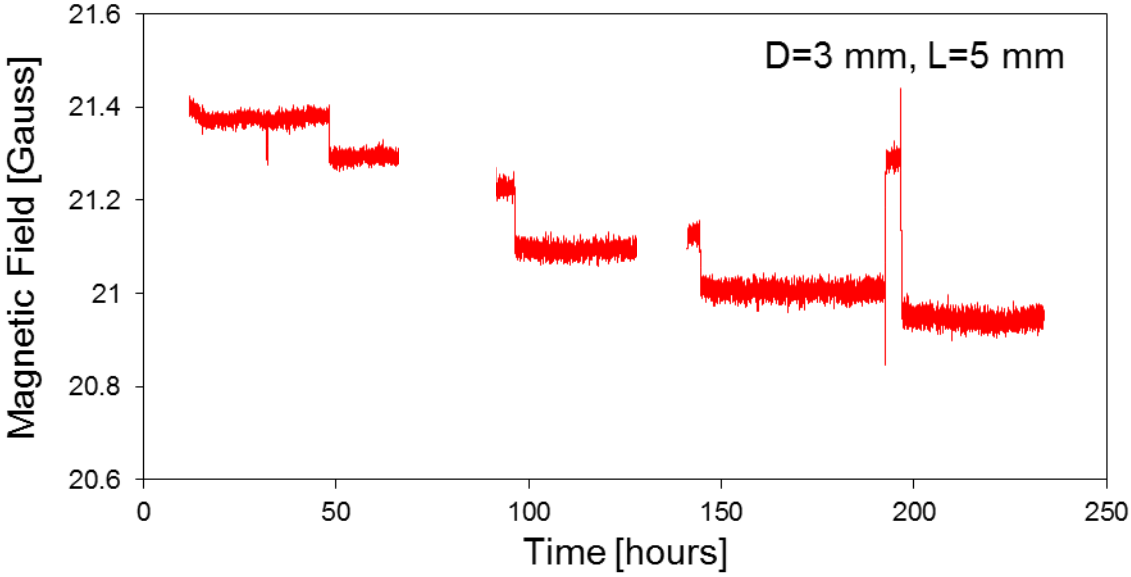

Fig. 7.10. Measured magnetic field strength vs. time for 3 mm diameter, 5 mm length magnet.

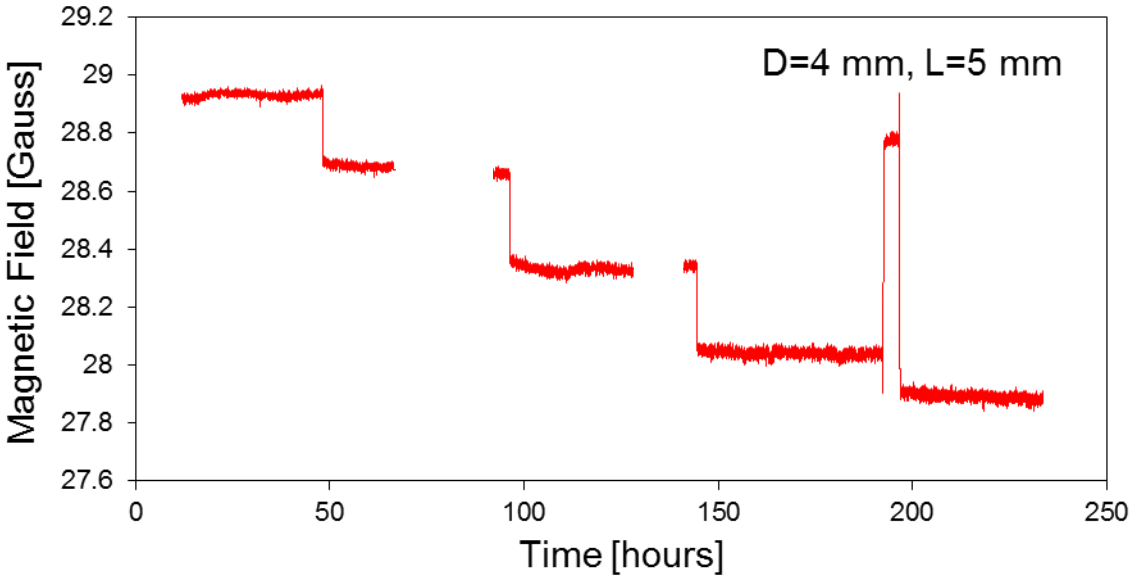

Fig. 7.11. Measured magnetic field strength vs. time for 4 mm diameter, 5 mm length magnet.

that was capturing the data. During this malfunction the hot plate continued to operate and maintain the constant temperatures. Hence when the system recovered there was no effect on the overall measurement trend.

7.2.3 Thermal cycling tests on cylindrical magnets

Another method of testing magnets for reliability is by subjecting them to continuous thermal cycling. The setup shown in Figure 7.6 is used for continuous thermal cycling tests. The hot plate temperature is varied from 5°C to 90°C with both rise and fall times set at 40 mins. In real-world operating conditions, the magnet will be rarely subjected to a continuous, symmetric thermal cycling where the temperature varies between two set points with identical rise time, fall time and stable regime. Hence, to randomize the temperature profile, the cycling trend is set to follow the trend shown in the inset on Figure 7.12. The magnets are selected from the same

batch used for the previous tests. These magnets are also subjected to 120°C for an hour to stabilize their magnetic domains.

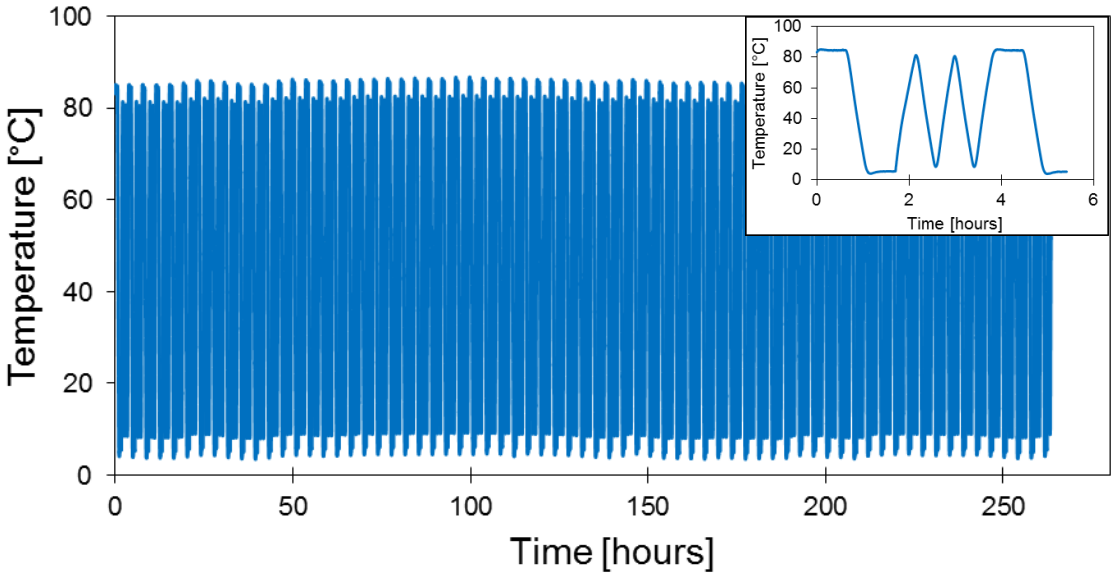

Fig. 7.12. Measured magnetic field strength vs. time for the 2 mm diameter, 4 mm length magnet.

Observations

1. Figure 7.12 shows hot plate temperature vs. time for 68 thermal cycles. Figures 7.13 to 7.14 show the measured field strengths vs. time for various cylindrical magnets. The temperature graph shows small overshoots when the thermal profile transitions from a rising/falling curve to stable regime. The magnetic field trends closely follow these thermal transitions indicating a linear response with temperature.

2. The linear curve fits in all measurement graphs have positive slopes indicating an increase in the magnetic field due to thermal cycling for all magnets.

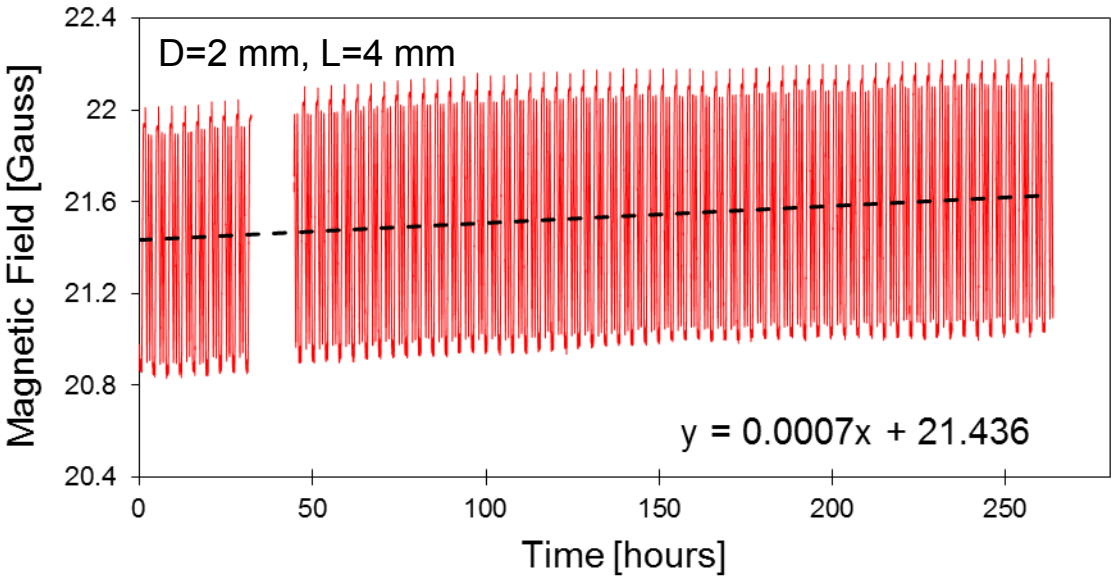

(a)

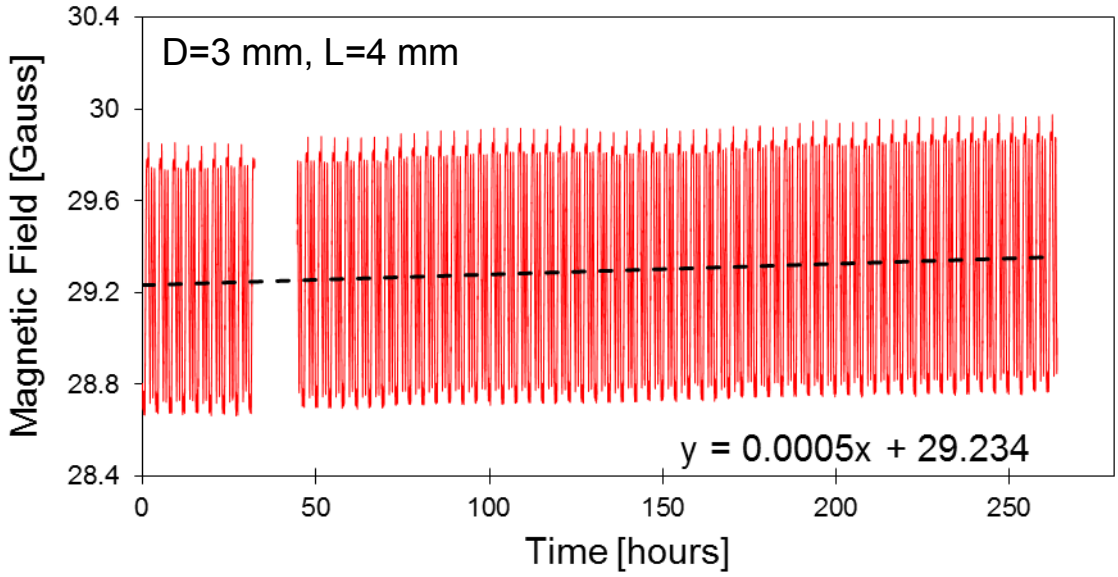

(b)

Fig. 7.13. (a) Measured magnetic field strength vs. time for 2 mm diameter, 4 mm length magnet. (b) Measured magnetic field strength vs. time for 3 mm diameter, 4 mm length magnet.

3. The magnetic field gain rate is the highest for the 2 mm diameter magnet and the lowest for the 4 mm diameter magnet.

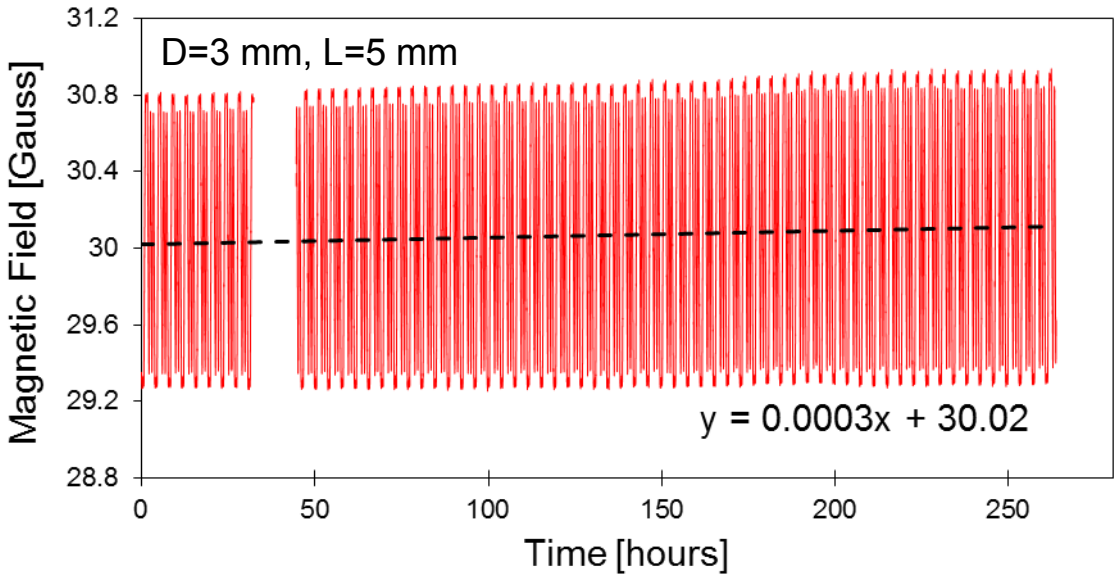

(a)

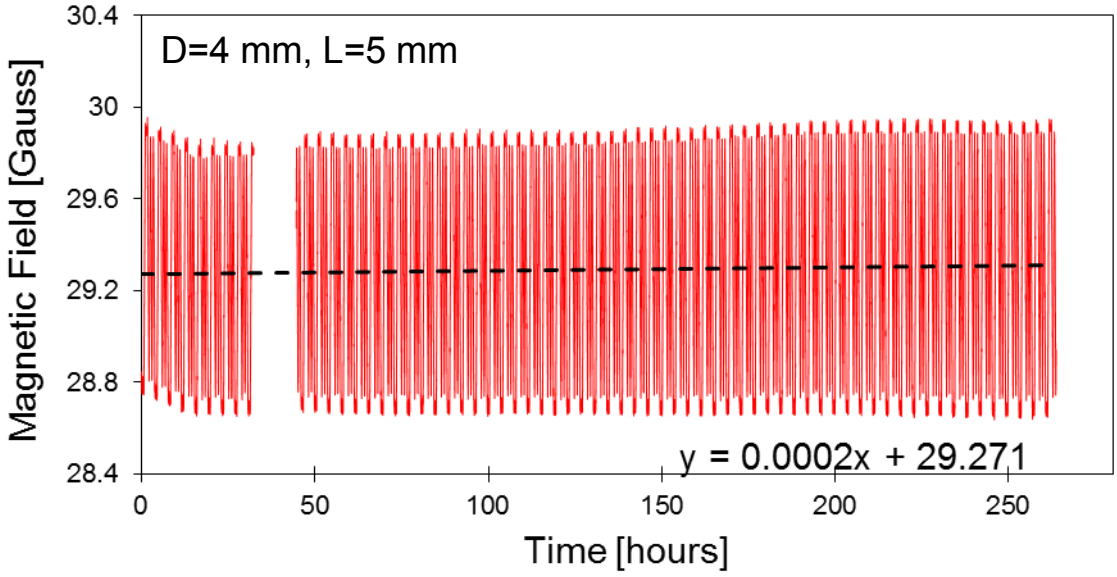

(b)

Fig. 7.14. (a) Measured magnetic field strength vs. time for 3 mm diameter, 5 mm length magnet. (b) Measured magnetic field strength vs. time for 4 mm diameter, 5 mm length magnet.

4. Figure 7.14(b) shows some initial drop in the magnetic field. This is possibly due to the physical expansion of the magnet at high temperature leading to

a minor change in the magnet-Hall Effect sensor distance. After 10 thermal cycles, this magnet seems to have stabilized in the aluminum block and showed an increase in magnetic field similar to the other magnets.

7.2.4 Long term tests on cylindrical magnets

Figure 7.15 shows the test setup for subjecting cylindrical magnets to high temperatures for long durations. The cylindrical magnets are placed in cylindrical holes drilled in an aluminum block as shown in the figure. This aluminum block is attached to a flexible silicon hot plate. A unique aspect of this flexible hot plate is its ability to operate up to 180°C with minimum AC field generation. Low AC fields from the hot plate help in avoiding the effects of stray fields, resulting in field strength reduction of the permanent magnet. The whole assembly is placed in an aluminum box with a piece of wood between the aluminum block and box base for thermal isolation. Hall Effect sensors (HAL825) are attached to the wall of the aluminum box. This configuration ensures that the distance between the magnet and the sensor remains fixed. The magnet-Hall Effect sensor positions are fixed with gap dimensions shown in Table 7.3. A thermocouple is attached to the aluminum block for reference temperature measurement. The temperature is kept constant at 127°C using the temperature controller shown in the Figure 7.15. Furthermore, the data are recorded continuously using PC, NI data acquisition card and LabVIEW [34].

Observations

1. Figure 7.16 shows the recorded hot plate temperature vs. time. The hot plate temperature shows an uncertainty of approximately 2.5°C from the set point. Over the course of 908 hours, the temperature drifted from 127°C to 130°C. Some of these variations may have occurred due to minor changes in the room temperature.

Table 7.3
Distance between cylindrical magnet and Hall Effect sensor

Sr. Number	Diameter (mm)	Length (mm)	Distance (mm)
1	2	4	8
2	3	4	12
3	3	5	13.5
4	4	5	14

2. Figure 7.17 shows the magnetic field strength and field strength change vs. time for D=2 mm L=4 mm long magnet. This was the smallest magnet by volume amongst tested. The measurements showed an increase in magnetic field with time. After 800 hours the magnetic field trend appeared to have stabilized after a gain of approximately 1.5%.

3. Figure 7.18 show magnetic field strength and field strength change vs. time for D=3 mm L=4 mm magnet. This magnet showed a small magnetic field loss with time. The loss was only 2% after 908 hours at 128°C.

4. Figure 7.19 shows the magnetic field strength and field strength change vs. time for D=3 mm L=5 mm magnet. This magnet showed a small low magnetic field loss about 0.5% after 908 hours at 128°C. This loss in magnetic field is very low considering the fact that hot plate temperature also drifted from set point during the test duration.

5. Figure 7.20 shows the magnetic field strength and field strength change vs. time for D=4 mm L=5 mm magnet. This was the largest magnet tested. The loss in field strength was less than 0.5% after 908 hours at 128°C. Similarly to the D=3 mm L=5 mm magnet, the loss in magnetic field is very low. Small variations were observed in the magnetic field during initial stages from start to 300 hours.

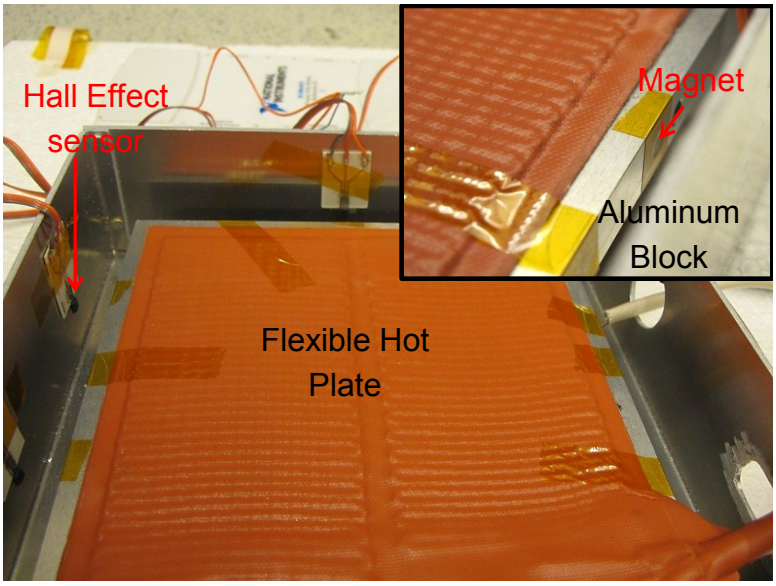

(a)

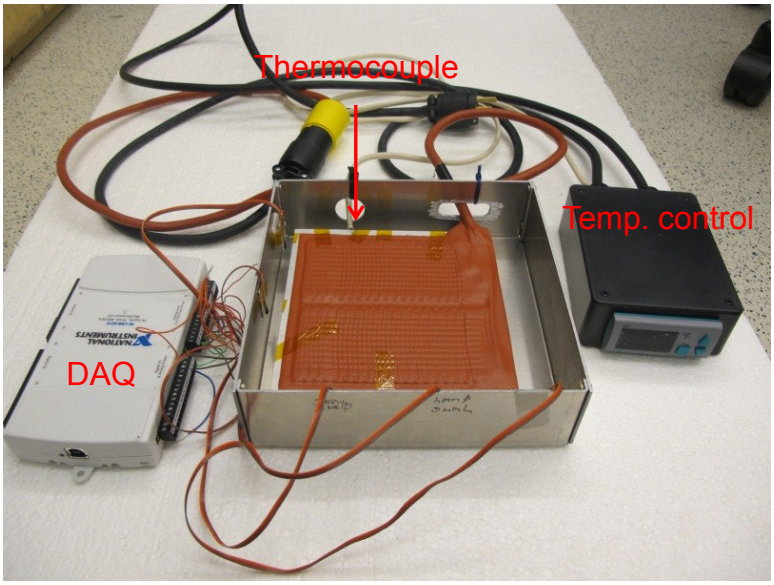

(b)

Fig. 7.15. (a) Long term test setup for studying effect of thermal cycling on magnet lifetime.

These variations were possibly due to thermal expansion of the magnets in the aluminum block that led to changes in the magnet-Hall Effect sensor distance.

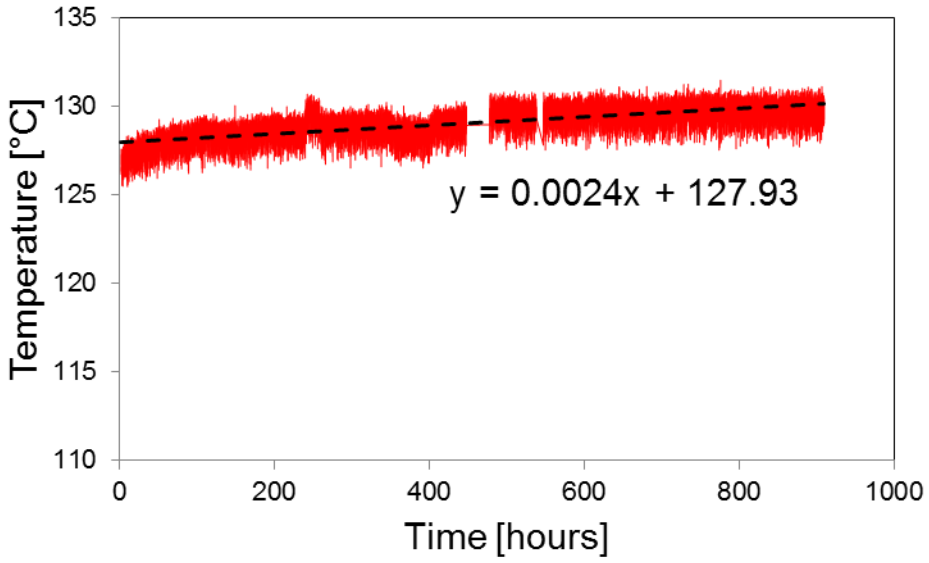

Fig. 7.16. Measured hot plate temperature vs. time

6. The recorded noise in the sensor output in all magnetic field measurements was possibly due to a) variation in temperature caused by the ON-OFF type temperature controller b) inherent noise from Hall Effect sensor, and c) limited resolution of data acquisition card. The noise from these sources was reduced by averaging and software filtration in the post collection data.

7. Figures 7.17 to 7.20 show two zones where the trend line had discontinuities. These discontinuities were caused by a malfunction in the computer that was capturing the data. During this malfunction the hot plate continued to operate and maintain the constant temperatures. Hence when the system recovered there was no effect on the overall measurement trend.

7.2.5 Discussion and magnet lifetime estimation

From the measurements shown in Sections 7.2.2 and 7.2.4, it is reasonable to conclude that the change in magnetic field strength for smaller magnets may become erratic at high temperatures. This is evident from results presented in Figures 7.8

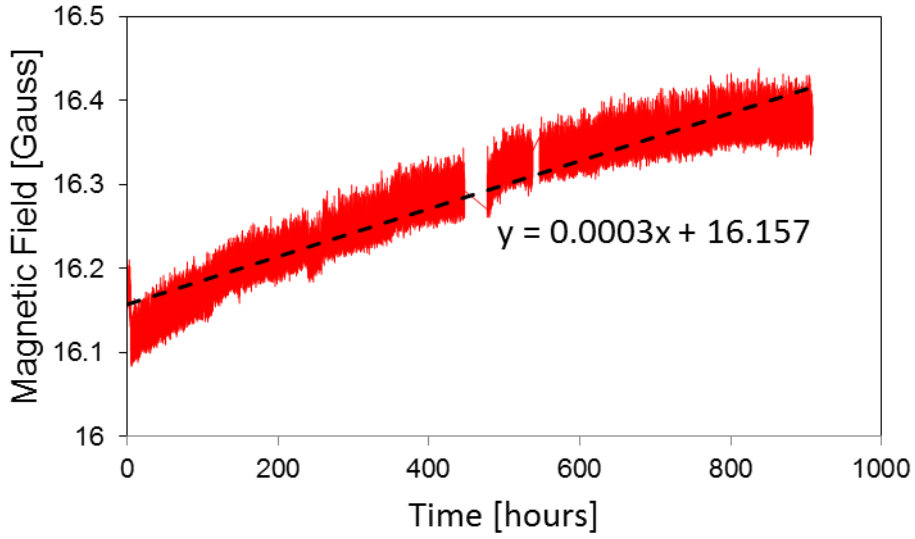

(a)

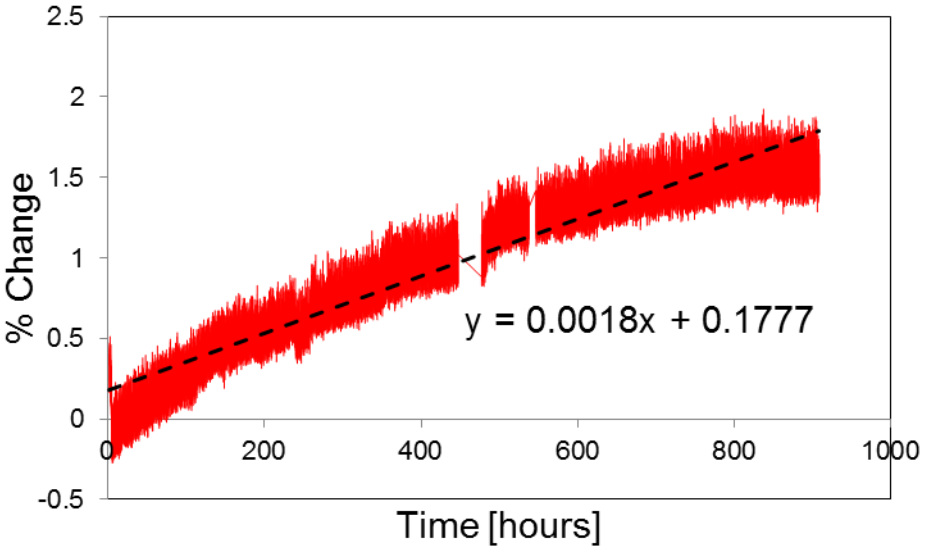

(b)

Fig. 7.17. (a) Measured magnetic field strength vs. time for 2 mm diameter, 4 mm length magnet. (b) Magnetic field strength loss vs. time for 2 mm diameter, 4 mm length magnet.

and 7.17 where the magnetic field for the 2 mm diameter, 4 mm length magnet decreased at the temperature of 75°C and increased at the temperature of 128°C.

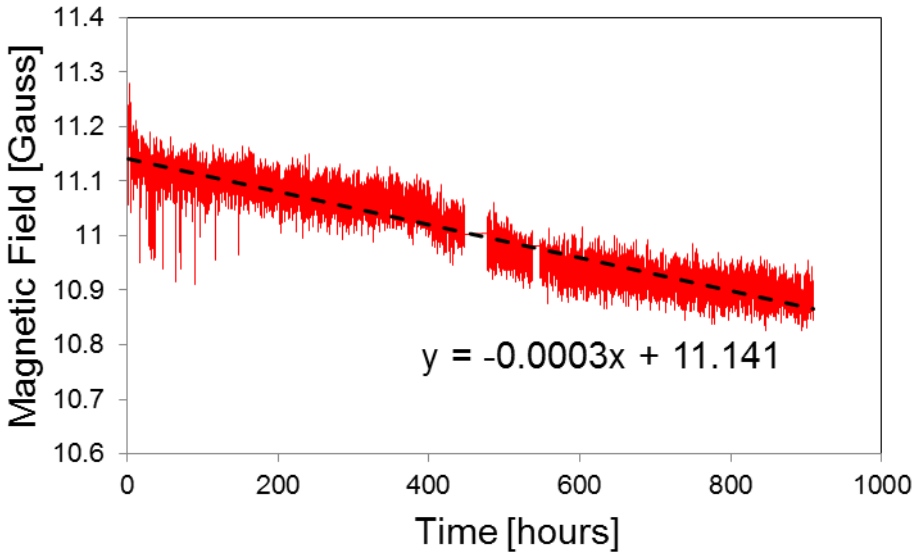

(a)

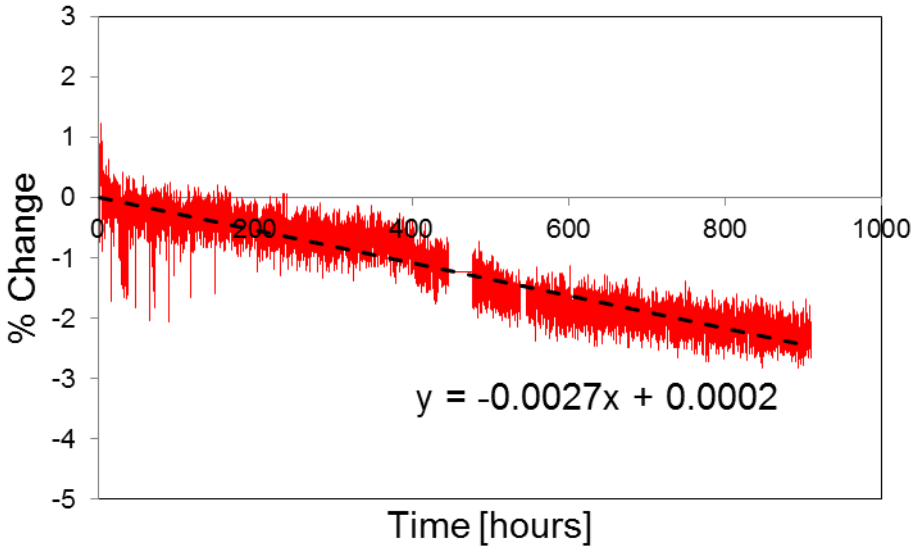

(b)

Fig. 7.18. (a) Measured magnetic field strength vs. time for 3 mm diameter, 4 mm length magnet. (b) Magnetic field strength loss vs. time for 3 mm diameter, 4 mm length magnet.

Furthermore, the measurements shown in Sections 7.2.1 and 7.2.2 indicate that even if the magnet's permeance coefficient is greater than 3.3, there is a lower limit to the

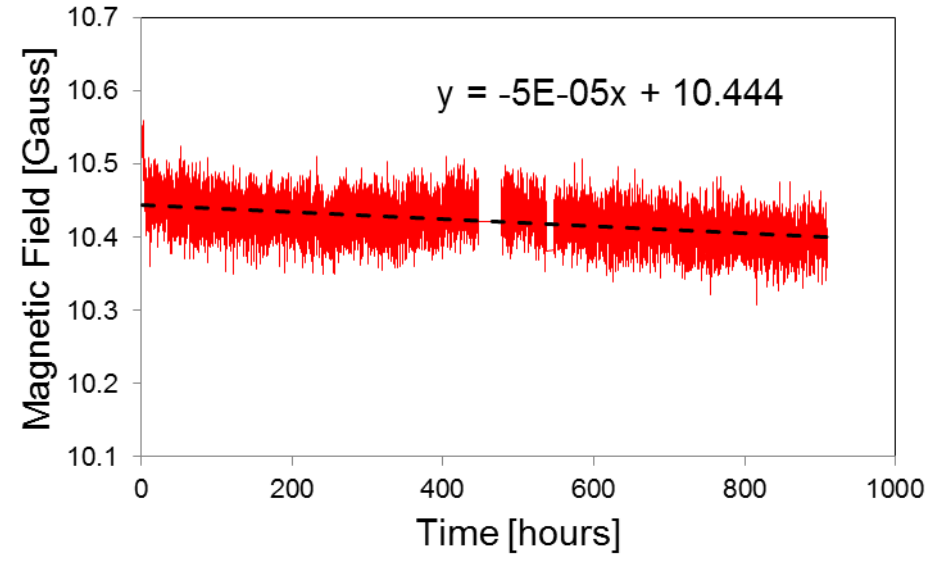

(a)

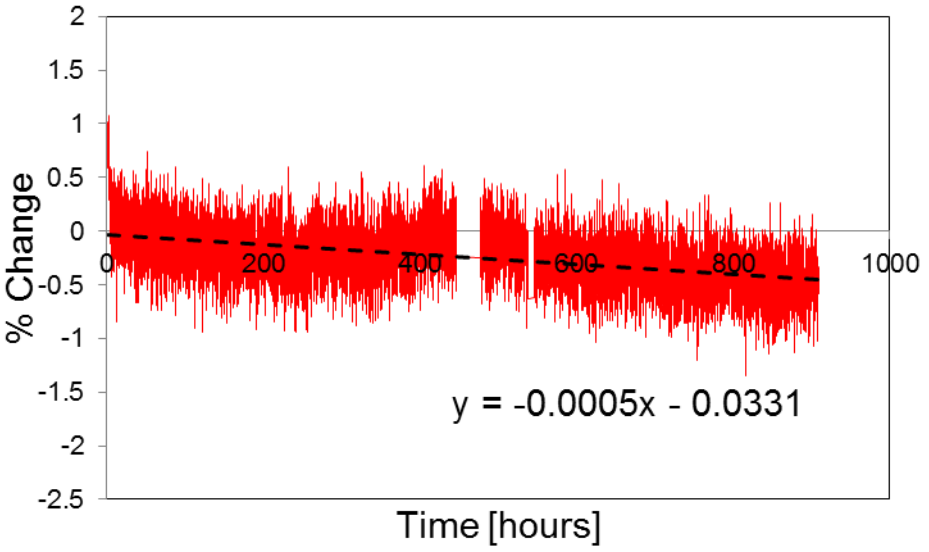

(b)

Fig. 7.19. (a) Measured magnetic field strength vs. time for 3 mm diameter, 5 mm length magnet. (b) Magnetic field strength loss vs. time for 3 mm diameter, 5 mm length magnet.

magnet's physical dimension (in this case 2 mm diameter and 4 mm length) beyond which the magnet may lose field strength, irrespective of the permeance coefficient

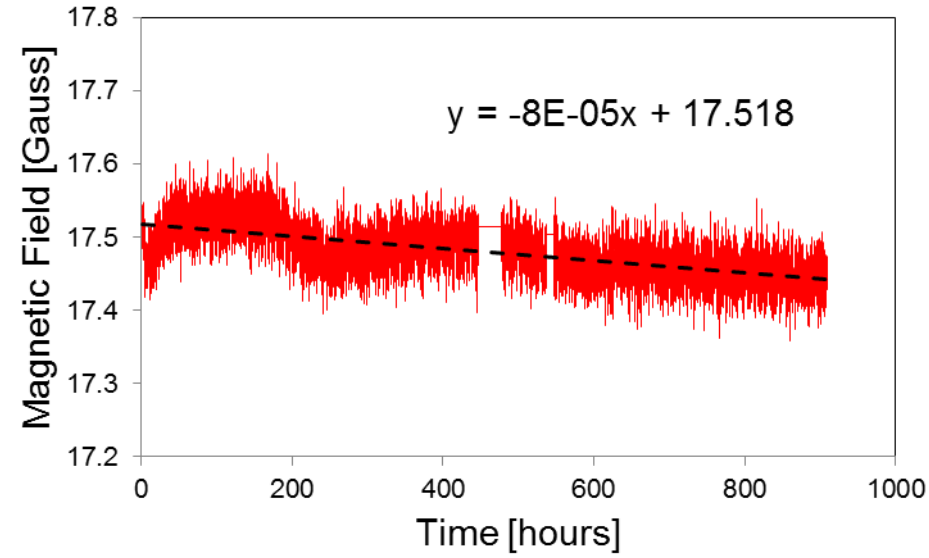

(a)

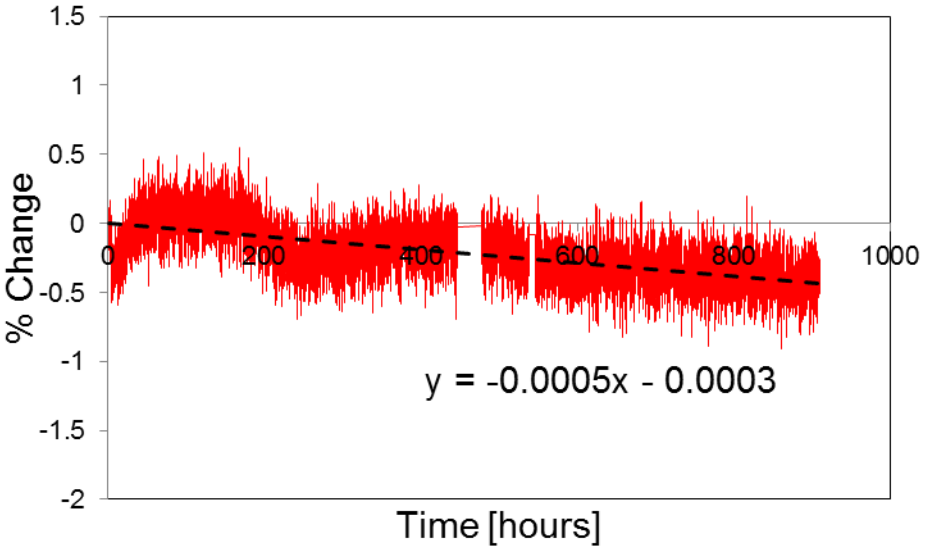

(b)

Fig. 7.20. (a) Measured magnetic field strength vs. time for 4 mm diameter, 5 mm length magnet. (b) Magnetic field strength loss vs. time for 4 mm diameter, 5 mm length magnet.

value. As a result the magnet's volume may play an important role in time-based magnetic field losses. The losses reduce significantly as magnet's volume in increased.

In 1975 Kavalerova et al. and in 1984 Levingston et al. had presented measurements at high temperatures for samarium cobalt magnets. When they subjected these magnets to high temperatures, some magnets showed a gain in magnetic field, others showed loss, while few remained stable [43], [44]. The results presented in this study for neodymium magnets show similar behavior, especially for these smaller cylindrical magnets. Similarly, when they thermally cycled the magnets, an increase in magnetic field was observed for few samples depending on magnet's magnetization-demagnetization history. These effects are observed in this study also as presented in Section 7.2.3. The magnetic field losses in permanent magnets are governed by magnetic viscosity, which is known to be a statistical relaxation phenomenon, caused by thermal fluctuation in the non-equilibrium state of the material [45]. For magnets, a logarithmic law describes magnetization-demagnetization as a function of time and magnetic field given by equation 7.5 [46]

$$M(t, H) = M(t_0, H) - S(H) \times ln\frac{t}{t_0} \tag{7.5}$$

where M is magnetization, H is magnetic field strength, t is time, S is a phenomenological magnetic viscosity constant and t_0 is the reference time. The magnetic viscosity constant is determined by equation 7.6 [47]

$$S = \frac{kT}{vK} f(H, T) M_s \tag{7.6}$$

where k is Boltzmann constant, T is temperature, v is the activation volume and K is the anisotropy constant that are dependent on the magnet material and its microstructure. The $f(H, T)$ function is a complicated entity that describes the exact nature of the magnetization at a particular temperature. In many commercial magnets these properties are unknown and inconsistent. From these equations, results presented by [33], [44] and measurements presented in this study, it is reasonable to conclude that for developing an analytical model that can predict the magnet lifetime at a given temperature, a number of parameters need to be known. More specifically, operating temperature, magnet's material, microstructure, magnetization history need to be known along with permeance coefficient and coercivity.

An ideal method for testing magnet's lifetime at high temperatures would include taking fresh magnets from a foundry, magnetizing them, annealing them for reducing effects of un-stabilized domains, and then subjecting them to high temperatures for data collection. Additionally, at regular intervals, it would be necessary to optically observe the magnet's microstructure to study the temperature induced variations in magnetic domains. In this study, the nickel coated magnets were procured from China. This procurement process took almost 1.5 months for magnets to arrive at our laboratory. Additionally, 2.5 months were spent in optimizing the test setup. During this process the magnet's history was unknown as magnets were placed in the vicinity of magnetic materials such as iron sheets and they were kept as a bundle with multiple small magnets of same type. Furthermore, the magnetic domains cannot be observed microscopically, as they are coated with metallic layers for external protection. All these external conditions alter the history of the magnet and in turn, their behavior at high temperatures. These effects are more prominent for magnets with smaller dimensions. From the recorded results, it is clear that for reliable operation of this sensor concept for long durations, the magnets should have a reasonable permeance coefficient as well as relatively large physical volume. Additionally, the magnets history should be closely controlled to avoid erratic responses and limit the losses, if any, at high temperatures.

However, from the tests results shown in Section 7.2.4, as a first degree approximation, we can estimate the lifetime of the cylindrical magnets that showed loss at high temperatures with time by extrapolating the field strength loss trends. Lifetime in this case is defined as the duration in which the magnet will be completely demagnetized. This extrapolation is performed using curve fit equations shown in magnetic field loss vs. time graphs at 128°C. The lifetime calculation for the 2 mm diameter magnet is not performed due to erratic behavior at high temperatures. Figure 7.21 shows extrapolated magnetic field strength loss vs. time (years) for three cylindrical magnets. The 3 mm diameter 4 mm length magnet shows a lifetime of 4.2 years. Furthermore, the 3 mm diameter, 5 mm length magnet and 4 mm diameter, 5 mm

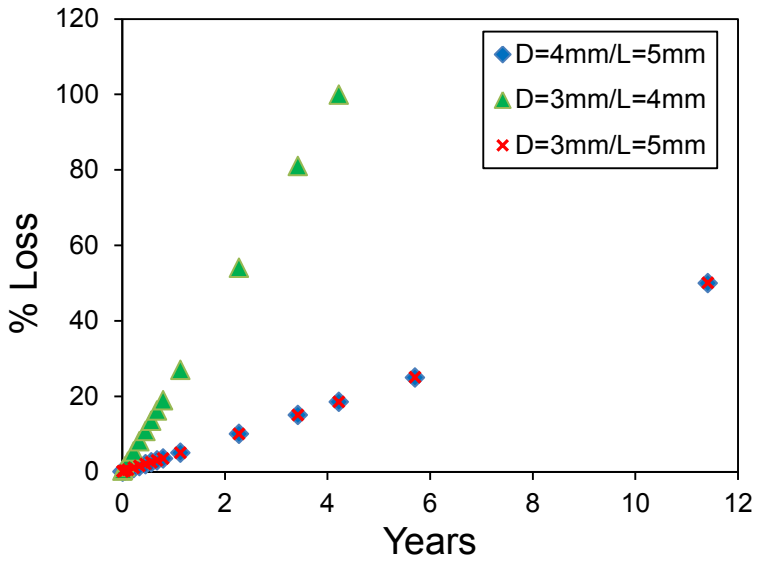

Fig. 7.21. Extrapolated magnetic field strength loss vs. time for cylindrical magnets.

length magnet show an identical loss of only 50% in magnetic field strength after 11.5 years at 128°C. These estimated lifetimes indicate that for mechanical seal applications, the magnets need to have a minimum of 3 mm diameter and 4 mm length for a lifetime of greater than 5 years at operating temperatures below 80°C. For higher temperatures, we may have to select magnets with larger volume while maintaining high permeance coefficient or use Samarium Cobalt and AlNiCo magnets that have higher temperature ratings. For bearing temperature monitoring the ring magnets presented in chapter 3 has reasonable volume with high permeance coefficient. Based on results presented by [33] for neodymium magnets with a permeance coefficient of 3.3 and higher, the estimated lifetime of the proposed ring magnet is greater than 10,000 hours.

7.3 Conclusion

In this chapter we have presented estimations for neodymium magnet life time which is more than 50,000 hours at 128°C. The lifetime estimations based on op-

timized measurements, provide an excellent base to use this concept for conditions monitoring applications in machines for extended durations. Nevertheless, the magnets can also be re-magnetized at regular maintenance intervals, thus possibly making the sensor operational for decades.

8. FUTURE WORK

8.1 Reliability study and dynamic tests on bearings and mechanical seals

The reliability measurements presented in this study needs to be extended up to 200°C and beyond for obtaining a more accurate prediction for a magnet's lifetime. Furthermore, the measurement setup can be improved to include detailed magnet history. Since, certain types of mechanical seal and bearing applications require temperatures beyond 200°C samarium cobalt and ALNICO magnets can be considered as sensing device.

Future work should also involve testing the developed sensors for hundreds of hours on rotating machinery under a variety of operating conditions. Additional tests should be performed to test the reliability of the magnet coatings by subjecting them to various fluids in pumps and bearings.

In this study, all applications use Hall Effect sensors for measuring magnetic field change. The Hall Effect sensor-magnet distance depends on the Hall Effect sensor's sensitivity and signal-to-noise ratio. Although, Hall effect sensors have good linearity and sensitivity, they tend to have low signal-to-noise ratio that limits the magnet-Hall Effect sensor distance. Other sensors based on the magneto-resistance effect in thin films may provide improved specifications and can enable larger magnet-Hall Effect sensor distances. Alternatively, smaller magnets can be used if distance is kept constant.

8.2 Temperature sensor based on permeability change in material

The sensor presented in this thesis ehibit excellent performance, but suffers from gradual magnetic field losses although their estimated lifetime is significantly higher

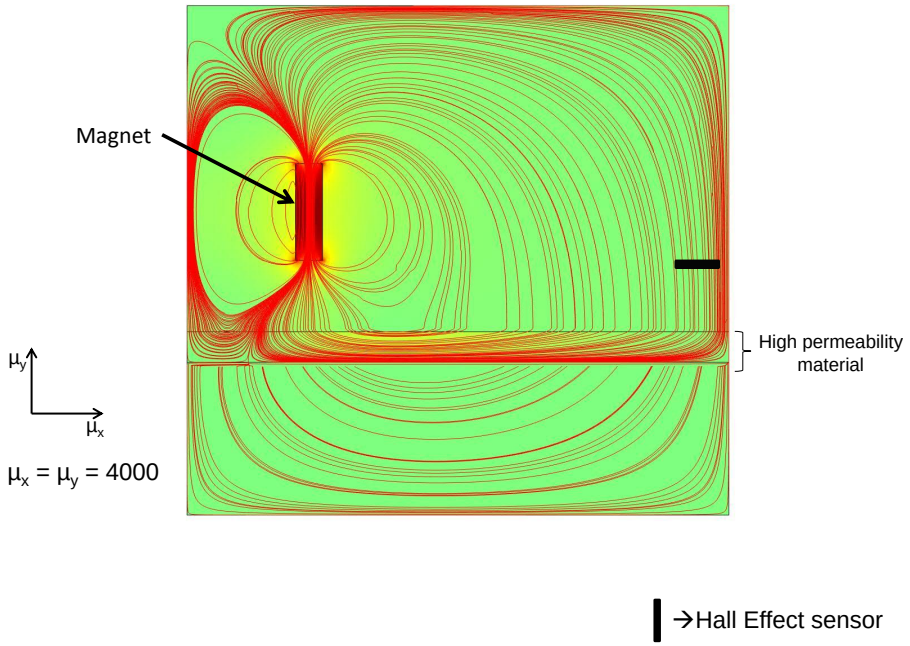

Fig. 8.1. COMSOL simulations showing magnetic field lines passing through high permeability metal plate [48]

than 10,000 hours. This effect is dominant since the magnet is placed in the hot zone for sensing temperature. A possible solution to this issue is shown in Figure 8.1. A permanent magnet is used as a source of static magnetic field placed in a relatively cold zone. The magnetic field lines pass through a high permeability material plate. This material has temperature dependent permeability. On the other end of the plate, a Hall Effect sensor senses the fields passing through the plate. As temperature is changed the permeability of the material changes resulting in reduced magnetic field lines reaching the Hall Effect sensor. Some high permeability materials (available from [49]) that have linear and monotonic permeability response with respect to temperature are show in Figure 8.2. Such materials can be used for implementing this concept with neodymium magnets as static magnetic field source.

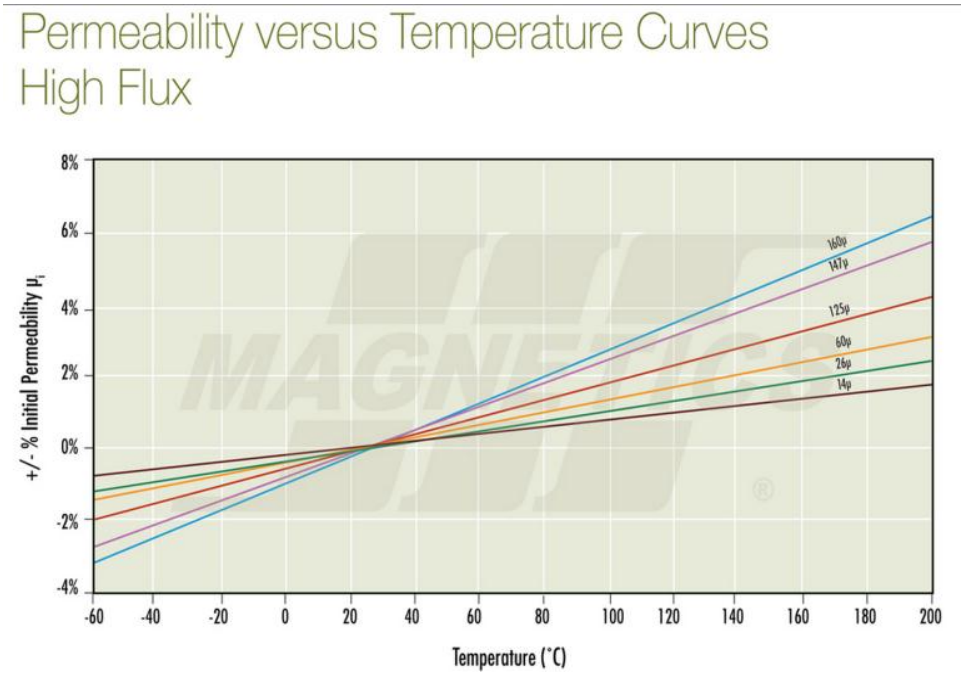

Fig. 8.2. Permeability change vs. temperature of high permeability materials [49]

8.3 Displacement sensor for mechanical seals

Measuring displacement and strain in mechanical seals can be an extension of the sensor concept presented in this study. Mechanical seals undergo radial deformation while in operation due to continuous large-scale axial pressure. This deformation often results in tapering of the seal thus leading to increased leakage. A combination of a magnet, Hall effect sensor and thin film magnetic material such as iron, nickel, cobalt can be utilized for such a sensor implementation. This concept is illustrated in Figure 8.3. The magnet and Hall effect sensor are placed in a hole in the flange at a distance as shown in Figure 8.3. A thin layer of high permeability material is deposited on the inner circumference of the seal stator. For zero deformation condition, the magnet-thin film-Hall Effect sensor distance remains fixed and Hall Effect sensor gives a fixed voltage output. Any radial deformation in the seal will alter magnet-thin film-Hall Effect sensor distance resulting in a variation in the Hall

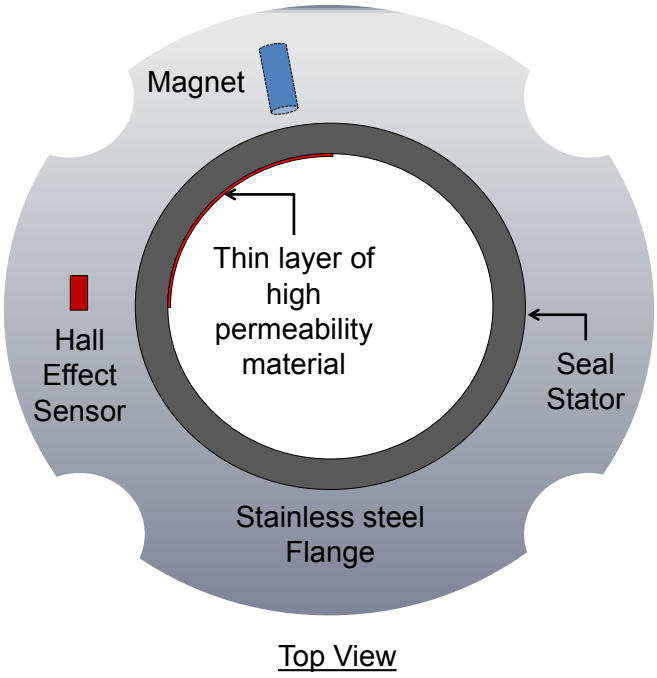

Fig. 8.3. Illustration of displacement sensor using permanent magnets for mechanical seals

effect sensor voltage output. This variation will be proportional to seal deformation and in turn proportional to the radial strain experienced by the seal. The sensor could be further extended to include multiple magnets and Hall Effect sensors to measure the complete circumferential profile of the seal stator.

8.4 Embedded sensors enable advanced data analytics

Advanced sensors such as the once presented in this study enable unprecedented accuracy and response time compared to any commercial wired sensors. The placement of the sensors thus far presented is the closest a user can get to the source of failure. But sensors are only a part of advanced condition monitoring and predictive analytics. For example, mathematical models such as SKF's L10 bearing life model can predict bearing lifetime based on user input. However, the model's accuracy is

limited as it does not account for realtime measurement data [29]. Similarly, simulation data derived from FEA-based models presented in [50] may be compared to actual measured failure data and help in understanding failure modes. Nevertheless, they cannot predict machine lifetime by taking into account real-time machine operating conditions and system parameters. Intelligent analytical and behavioral models that can analyze sensor data can provide the user with information about machine component lifetime. They can further result in improved maintenance actions for efficient machine operation that can be scheduled accurately on need basis. As a future extension of this study, development of such analytical and behavioral models for bearings and mechanical seals using the proposed sensors or more advanced sensors may significantly advance condition monitoring technologies and predictive analytics.

LIST OF REFERENCES

LIST OF REFERENCES

[1] A. Kovacs, D. Peroulis, and F. Sadeghi, "Early-warning wireless telemeter for harsh-environment bearings," in *Sensors, 2007 IEEE*, pp. 946 –949, oct. 2007.

[2] D. Industry, "Roller Element Bearing." `http://img.directindustry.com/images_di/photo-g/high-precision-ball-bearing-8884-4332229.jpg`, 2012. "[Online; accessed 10-October-2013]".

[3] T. Tallian, *Failure atlas for Hertz contact machine elements*. ASME Press, 1999.

[4] B. Liptak, *Temperature Measurement*. Taylor & Francis, 1993.

[5] D. A. Nickel and F. Sadeghi, "In situ tribocomponent temperature measurement using a radio telemeter," *Tribology Transactions*, vol. 40, no. 3, pp. 514–520, 1997.

[6] A. Joshi, S. Marble, and F. Sadeghi, "Bearing cage temperature measurement using radio telemetry," *Proceedings of the Institution of Mechanical Engineers, Part J: Journal of Engineering Tribology*, vol. 215, no. 5, pp. 471–481, 2001.

[7] S. Scott, A. Kovacs, L. Gupta, J. Katz, F. Sadeghi, and D. Peroulis, "Wireless temperature microsensors integrated on bearings for health monitoring applications," in *Micro Electro Mechanical Systems (MEMS), 2011 IEEE 24th International Conference on*, pp. 660 –663, jan. 2011.

[8] Z. M. Zhang, "Surface temperature measurement using optical techniques," *Annual Reviews of Heat Transfer*, vol. 11, no. 11, pp. 351–411, 2000.

[9] L. Grattan and B. Meggitt, *Optical Fiber Sensor Technology: Volume 2: Devices and Technology*. Optoelectronics, Imaging and Sensing Series, Springer, 1997.

[10] A. Barber, *Handbook of Noise and Vibration Control*. Elsevier advanced technology, Elsevier Advanced Technology, 1992.

[11] C. Ovrn, M. Adolfsson, and B. Hk, "Fiber-optic systems for temperature and vibration measurements in industrial applications," *Optics and Lasers in Engineering*, vol. 5, no. 3, pp. 155 – 172, 1984.

[12] J. Zook, W. R. Herb, C. Bassett, T. Stark, J. N. Schoess, and M. L. Wilson, "Fiber-optic vibration sensor based on frequency modulation of light-excited oscillators," *Sensors and Actuators A: Physical*, vol. 83, no. 13, pp. 270 – 276, 2000.

[13] Y. Rao, P. Henderson, D. Jackson, L. Zhang, and I. Bennion, "Simultaneous strain, temperature and vibration measurement using a multiplexed in-fibre-bragg-grating/fibre-fabry-perot sensor system," *Electronics Letters*, vol. 33, pp. 2063 –2064, nov 1997.

[14] A. Lebeck, *Principles and design of mechanical face seals*. Wiley-Interscience publication, Wiley, 1991.

[15] Silberwolf, "Rotating mechanical seal-3D." `http://commons.wikimedia.org/wiki/File:Rotating_mechanical_seal-3D_135.png`, 2013. "[Online; accessed 17-February-2012]".

[16] Y. E. Fan, F. Gu, and A. Ball, "A review of the condition monitoring of mechanical seals," *ASME Conference Proceedings*, vol. 2004, no. 41758, pp. 179–184, 2004.

[17] L. Gupta and D. Peroulis, "Wireless temperature sensor for condition monitoring of mechanical seals," in *Microwave Conference (EuMC), 2012 42nd European*, pp. 424–427, 2012.

[18] P. S. Y. Chu and A. Cameron, "Flow of electric current through lubricated contacts," *A S L E Transactions*, vol. 10, no. 3, pp. 226–234, 1967.

[19] A. Cameron and R. Gohar, "Theoretical and experimental studies of the oil film in lubricated point contact," *Proceedings of the Royal Society of London. Series A. Mathematical and Physical Sciences*, vol. 291, no. 1427, pp. 520–536, 1966.

[20] H. Osada, S. Chiba, H. Oka, H. Hatafuku, N. Tayama, and K. Seki, "Non-contact magnetic temperature sensor for biochemical applications," *Journal of Magnetism and Magnetic Materials*, vol. 272-276, Supplement, no. 0, pp. E1761 – E1762, 2004. Proceedings of the International Conference on Magnetism (ICM 2003).

[21] L. A. Gupta and D. Peroulis, "Wireless temperature sensor operating in complete metallic environment using permanent magnets," *Magnetics, IEEE Transactions on*, vol. 48, pp. 4413 –4416, nov. 2012.

[22] P. Campbell, *Permanent magnet materials and their application*. Cambridge University Press, 1996.

[23] "Arnold magnetic technologies," 2013.

[24] J. Lenz and S. Edelstein, "Magnetic sensors and their applications," *Sensors Journal, IEEE*, vol. 6, pp. 631 –649, june 2006.

[25] "Allegro microsystems inc.," 2011.

[26] "Teca corporation," 2013.

[27] "National instrument corporation," 2013.

[28] B. S. S. Association, "Magnetic properties of stainless steel," may. 2000.

[29] "Skf group," 2012.

[30] L. A. Gupta, L. Young, B. Wondimu, and D. Peroulis, "Wireless temperature sensor for mechanical face seals using permanent magnets," *Sensors and Actuators A: Physical*, vol. 203, no. 0, pp. 369 – 372, 2013.

[31] "Yungsheng usa inc.," 2013.

[32] "Micronas, semiconductor, holding, ag." http://www.micronas.com/, 2012.

[33] M. Haavisto and M. Paju, "Temperature stability and flux losses over time in sintered ndfeb permanent magnets," *Magnetics, IEEE Transactions on*, vol. 45, pp. 5277 –5280, dec. 2009.

[34] "National instruments corporation." www.ni.com, 2012.

[35] L. Young. Flowserve Corporation, Temecula, CA, Jan 2013. Private communication.

[36] "Agilent technologies." http://www.home.agilent.com, 2012.

[37] L. Gupta and D. Peroulis, "Wireless temperature sensor for condition monitoring of bearings operating through thick metal plates," *Sensors Journal, IEEE*, vol. 13, no. 6, pp. 2292–2298, 2013.

[38] "Polytec, gmbh, waldbronn." http://www.polytec.com/us/, 2013.

[39] P. Campbell, "The design and application of high energy rare earth permanent magnets," in *Electrical Electronics Insulation Conference, 1995, and Electrical Manufacturing Coil Winding Conference. Proceedings*, pp. 49 –57, sep 1995.

[40] "K & j magnetics, inc.." http://www.kjmagnetics.com/glossary.asp, 2013.

[41] R. Parker, *Advances in permanent magnetism*. A Wiley interscience publication, Wiley, 1990.

[42] S. Constantinides. Arnold Magnetics, Rochester, NY, April 2012. Private communication.

[43] L. Kavalerova, B. Livshitz, A. Lileev, and V. Menushenkov, "The reversibility of magnetic properties of sintered smco5 permanent magnets," *Magnetics, IEEE Transactions on*, vol. 11, no. 6, pp. 1673–1675, 1975.

[44] J. Livingston and D. Martin, "Thermal remagnetization of co5sm magnets," *Magnetics, IEEE Transactions on*, vol. 20, no. 1, pp. 140–144, 1984.

[45] R. Skomski and J. Coey, *Permanent Magnetism*. Condensed Matter Physics Series, Institute of Physics Publishing, 1999.

[46] C. Hwang, S. B. John, S. S. Bor, and C. S. Chang, "The analysis and design of a ndfeb permanent-magnet motor for cd-rom drive," in *Electric Machines and Drives Conference Record, 1997. IEEE International*, pp. WB2/12.1–WB2/12.3, 1997.

[47] E. P. Wohlfarth, "The coefficient of magnetic viscosity," *Journal of Physics F: Metal Physics*, vol. 14, no. 8, p. L155, 1984.

[48] "Comsol, inc.." http://www.comsol.com/, 2012.

[49] "Magnetics, inc.." http://www.mag-inc.com/, 2012.

[50] F. Sadeghi, B. Jalalahmadi, T. S. Slack, N. Raje, and N. K. Arakere, "A Review of Rolling Contact Fatigue," *Journal of Tribology*, vol. 131, no. 4, p. 041403, 2009.

APPENDICES

A. HALL EFFECT SENSOR PROGRAMMING PROCEDURE

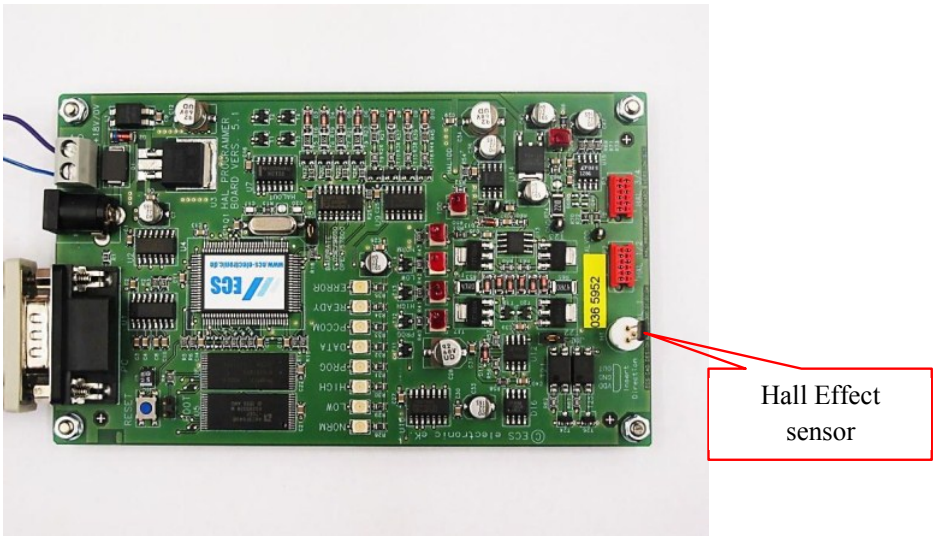

Fig. A.1. Programmer board for HAL825 Hall Effect sensor

The sensitivity with HAL825 sensor is a programmable sensor. The sensor's parameters such as sensitivity, voltage levels, internal noise filter, temperature coefficient of the chip can be programmed using a PC825 programmer board (Figure A.1) provided by Micronas Gmbh [32]. These settings are shown in Figure A.2.

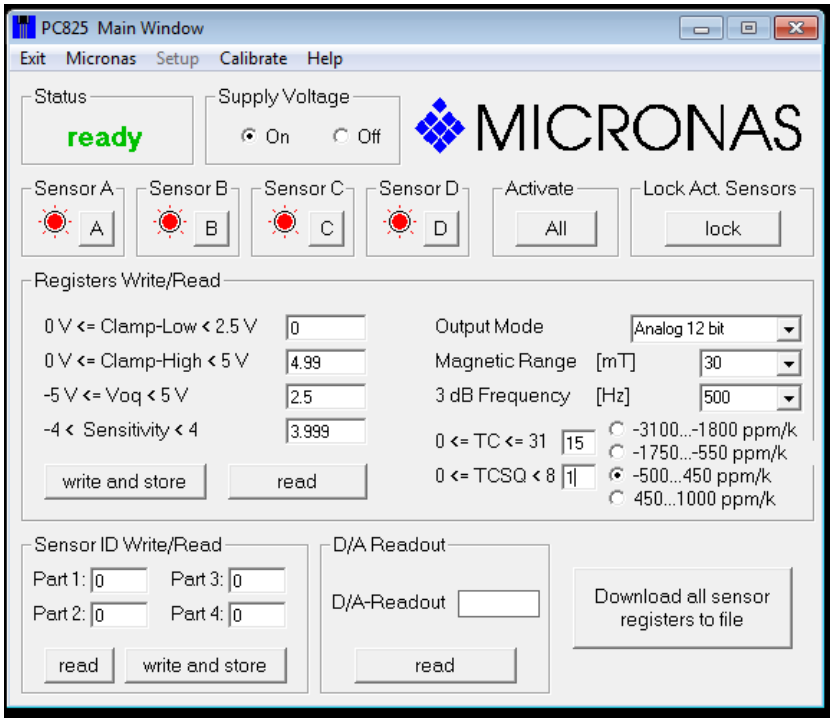

Fig. A.2. Programming settings for HAL825 Hall Effect sensor

B. LEVEL SHIFT CIRCUIT AND CALIBRATION PROCEDURE FOR MECHANICAL SEAL

B.1 Level shift circuit

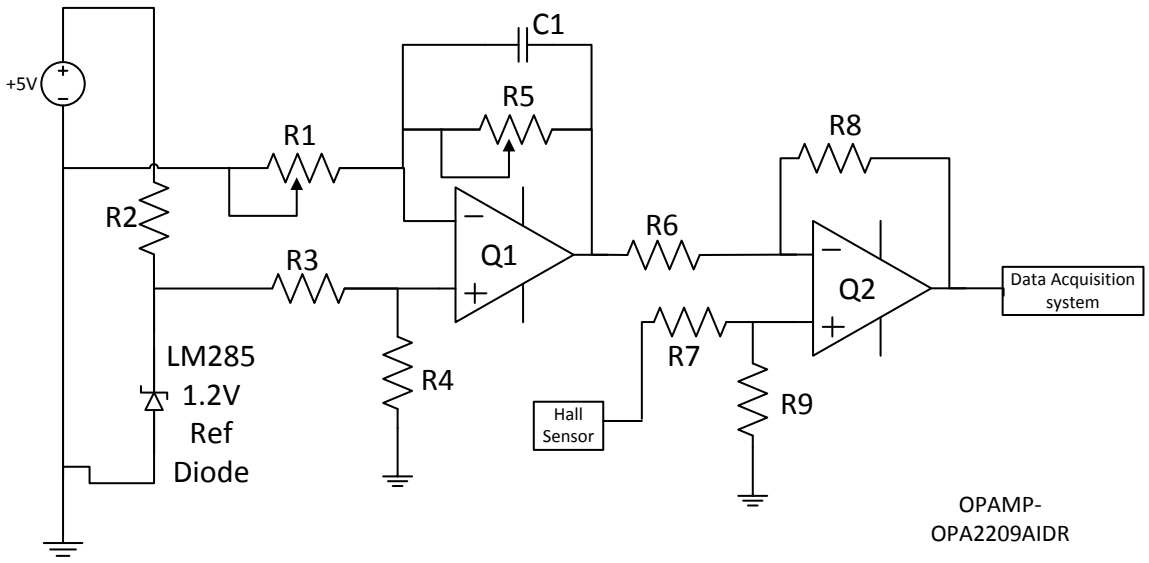

Fig. B.1. Level Shift Circuit simplified diagram

In this document, a level shift circuit is designed to remove the base voltage from the sensor output and make sensor output compatible with flow serve data acquisition system. The simplified circuit is shown in Figure B.1. A LM285-1.2V ref. diode generates a stable 1.2 volt which is amplified by Q1 to the voltage that needs to be subtracted from the Hall Effect sensor output. This voltage can be controlled by varying R1 and R5 and can be set to any value as required by the flow serve data acquisition system. The amplified reference voltage is given to a difference amplifier Q2 which subtracts the reference voltage from the Hall Effect sensor output depending

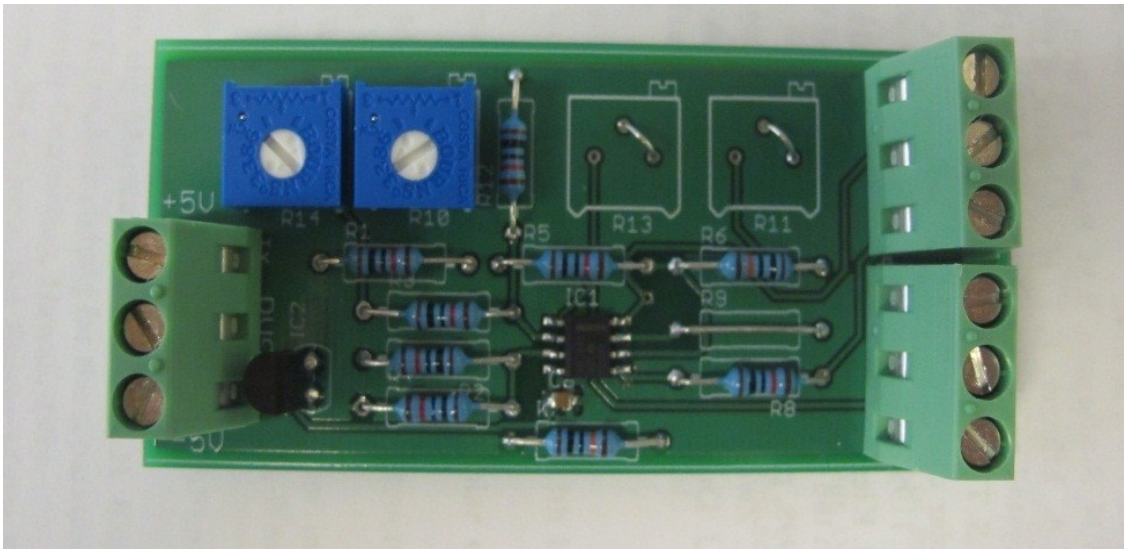

Fig. B.2. Level Shift Circuit PCB

on the base voltage and amplifies the difference signal by 10 for the data acquisition system. The final PCB for the circuit is shown in Figure B.2. The PCB is powered by +/- 5V power dual supply.

B.2 Calibration procedure

1. Tighten the sensor holder to its maximum limit as shown in Figure B.3 with the black triangle mark facing the shaft cavity as shown. F on the mark indicates front side of the Hall Effect sensor that needs to face the magnet in the seal.
2. Assemble the seal, Hall Effect sensor with sensor holder and the shaft in the pump. The calibration needs to be done with all the components mounted in the pump as shaft is magnetic and affects the sensor magnetic field. The calibration when done with the shaft, removes any error from the sensor output introduced by the magnetic shaft.

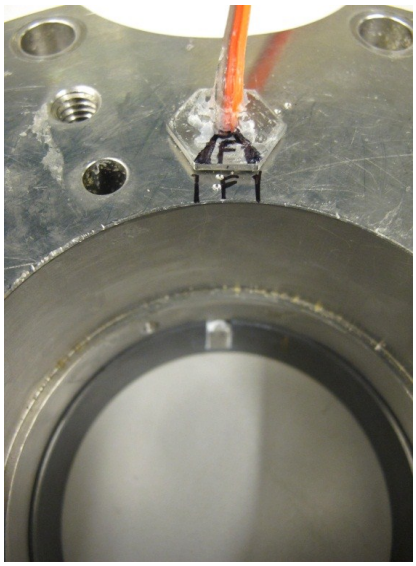

Fig. B.3. Sensor holder with reduced head tightened till the end and aligned with the marks on the flange

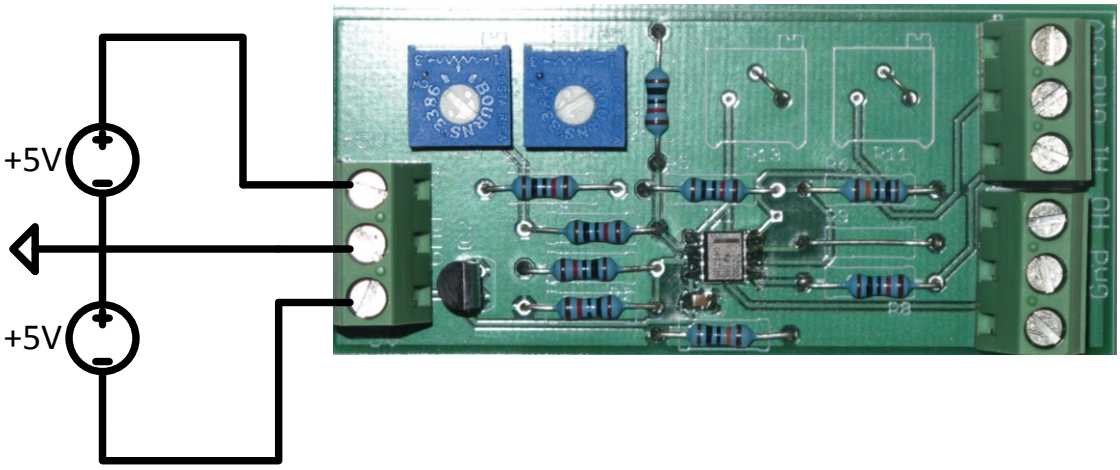

Fig. B.4. Power supply connections

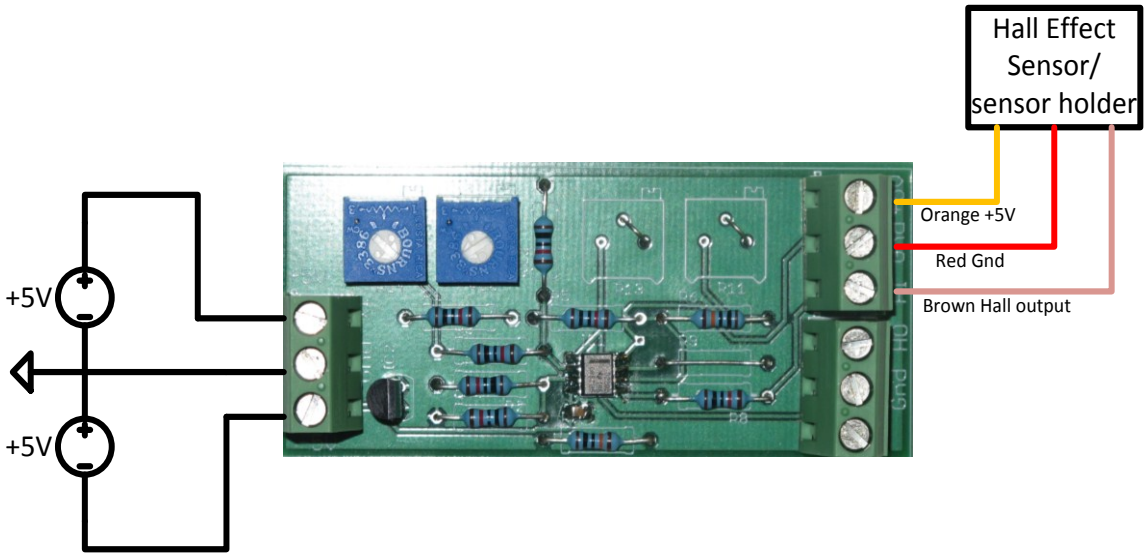

Fig. B.5. Hall Effect sensor connection

3. Make power supply connections to the sensor level shift circuit as shown in Figure B.4
4. Connect Hall Effect sensor wires as shown in Figure B.5. The Orange wire is +5 V, Red is Ground and Brown is HI that is Hall Effect sensor output as input to the board.
5. Measure the temperature of the pump/surrounding (stationary condition). The calibration point is set with respect to the room temperature/stationary pump temperature.
6. Connect a high resolution DC voltmeter between the ground terminal (Red wire) and Hall Effect sensor output (Brown wire) as shown in Figure B.6.
7. There are two methods to change the sensitivity of the Hall Effect sensor with respect to magnet. One way is to reprogram the Hall Effect sensor and change the sensitivity, or program the Hall Effect sensor to the highest sensitivity and

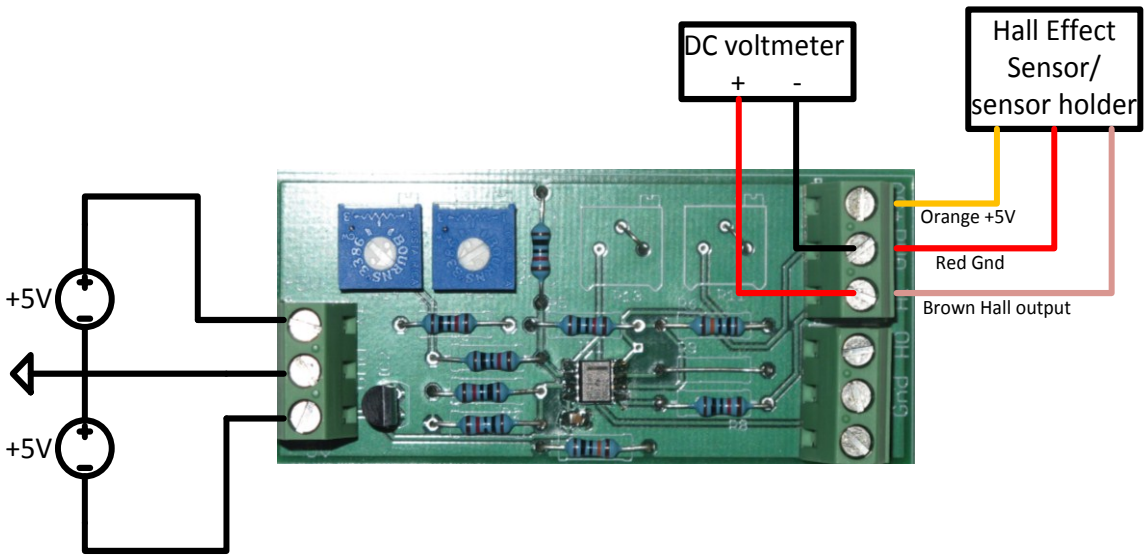

Fig. B.6. Hall Effect sensor sensitivity calibration connections

Table B.1
Reference voltage for Hall Effect sensor calibration

Flange / Surrounding Temperature [°C]	Sensitivity 1 [V]	Sensitivity 2 [V]	Sensitivity 3 [V]
19	1.644	1.753	1.850
20	1.665	1.753	1.850
21	1.665	1.754	1.851
22	1.666	1.755	1.851
23	1.667	1.755	1.851
24	1.667	1.756	1.852
25	1.668	1.756	1.852

then change the orientation of Hall Effect sensor by rotating it with respect to the flange. In this case we use the second method.

8. Turn on the power supply. The DC voltmeter should show some readings.
9. Rotate the sensor holder shown in Figure B.3 in counter clockwise direction using a wrench very slowly to match one of the voltages shown in the Table B.1 for the temperature measured at the flange. (Example: if flange temperature is 22°C and selected sensitivity range is 1.75 V, then rotate the holder till 1.755 V is observed on voltmeter.) This needs to be done very precisely with accuracy up to the 3 digit after decimal.
10. After calibrating the Hall Effect sensor to match for flange/surrounding temperature the next step is to calibrate the Level shift circuit board.
11. Connect the DC voltmeter as shown in Figure B.7. The voltmeter will show default reading at 1.841 V. This voltage is the reference voltage that the circuit

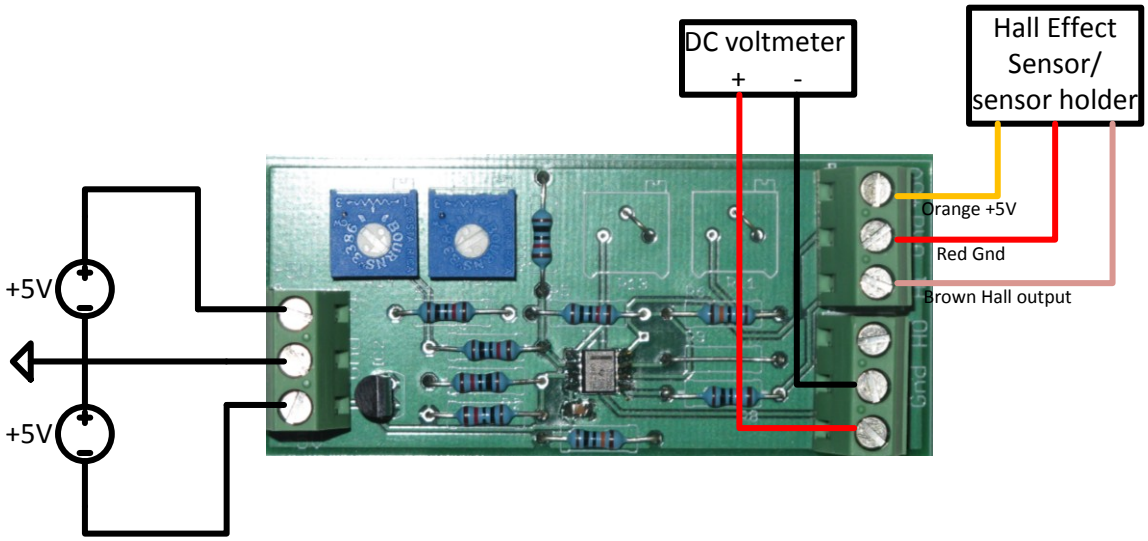

Fig. B.7. Level shift circuit calibration connection

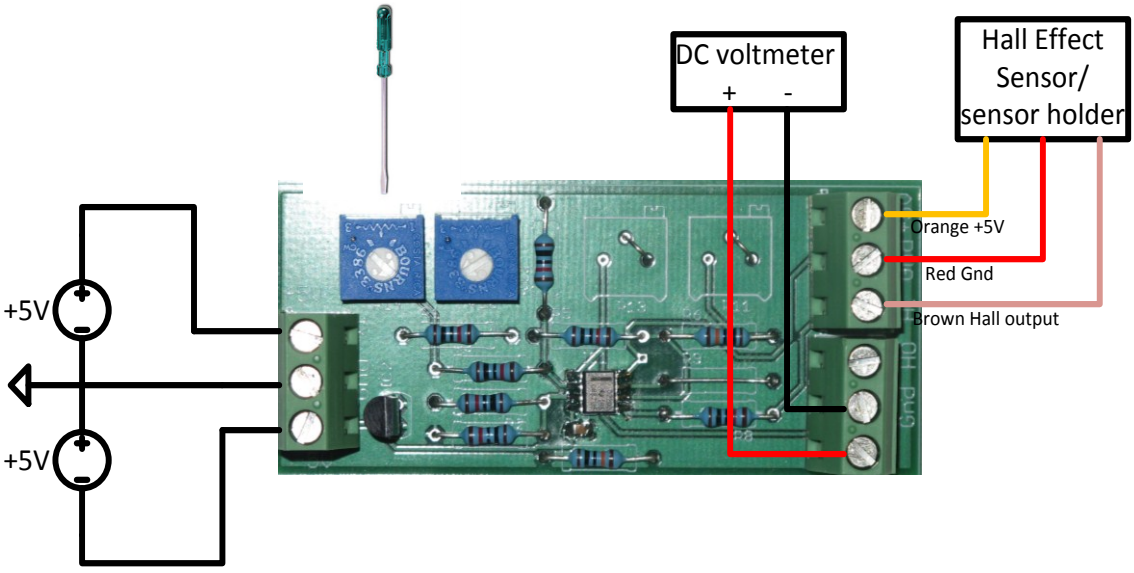

Fig. B.8. Tuning the Level shift circuit

Table B.2
Reference voltage for level shifting

	Sensitivity 1	Sensitivity 2	Sensitivity 3
Reference Voltage [V]	1.650	1.744	1.841

subtracts from the Hall Effect sensor output to remove the base voltage before signal amplification.

12. Take a small screw driver and vary the variable resistors R10 and R14 (Figure B.8) to set this voltage to appropriate value shown in Table B.2 depending on the sensitivity selected in step 9.

13. After completion of calibration of Hall Effect sensor and Level shift circuit, disconnect the voltmeter and connect the data acquisition system to HO (+ve) and gnd (-ve) terminals as show in Figure B.9.

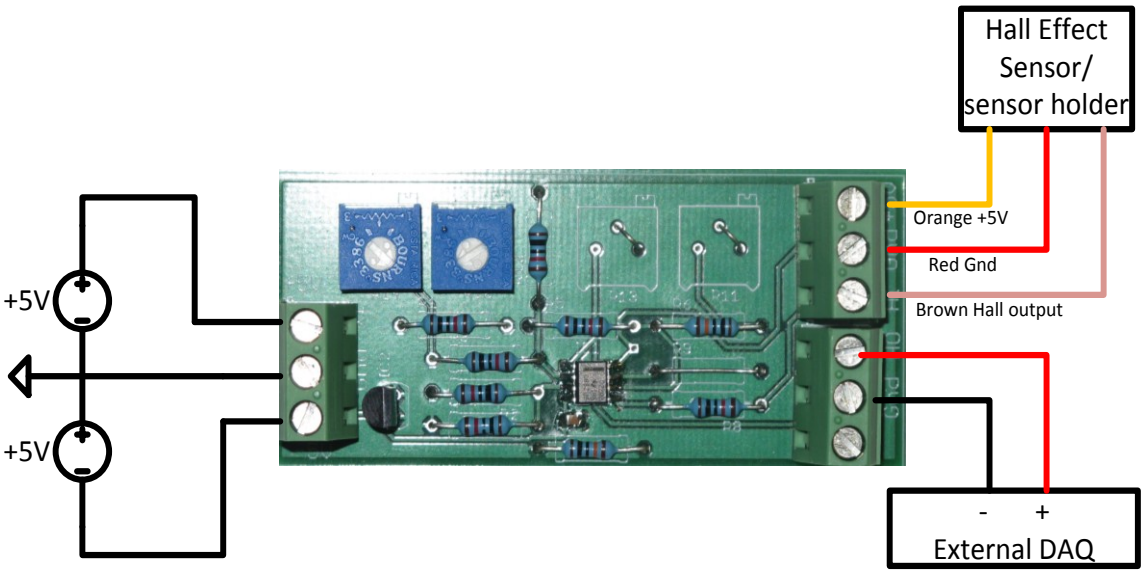

Fig. B.9. Connection to the data acquisition system

Table B.3
Calibration Equation and temperature measurement range. T is the temperature deduced from the voltage measured by the data acquisition system. V is the voltage measured by the data acquisition system.

	Calibration Equation	Temperature Range	Level Shift Output Voltage Range
Sensitivity 1	$T = \frac{V-2.407e-2}{5.757e-3}$	7.5°C-75.8°C	77 mV-470 mV
Sensitivity 2	$T = \frac{V+1.469e-2}{5.191e-3}$	7.5°C-75.8°C	37 mV-380 mV
Sensitivity 3	$T = \frac{V+5.943e-3}{4.041e-4}$	7.5°C-75.8°C	42 mV-310 mV

14. Table B.3 shows the calibration equations to be used in the data acquisition system control for temperature measurement depending on selected sensitivity. The table also compiles total variation in the sensor output and level shift circuit output for given temperature range.

VITA

VITA

Lokesh A. Gupta received his Bachelors degree from Vishwakarma Institute of Technology, Pune, India in May, 2006. After working in Forbes Marshall Pvt. Ltd. as Design and Development Engineer for two years he joined the Masters program at Purdue University, USA in Fall 2008. Following completion of Masters program in Summer 2010 with thesis research in wireless power transfer and sensors systems, he joined as a PhD. student at Purdue University with research focus on sensors and condition monitoring systems of bearings and mechanical seals. In Dec, 2013 he finished his Phd. and joined Bearing Analytics Inc. as VP of Research and Development. Dr. Gupta has nine research papers in peer reviewed journals and conferences as well as two filed patents. His area of interests include Analog and RF design, MEMS and sensor technologies.